2007

Flow structure along a 1303 unmanned combat air vehicle

Mehmet Alpaslan Kosoglu
Lehigh University

Kosoglu, Mehmet Alpaslan

Flow Structure Along a 1303 Unmanned Combat Air Vehicle

January 2008

FLOW STRUCTURE ALONG A 1303 UNMANNED COMBAT AIR VEHICLE

by

Mehmet Alpaslan Kosoglu

A Thesis

Presented to the Graduate and Research Committee

of Lehigh University

in Candidacy for the Degree of

Master of Science

in

The Department of Mechanical Engineering and Mechanics

Lehigh University

September, 2007

This thesis is accepted and approved in partial fulfillment of the requirements for the Master of Science.

09/04/07

Date

Thesis Advisor

Chairperson of Department

ACKNOWLEDGMENTS

I would like to express my sincere gratitude to my advisor, Prof. Donald Rockwell, for his knowledge, guidance, and encouragement throughout this study. His efforts toward my academic progress have been invaluable. I would also like to thank Dr. Micheal Ol from Air Force Research Labs at Wright-Patterson Air Force Base. Also, I am very grateful to the Air Force Office of Scientific Research for its financial support.

I appreciate the assistance of the machine shop, particularly Mr. Richard Towne, Mr. Robert Minnich and Mr. James Bunderla for their craftsmanship. I am also very thankful to Mrs. JoAnn Casciano, Mrs. Geri Kneller, and Mrs. Carol Paul and for their kindness and administrative assistance. Many thanks to Andrew for keeping all of the computers in our lab working properly and my colleagues, Mr. Philip Breneman, Dr. Emine Celik, Dr. Alis Ekmekci, Mr. Jason Foust, Dr. Metin Yavuz, Mr. Tunc Goruney, and Mr. Turgut Yilmaz for their valuable contributions and friendship.

I owe my heartfelt gratitude and thanks to my parents and my sister, for their support and to my best friends Emir Angin and Cem Celik, who despite being in three different countries have been like brothers to me.

Finally, I am grateful to my beautiful fiancée, Laura Marie Hannum, for her encouragement, support, patience, and love.

TABLE OF CONTENTS

LIST OF FIGURES

NOMENCLATURE

C	Chord of planform
CAD	Computer Aided Design
CFD	Computational Fluid Dynamics
LE	Leading-edge
LEV	Leading-edge-vortex
M	Mach number
PIV	Particle Image Velocimetry
Re	Reynolds number
RPM	Revolutions per minute
T	Time variable
u	Streamwise velocity
$\langle u \rangle$	Average streamwise velocity
U	Freestream velocity
u_{rms}	Root-mean-square value of streamwise velocity component
v	Transverse velocity
$\langle v \rangle$	Average transverse velocity
v_{rms}	Root-mean-square value of transverse velocity component
$\underline{V}$	Velocity vector
$\langle \underline{V} \rangle$	Average velocity vectors
x	Coordinate in streamwise direction
y	Coordinate in transverse direction

z	Coordinate in surface normal/crossflow direction
α	Angle-of-attack
Δ	Displacement from the wing surface
Λ	Sweep angle
μ	Dynamic viscosity, mean value of the random distribution
υ	Kinematic viscosity
$< >$	Time-average

ABSTRACT

The 1303 Unmanned Combat Air Vehicle is representative of a variety of UCAVs with blended wing-body configurations. The flow structure along a scale model of this configuration was investigated using dye visualization and particle image velocimetry, for variations of Reynolds number and angle-of-attack. Both of these parameters substantially influence the onset and structure of the leading-edge vortex (LEV) and a separation bubble/stall region along the tip. The onset of formation of the LEV initially occurs at a location well downstream of the apex, and moves upstream for increasing values of either Reynolds number or angle-of-attack. In cases where a separation bubble or stall region exists, quantitative information on its structure was obtained via PIV imaging on a plane nearly parallel to the surface of the wing. By acquiring images on planes at successively larger elevations from the surface, it was possible to gain insight into the space-time features of the three-dimensional structure of the bubble or stall region, which is highly time-dependent. Both the scale of this region and the corresponding velocity patterns show large variations. Time-averaged images indicate that the maximum velocity defect decreases in magnitude and moves in the downstream direction with increasing elevation from the surface of the wing.

1. INTRODUCTION

Leading-edge-vortices, i.e., LEVs, are the main feature of flow past a simple delta wing of given sweep angle. Their existence enhances the ability of a delta wing to generate substantial lift at higher angles-of-attack. Formation, breakdown and three-dimensional characteristics of LEVs on delta wings have been a subject of research for decades. The focus of the present investigation is on a planfom having a more complex configuration than a simple delta wing, and for which the existence and nature of leading-edge vortices is unclear. Moreover, it has a well defined wing tip, and separation and stall may occur in this region. This type of flow pattern may contribute to destabilization of the flight mechanics of the UCAV.

1.1 Practical Aspects of 1303 UCAV

The 1303 UCAV was created at the Boeing Phantom Works, under contract to the Air Vehicles Directorate of Air Force Research Labs (McParlin et al, 2003). The 1303 configuration is representative of a variety of UCAVs with blended wing-body configurations (Ol, 2006). The US Naval Air Systems Command (NAVAIR) has investigated the low speed characteristics of the 1303 UCAV (McParlin et al, 2003).

The 1303 is an "edge-aligned", "near-lambda" delta wing which has a concave trailing edge crank at or near the mid-semispan and a convex trailing edge crank. These cranks can cause several problems with aerodynamic performance. The local minimum in the chord from the inboard trailing edge crank causes a local maximum in

the sectional lift coefficient. Similarly, the outboard crank can generate a local minimum in the local lift coefficient (McParlin et al, 2003). Flow separation may occur at or near either of these local extrema and spread rapidly in the outboard direction. This rapid spreading may lead to fully separated flow over the outboard wing panel and any trailing edge devices installed at that location. The loss of effectiveness of outboard control surfaces is associated with a reduction in lateral control authority (McParlin et al, 2003).

For this configuration, as a result of the onset and development of flow separation over the outer portion of the wing, the centroid of lift of the wing may tend to shift inboard and forward. This can result in an occurrence of rapid and unstable pitch-up. This is also called a pitch break situation, in which the curve of the pitching moment vs. angle-of-attack reverses from stable to unstable at an angle-of-attack far below that of the maximum lift coefficient (Ol, 2006). This phenomenon can impose limits on the useable lift. Lower maximum useable lift coefficient indicates greater landing and take-off speeds, which can be an issue for all UCAVs, especially those intended to be used in carrier based operations (McParlin et al, 2003).

1.2 Previous Investigations of 1303 UCAV

This pitch break phenomena can be very critical, and it is hypothesized that some persistent flow separation is the cause (Ol, 2006). To investigate this, a 1303 UCAV model was tested in the QinetiQ low-speed wind tunnel (McParlin et al, 2003).

Pressure tap data from the study demonstrated that the pitch break is due to tip stall with an increase in suction near the apex, possibly from LEV formation from the apex (Ol, 2006). For the "sharp" leading edge case, the pitch break has been shown to occur at $\alpha = 6°$ (Ol, 2006).

The 1303 UCAV configuration with a sharp leading edge was also tested in the AFRL water tunnel in an effort to investigate the possibility of smaller scale water tunnel testing as an alternative to wind tunnels. This study, with the aforementioned pressure distributions in mind, suggests that tip stall may be the main contributor to the "pitch break" phenomenon. LEV formation was not a factor in the water tunnel experiments at $\alpha = 6°$, which is the angle-of-attack for the pitch break onset in the QinetiQ wind tunnel test. It was found that 1303 the UCAV configuration shows signs of tip stall at Re = 32,000, as indicated in the foregoing. Moreover, at this angle-of-attack and Re, the "pitch break" explained earlier is hypothesized to be the result of loss of attached-flow suction at the tip, accompanied by a slight increase in suction near the apex (Ol, 2006). Ol (2006) obtained velocity data from PIV and compared patterns in the tip region with patterns at locations further inboard. He deduced that, at $\alpha = 6°$, the stall region grows from the tip and moves inboard. That is, the flow around the tip is noticeably separated while the flow inboard of the tip is highly attached. It was also stated that a small laminar bubble divides these two regions (Ol, 2006).

Ol (2006) reported that LEV formation was not visualized via dye injection at α = 6°, but at α = 12° and Re = 32,000, a distinct LEV was detected in a single realization. This result is given in Figure 1.1. Ol (2006) found that, at α = 12°, LEV formation can occur in accord with outboard branching of the dye visualization immediately downstream of the apex. On the basis of his experiments, Ol (2006) recommended that dye injection ports be located inside the model, and connected to tubes at the aft end, perhaps near the string amount.

Another study of the flow structure on the 1303 UCAV geometry was performed by Nelson et al (2007). By using a special casting method they were able to place two dye ports inside the wing model. With the dye coming out of two holes on the surface of the wing, located very close to the apex, they were able to visualize the occurrence of a leading-edge-vortex at angles-of-attack $\alpha > 8°$. At lower angles-of-attack, it was concluded that the flow is dominated by a mean flow in the transverse direction. Also there was evidence of considerable reverse flow near the wing tip. This flow structure was referred to as "tip stall" in previous investigations.

1.3. Recent Investigations of Delta Wings of Low-and Moderate-Sweep Angle

Delta wings have been used for several decades in combat and supersonic aircraft. The wings usually have a large sweep angle. However, pure delta wings of small or moderate sweep have been employed less frequently, perhaps due to questions related to the stable and manageable presence of LEVs (Ol and Gharib,

2003). A comprehensive overview of previous related investigations of the flow structure on delta wings of low and moderate sweep angles is beyond the scope of the present study. In the following, selected citations are provided.

Delta wings of low and moderate sweep angles have been researched by Gursul, Taylor and Wooding (2002). They used dye visualization to illustrate the flow patterns over moderately swept delta wings with different planforms. PIV was used in order to quantitatively measure the vortex cores in the crossflow planes. Stereo particle image velocimetry (SPIV) was employed by Ol. and Gharib (2003) to illustrate three-dimensional features of the flow over 50 and 65 degree swept delta wings. They also demonstrated the upstream progression of vortex breakdown with increasing angle-of-attack. Yaniktepe and Rockwell (2004) and Yavuz, Elkhoury and Rockwell (2005) investigated the flow structure in crossflow and near- surface planes for delta wings having relatively low values of sweep angle. The time-averaged flow patterns were accompanied by representations of the flow unsteadiness, including spectral analysis of the structure. Elkhoury and Rockwell (2004) investigated the Reynolds number dependence of vortices on a UCAV planform using dye visualization. The first numerical simulation of the flow structure on delta wings of moderate sweep angle was done by Gordnier and Visbal (2003). Their research illustrated substructures in the shear layer separating from the leading-edge of the wing.

Rullan et al. (2005) investigated the flow on delta wings of 30 and 40 sweep angles and the effect of unsteady blowing at the leading edge of a sharp LE wing. The effect of blowing at the trailing edge was researched by Yavuz and Rockwell (2006).

All of the foregoing investigations, as well as a number of other important, related investigations, provide background for the present study. The planform of the 1303 UCAV is, however, particularly complex, and one expects distinctive features of the flow patterns relative to a simple delta wing.

1.4 Unresolved Issues

The investigations of the 1303 UCAV described in the foregoing have provided an important framework for the present study. Taking into account these investigations, as well as the need for more detailed studies, selected issues may be summarized as follows.

Qualitative visualization using dye injection, extending over a larger extent of the planform, can provide further insight into the flow structure as a function of both angle-of-attack and Reynolds number. In particular, the onset and development of leading-edge vortices, as well as separation bubbles and stall regions, have not been fully clarified.

In cases where a stall region exists, quantitative information on its detailed structure has not yet been obtained. The spatial extent and character of this region along the surface of wing has not been defined in detail. Quantitative representations

along a plane oriented nearly parallel to the wing surface would provide a first level of insight. Furthermore, the manner in which the quantitative structure varies as a function of elevation above the surface of the wing has not been characterized, yet this type of information would be helpful to understand the three-dimensional structure of the stall region. Finally, the instantaneous structure of the stall region, relative to its time-averaged structure, would be informative, as it would provide a physical means for interpretation of the flow unsteadiness.

2. EXPERIMENTAL SYSTEM AND TECHNIQUES

A large–scale, low-turbulence water channel in the Fluid Mechanics Laboratories at Lehigh University was used for the experiments in this study. These experiments include dye visualization and near-surface particle image velocimetry for different angles-of-attack and Reynolds numbers of a 1303 UCAV.

Figure 2.1 gives an overview of the water channel system. It has a test section that is 613 mm wide, 594 mm deep and 5435 mm long. The free surface of the water in the channel is kept at a height of 508 mm. Plexiglas® was used to manufacture the walls of the test section for optical transparency and the reservoirs are made of PVC (polyvinyl chloride). Water that filled the tank was filtered by use of two 1 μm filters to ensure adequate water clarity in the channel for better dye visualization and PIV results.

Upstream of the test section, the flow was conditioned by a honeycomb, a series of four screens and a 3:1 contraction. This conditioning yielded a very low level of free-stream turbulence intensity of less than 0.1%. Perturbations in the flow occurring at locations downstream of the delta wing and sting system were damped by a honeycomb and a settling tank at the downstream end.

The 1303 UCAV model has a leading edge sweep of 47° and a root chord of 177 mm. It has a cranked sharp trailing edge, and aft-rounded tips. This model was made of PVC, and manufactured by a single axis CNC machine in two parts: starboard

and port (left and right). The components of the wing were held together by very viscous silicon grease and two 6 mm brass dowel pins.

The rotational speed of the pump motor is controlled with a controller unit in order to achieve various values of Reynolds number for the experiments. Calibration of the revolutions per minute of the motor to the uniform speed of the water at a given temperature in the water channel was done before the start of the experiments. The calibration is given in Figure 2.2. For a water temperature of 25°C, and freestream velocity U = 51.66, the Reynolds numbers based on chord C was 10,000. A floating thermometer was used to measure the temperature of the water in order to track the changes in viscosity.

A support system was designed and manufactured in order to hold the delta wing in position for different angles-of-attack. Side and plan views of the wing, the support system and dye supply are given in Figures 2.5, and 2.6. A horizontal, a vertical, and a rotational traverse were used to move the wing in two directions and about a single axis. This allowed the wing to be placed at different angles-of-attack with minimal or no changes of the location of the laser sheet. This is a desired advantage for PIV experiments. The angle-of-attack of the wing was measured from its sharp leading-edge, at the starboard side. The alignment laser that is shown in Figures 2.5 and 2.6 is generated by a commercially available laser-compass that emits a thin laser sheet at some angle. The angle of the alignment laser is measured by a magnetic protractor, which measures the angle of some object by taking the direction

of the gravitational force as a zero reference. When this thin laser sheet exactly matches the leading-edge of the wing the wing, it is assumed to be at the same angle as the alignment laser.

Dye visualization technique was used in order to visualize the flow structures on the 1303 UCAV. A mixture of a generic food dye and tap water with an approximate 1:8 ratio of dye to water was used. The mixture was inserted through the dye ports inside the wing. Dye was carried through these four dye ports and was injected to the flow through the four holes on the surface of the wing. These holes are located at 0.03, 0.1, 0.2 and 0.3 chord-wise locations, and they are placed to be as close to the leading-edge as possible. Each dye hole had a diameter of 1 mm.

A dye supply with flow rate control was used in order to achieve a constant dye flow. During the experiments it was observed that larger flow rates of dye through the dye ports deflected the dye pattern away from the surface of the wing. As one expects, large quantities of dye are needed in order visualize the flow structure, such as leading-edge vortices or tip stall. So, for each experiment, an optimum dye flow was used, while making sure that the injected dye remained sufficiently close to the surface.

Particle image velocimetry technique was used for quantitatively visualizing the flow structure on the 1303 UCAV. This technique consists of generating a sequence of instantaneous velocity fields over the area of interest (field of view) without generating any disturbance in the flow field. Reviews of the advances of this

technique have been published by Adrian (1986, 1988) and Westerweel (1993, 1997). In this study, a TSI-based digital particle image velocimetry system was used. Figure 2.4 is a representation of the overview of the experimental components of the DPIV system. It includes a TSI synchronizer (model 610032); a 90 mJ Nd:Yag double-pulsed laser system (532 nm); a CCD digital camera model PowerView^{TM} 2M+ (60057) ; a frame grabber model 600070; and Insight^{TM} software version 6.0. The flow was seeded with 12 micron metallic-coated hollow plastic spheres which have nearly neutral buoyancy. The seeding density was sufficient for high image density PIV. These particles were illuminated with two short duration laser pulses by the dual pulsed Nd: Yag laser. The maximum repetition rate of each laser head is 30 Hz. In this study, a 15 Hz repetition rate was used.

A digital charge-coupled-device (CCD) camera along with a frame grabber card was used to capture and record the particle images. The resolution of the camera was 1600 x 1200 pixels. However, due to the limited capacity of this particular frame grabber, only approximately 40 percent of the capture area could be used for experiments at the 15 Hz sampling rate. If a larger capture area were to be used, the images captured by the frame grabber would be slightly off from the actual pulses of the laser, which resulted in bad velocity fields. However the smaller capture area did not raise an issue about resolution of the PIV because the tip stall region investigated is fairly small, about the size of a 45 mm x 60 mm rectangle. Also the lack of speed of the frame grabber created no problems for dye visualization tests. The camera was

equipped with a lens of focal length 28 mm for dye visualization experiments, which gives a larger field of view that encompasses the entire half wing. For the PIV experiments, a lens of focal length 60 mm was used. Figure 2.7 illustrates the interrelationship of the DPIV components.

Considering that 1303 UCAV configuration is symmetric, flow visualization and PIV were performed only for one half of the wing. In order to obtain a thin laser sheet, two -15 mm focal length cylindrical lenses and a spherical lens of 500 mm focal length were used respectively. The laser sheet was approximately 3/4 mm thick at the center of the half wing. The center of the laser sheet was located at several positions starting at an elevation of 1 mm from the wing surface and extending up to 20 mm in some cases. The laser sheet at 1 mm away from the surface corresponds to Δ/C = 0.006, where C is the chord.

The instantaneous velocity fields are generated by interrogating a pair of single-exposed frames by utilizing a spatial frame-to-frame cross-correlation technique for the time period between the two laser pulses. The Hart correlation technique was used in this study because of the shorter processing time needed to complete the correlations. The interrogation window size was 32 pixels x 32 pixels. In order to satisfy the Nyquist criterion, 50% overlap was used during the interrogation process. The effective grid size in the plane of the laser sheet was approximately 80 mm x 90 mm. A total of 200 instantaneous image couples were obtained for each experiment.

Post-processing of raw velocity fields followed the schematic which is shown in Figure 2.8. Validation data was done by utilizing the software CLEANVEC. CLEANVEC was utilized in order to perform vector validation according to the following criteria: root-mean-square fluctuation, absolute range, magnitude difference and median magnitudes.

The NFILVB program created by Lin (1994) of the Fluid Mechanics Laboratories was used to fill the missing vectors that were removed by the CLEANVEC program earlier in the post-processing. NFILVB applies a bilinear interpolation technique with a least squares fit. This program also evaluates the instantaneous vorticity fields which were not used in the current study. In addition, data smoothing with an axisymmetric Gaussian smoothing kernel with parameter σ = 1.3 was utilized to reduce the error-based deviations.

The mean (time-averaged) velocity fields were generated by the in-house program NWENSAV2 which was formulated by Lin (1996).

The data were transformed to the final formats by utilizing Tecplot 360; these formats include velocity vectors, contours of streamwise and transverse velocity both in instantaneous and averaged form, as well as root-mean-squares of streamwise and transverse velocity. The images in this thesis were prepared using CorelDRAW. The overview of the entire post-processing procedure is given in Figure 2.8.

In short, the aim of this study was to investigate the flow patterns on a 1303 UCAV. Experimental results are given in the sections that follow.

3. DISCUSSION OF RESULTS

3.1 Dye Visualization

Figures 3.1 through 3.5 show the patterns of dye visualization along the scale model of the 1303 UCAV over a Reynolds number range of Re = 1.0 x 10^4 to 5.0 x 10^4, and for angles-of-attack α = 4°, 6°, 9° and 12°. Figure 3.1 shows the flow of dye in the transverse direction, from the mid-plane towards the tip of the delta wing, at angles-of-attack α = 4° and 6°, and at Reynolds numbers Re = 10,000, 30,000 and 50,000.

Figure 3.1 shows that the first formation of a very distinct LEV is at angle-of-attack α = 6° and Reynolds number Re = 50,000. At angles-of-attack α = 9° and 12°, distinctive LEV formation can be seen at a value of Reynolds number Re = 30,000.

Figure 3.2 demonstrates the Reynolds number dependence of the onset the of LEV formation along a 1303 UCAV. For α = 9° and 12° the onset of formation of the LEV progresses upstream as the Reynolds number increases from 30,000 to 50,000. The LEV formation begins from the apex at 12° angle-of-attack and a value of Reynolds number of 50,000.

Patterns of dye visualization at constant Reynolds number and various values of angle-of-attack are given in Figures 3.3 through 3.5. Figure 3.5 shows the sensitivity of the onset of the LEV formation to changes in the angle-of-attack at a Reynolds number Re = 50,000. While there are no signs of a LEV at angle-of-attack α

= 4°, it does occur at α = 6°. For α = 9° and α =12° at Re = 50,000, there is clear evidence of LEVs originating from upstream locations of the leading-edge. From Figure 3.5, it can be observed that for a Reynolds number Re = 50,000 at α = 6°, the onset location of the LEV is located between the third and fourth holes away from the apex. At 9°, the onset of the LEV formation is at a location between the first and second holes, while at 12° the LEV formation occurs very close to the apex.

As it is shown in Figure 3.1, signs of tip stall can be seen even at the angle-of-attack α = 4° and Reynolds number Re = 10,000. Figure 3.1 illustrates that the center of the stall region moves upstream as Reynolds number increases. At α = 4° and Re = 50,000, the flow over the tip region is fully separated. In Figure 3.3, one can see that the stall region moves upstream and also inboard with increased angle-of-attack, generating a large circulating flow region that can be visualized only at Re = 10,000, which is prior to the occurrence of the LEV.

3.2 Particle Image Velocimetry

In this section, the results of near-surface, high image density digital PIV are discussed. These results are given by Figures 4.1 through 8.3. The Reynolds number based on chord is 50,000 for all cases. Near-surface PIV was done at different locations away from the surface. The distance from the surface Δ is normalized by chord C. The orientation of the laser sheet and proximity of the laser sheet to the surface are given in Figure 2.3. In addition, images 4.1 through 5.3 and 7.1 through

7.3 include a small figure that indicates the orientation of the laser sheet. The location of the cross-section in the side image is designated by the orange dashed line. An approximate representation of the field of view is given by the black dashed rectangle.

Figures 4.1 through 4.3 show the time-averaged velocity vectors along the 1303 UCAV. These patterns of vectors indicate a region of stalled flow. The contour of the delta wing surface is designated by the dashed curve. The high speed region close to the leading-edge is caused by the orientation of the laser sheet and also the increased flow speed of the freestream in that region. As can be seen from the small figures at the bottom right, the laser sheet is farther away from the surface near the leading-edge than the trailing-edge. Due to the three-dimensional model that is being investigated, the laser sheet was placed in a way that it would adequately visualize the area of the tip stall region that was found from the dye visualization results. Another interesting point shown in these figures is that flow in the transverse direction is apparent at angles-of-attack α = 9° and 12° at a Reynolds number Re = 50,000, even though dye visualization experiments did not reveal it.

Figures 5.1 through 5.3 show the streamwise velocity contours normalized by the freestream velocity. Velocity measurements at different distances from the surface at α = 6° are given in Figure 5.1. As can be seen from the images, the scale of the stalled region decreases as the measurement surface is located further away from the wing surface. Also, it can be observed that the center of the stalled region moves downstream with increased distance from the surface. The same argument can be

made for Figures 5.2 and 5.3 which show patterns of velocity for the cases $\alpha = 9°$ and $\alpha = 12°$. Comparing the images at the same distance from the surface and for 6°, 9° and 12° degrees, it can be seen that the stalled region increases in scale by moving inboard and upstream with increased angle of attack. Figures 5.1 through 5.3 also show a change in the scale of the stalled region in the z direction. For $\alpha = 6°$ and $\Delta/C = 0.024$, the flow attains half the freestream velocity in the stall region. At, higher angles-of-attack, this distance is $\Delta/C = 0.048$ for $\alpha = 9°$ and $\Delta/C = 0.084$ for $\alpha = 12°$.

Figures 6.1 through 6.3 show stacked arrangements of the images of 5.1 through 5.3. The interpretations given in the foregoing are also evident in this arrangement of images.

Figures 7.1 through 7.3 include instantaneous images that represent extreme instantaneous patterns of the contours of constant streamwise velocity taken and velocity vectors from the cinema sequence. These patterns provide a basis for interpretation of the patterns of root-mean-square velocity fluctuation, to be shown subsequently. In addition, Figures 7.1 through 7.3 provides patterns of time-averaged vectors of velocity and contours of streamwise and transverse velocity. Comparison of these patterns with the aforementioned instantaneous patterns reinforces the point that the instantaneous flow structure exhibits substantial excursions from the time-averaged structure. This observation also holds for angles-of-attack of 9° and 12°, given in Figures 7.2 and 7.3. Taken together, all of the foregoing observations indicate that the scale of the region of stalled flow, as well as the magnitude of the

velocity fluctuations, are highly time-dependent, for all angles–of-attack. Furthermore, from the time-averaged transverse velocity contours given in Figures 7.1 through 7.3, it can be asserted that there is a considerable flow in the transverse direction, that is, in the outboard direction along the span of the wing. The magnitudes of the transverse velocities increase with the increasing angle-of-attack, and the location of the largest transverse velocity moves inboard as the angle-of-attack increases.

Figures 8.1 through 8.3 give the root-mean-square values of streamwise and transverse velocity components, u_{rms} and v_{rms}. Figure 8.1 shows the time-averaged streamwise velocity contours at different distances from the surface. From Figure 8.1 it can be seen that the u_{rms} values are actually smaller within the aforementioned stall regions where there is smaller streamwise velocity. There is a relatively high u_{rms} region close to the leading edge, which indicates that this region undergoes large amplitude fluctuations. This region of higher values of u_{rms} moves downstream with increasing distance from the surface of the wing, and it stretches inboard with increased angle-of-attack.

Figure 8.2 shows the v_{rms} contours for the same distances from the surface and the same angles-of-attack as in the foregoing. One observation is that the region of higher v_{rms} moves inboard with increasing values of angle-of-attack. Contrary to the observation for the aforementioned u_{rms} values, the v_{rms} values decrease in magnitude with increasing distance from the surface of the wing for angles-of-attack α = 6° and 9°.

4. CONCLUSIONS

The goal of this investigation is to understand the flow physics associated with the flow along a 1303 UCAV. The focus was on the formation of the LEV and the stall occurring at the wing tip.

It was found that there is an indication of LEV formation as early as an angle-of-attack $\alpha = 6°$. The results of dye visualization showed that tip stall is apparent at all angles-of-attack, and it moves in the upstream direction and inboard as the angle-of-attack or Reynolds number increases.

Near-surface PIV was employed to characterize the physics of tip stall. The scale of the stall region varies with angle-of-attack and the distance from the surface of the wing. The center of the stalled region moves upstream as angle-of-attack increases, and is located further downstream with the increasing distance from the surface of wing. Moreover, the scale of the stalled region increases with increasing angle of attack, but decreases with increasing distance from the wing. Also, it was shown that the stall region increases in scale in the surface normal direction as the angle-of-attack increases.

This stall region in the vicinity of the tip is also highly time-dependent. That is, its instantaneous structure shows large departures from the time-averaged structure. These departures correspond to relatively large magnitudes of the root-mean-square values of the streamwise and transverse velocities.

5. RECOMMENDATIONS FOR FUTURE INVESTIGATIONS

In future investigations, the flow structure at higher Reynolds numbers of the order of 100,000 should be addressed. It might be possible to find signs of LEVs at smaller values of angle-of-attack α, relative to the minimum value of $\alpha = 6°$ for the present range of Reynolds number. Also the effect of flow control methods such as applying small perturbations to the wing or blowing through the surface of the wing at appropriate locations might give valuable information on control of the physical phenomena described in the foregoing. Furthermore, use of PIV and the crossflow plane might be helpful to gain further understanding of the tip stall region.

FIGURES

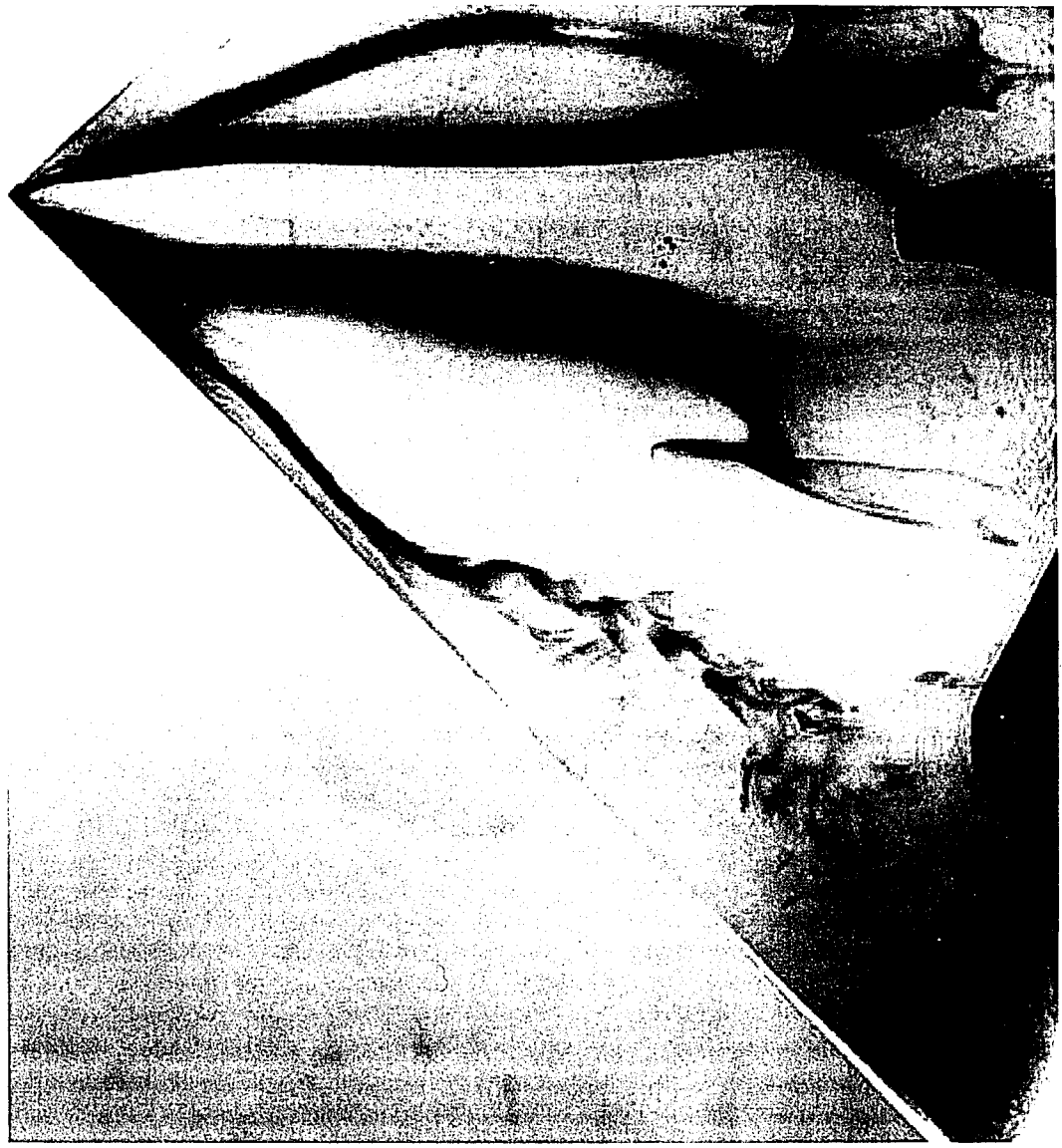

Figure 1.1: Dye visualization of flow structure at angle-of-attack $\alpha = 12°$ and for a value of Reynolds number Re = 32,000 based on chord (Ol, 2006).

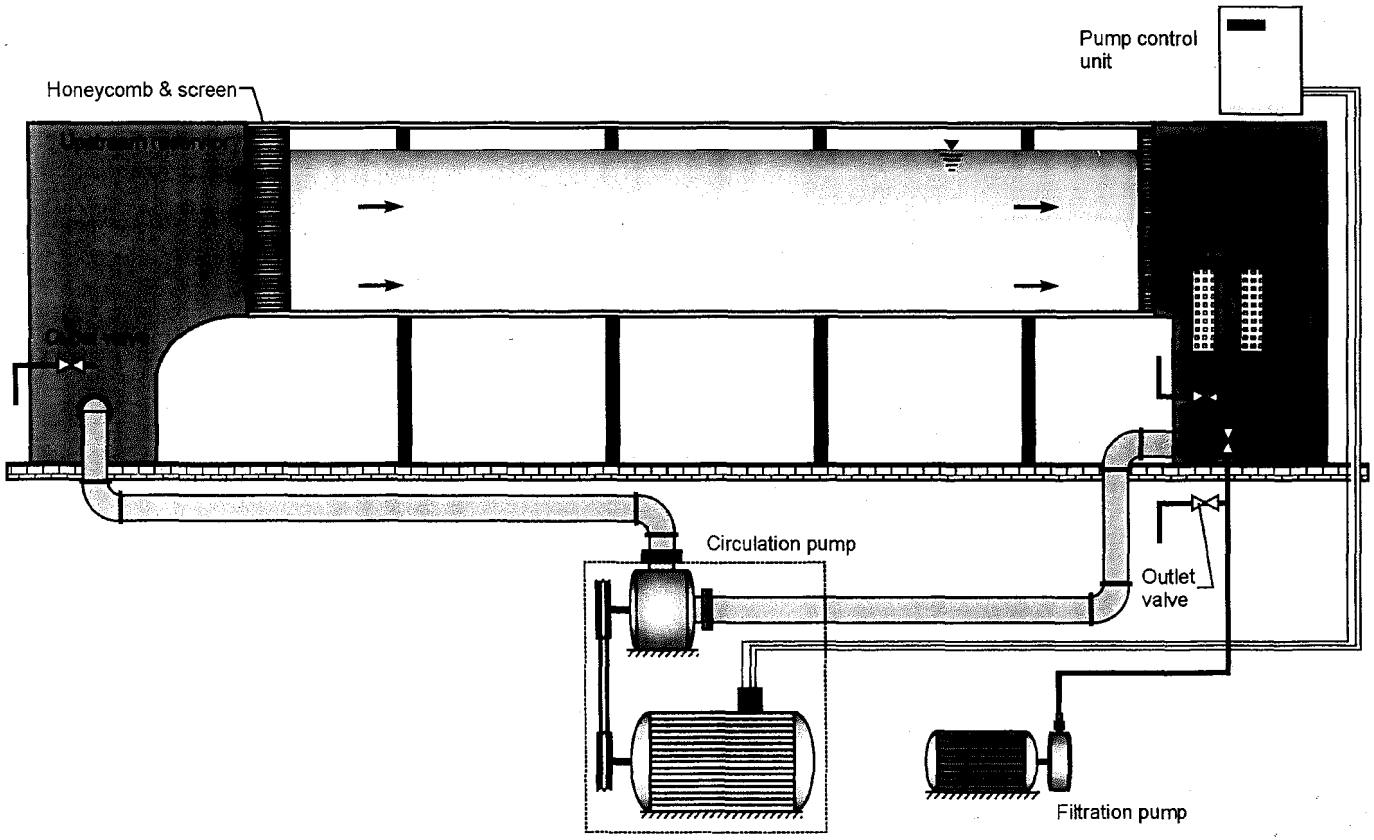

Figure 2.1: Schematic of the recirculating type free-surface water channel facility.

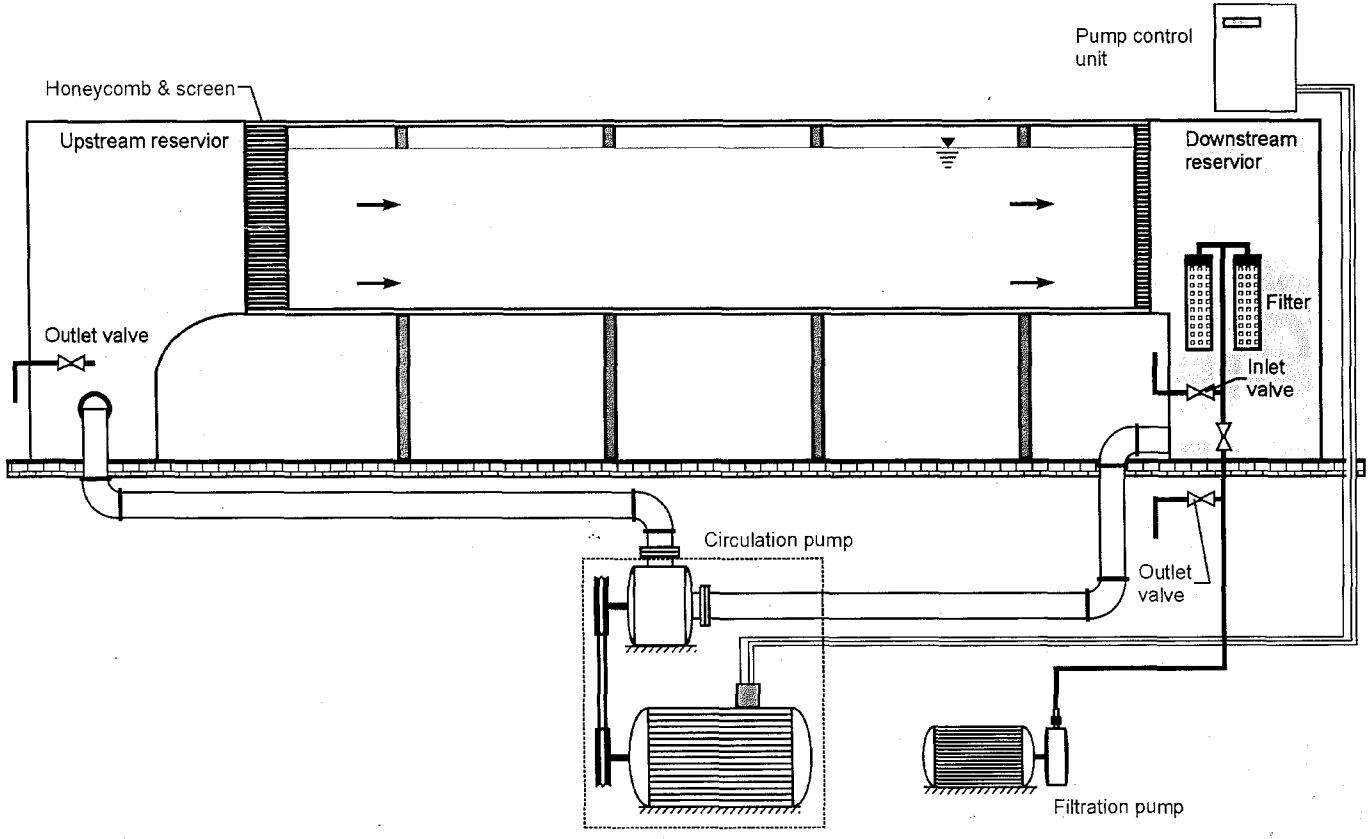

Figure 2.1: Schematic of the recirculating type free-surface water channel facility.

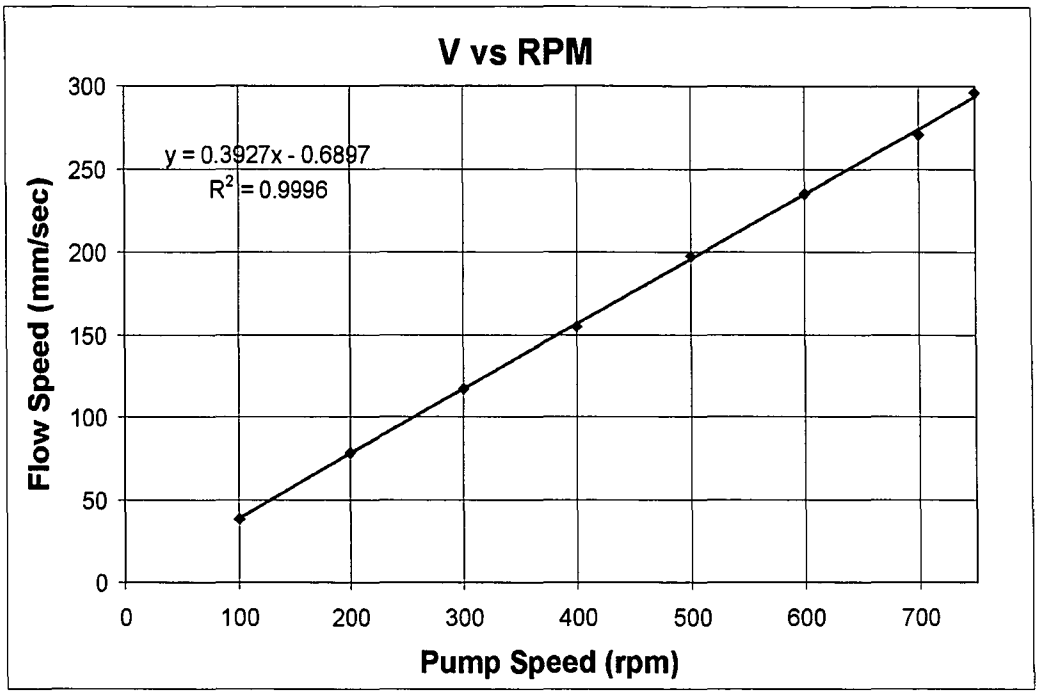

Figure 2.2: Channel calibration curve.

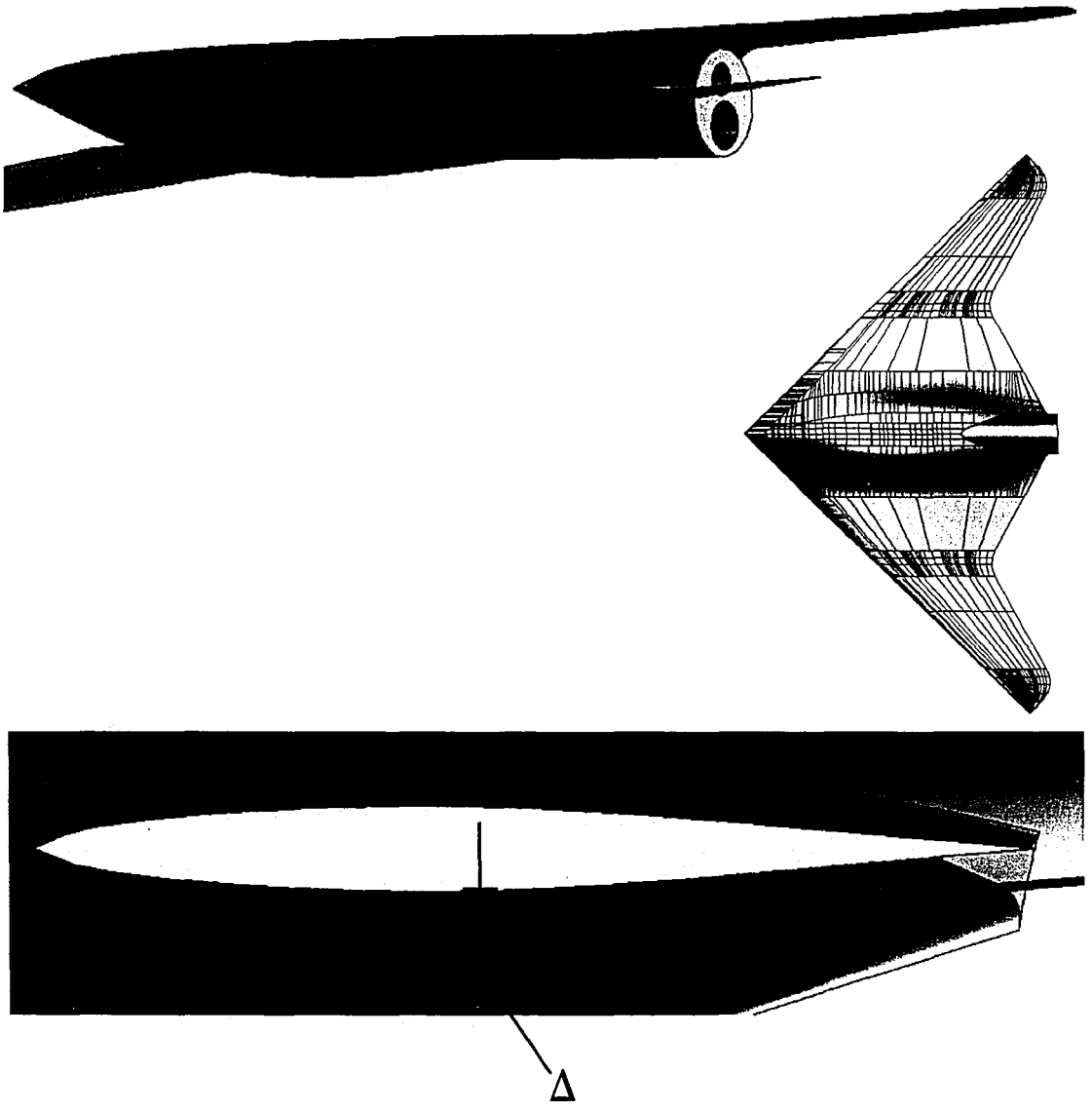

Figure 2.3: Solid model representations of 1303 UCAV and designation of location of laser sheet.

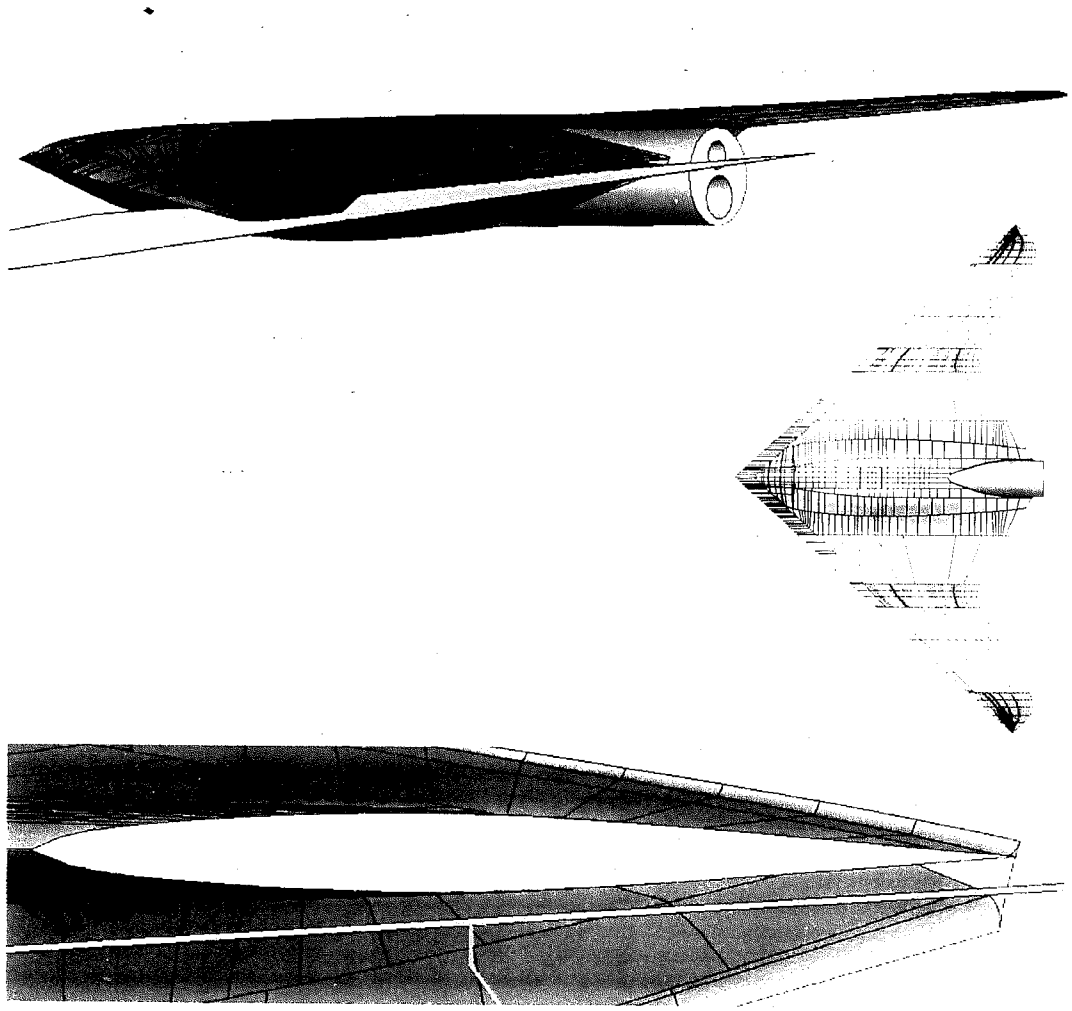

Δ

Figure 2.3: Solid model representations of 1303 UCAV and designation of location of laser sheet.

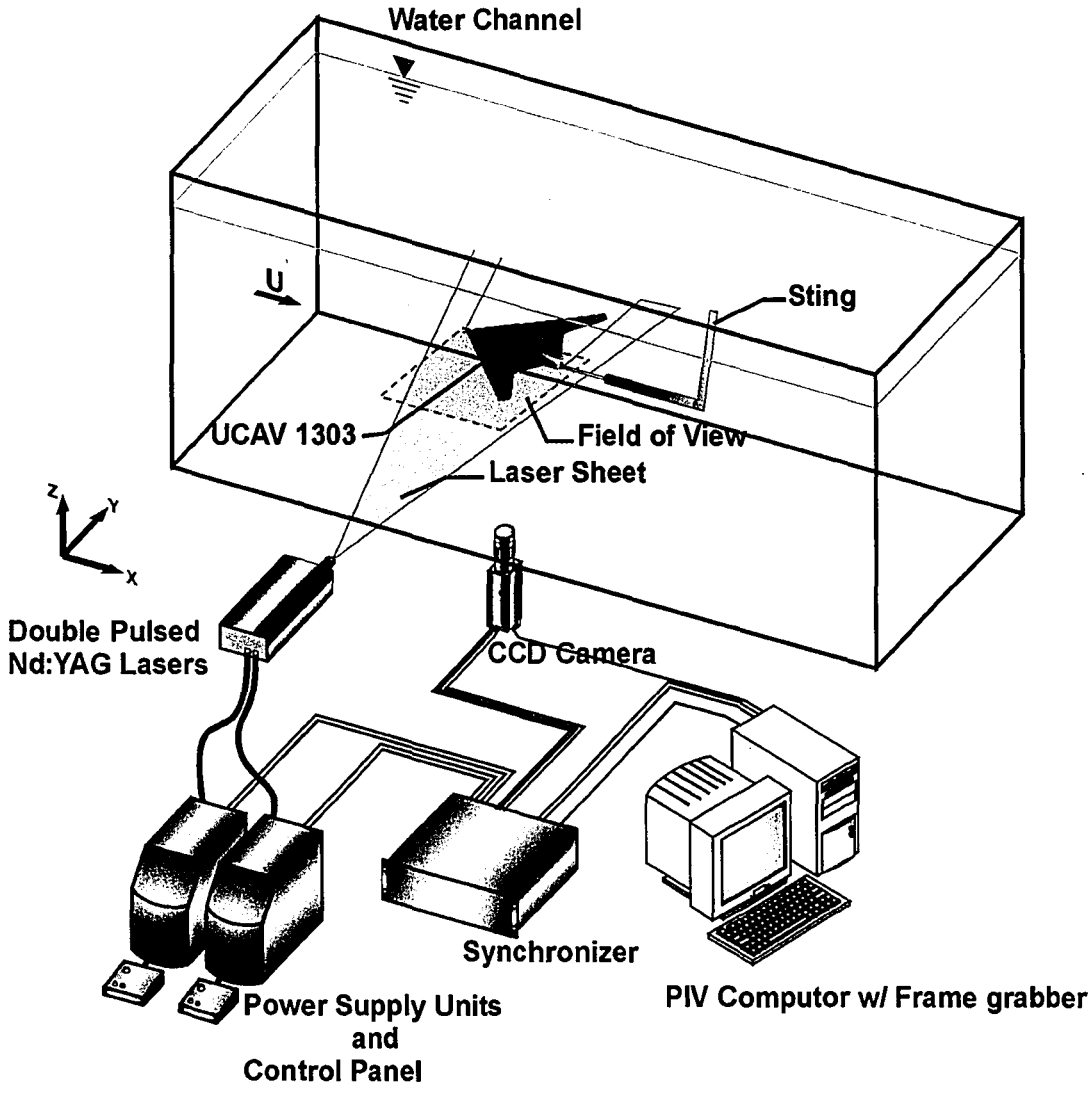

Figure 2.4: Overview of experimental system, and instrumentation.

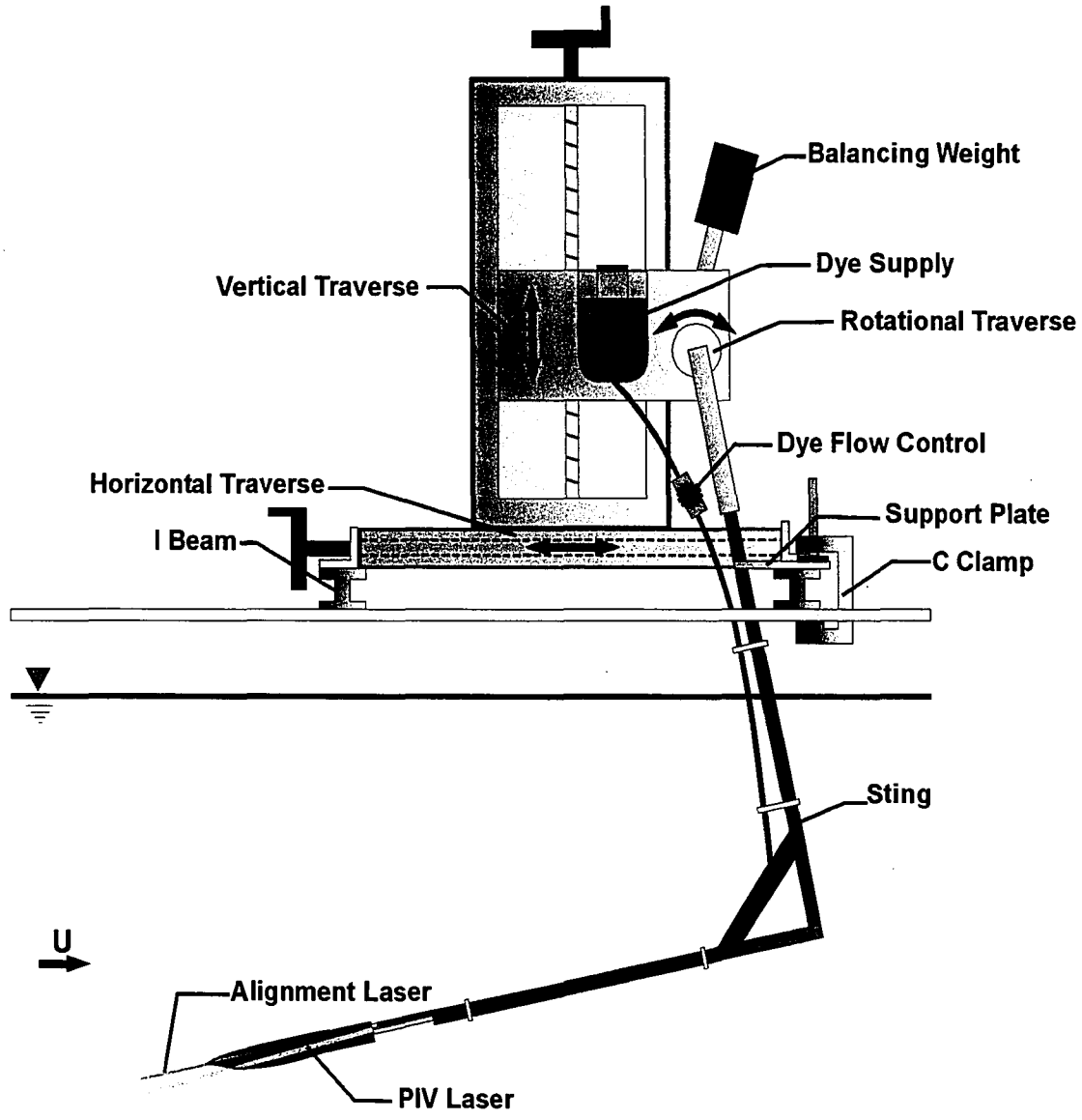

Figure 2.5: Side view of experimental system.

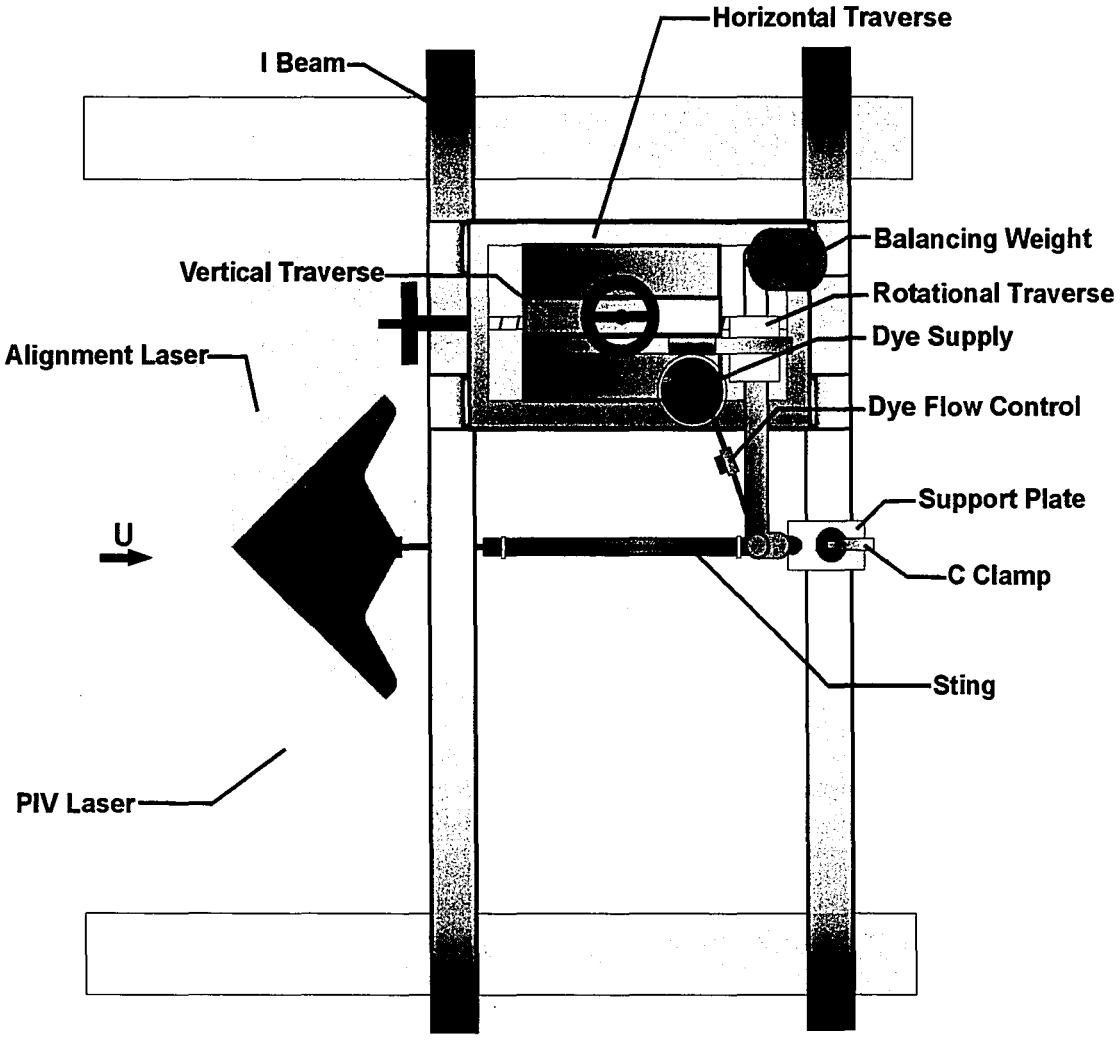

Figure 2.6: Plan view of experimental system

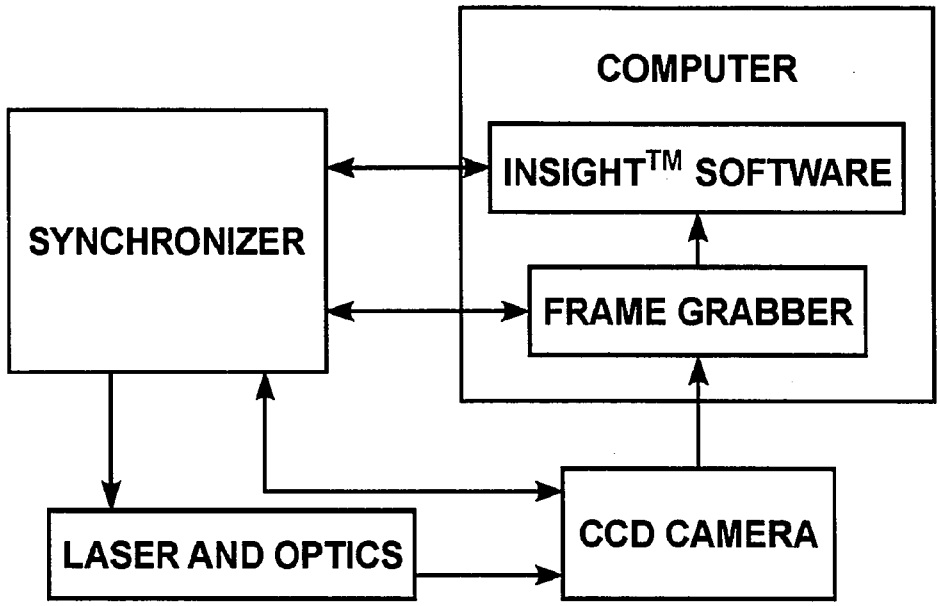

Figure 2.7: Interrelationship of Digital Particle Image Velocimetry (DPIV) components.

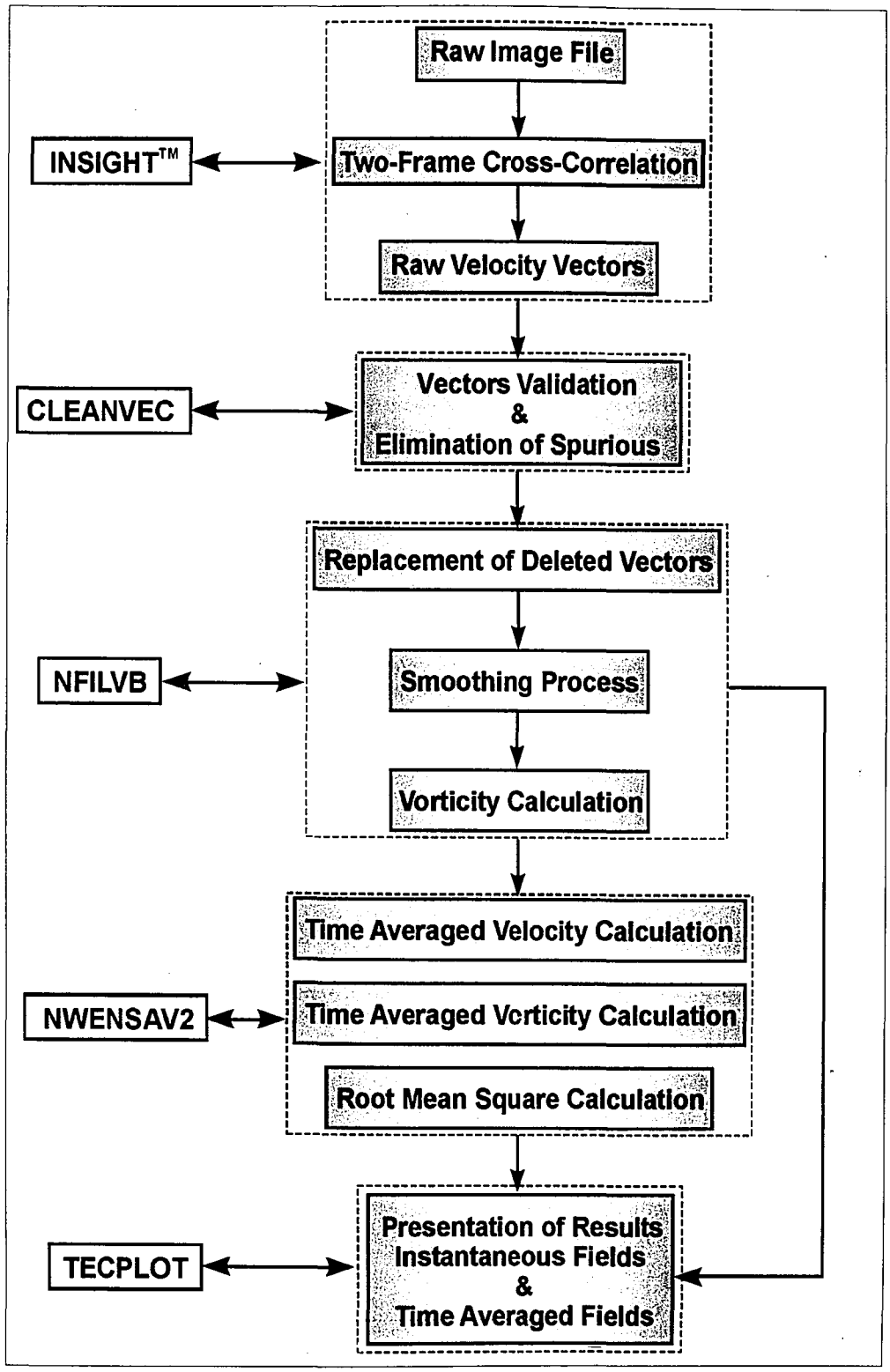

Figure 2.8: Flow chart of DPIV processing and post-processing.

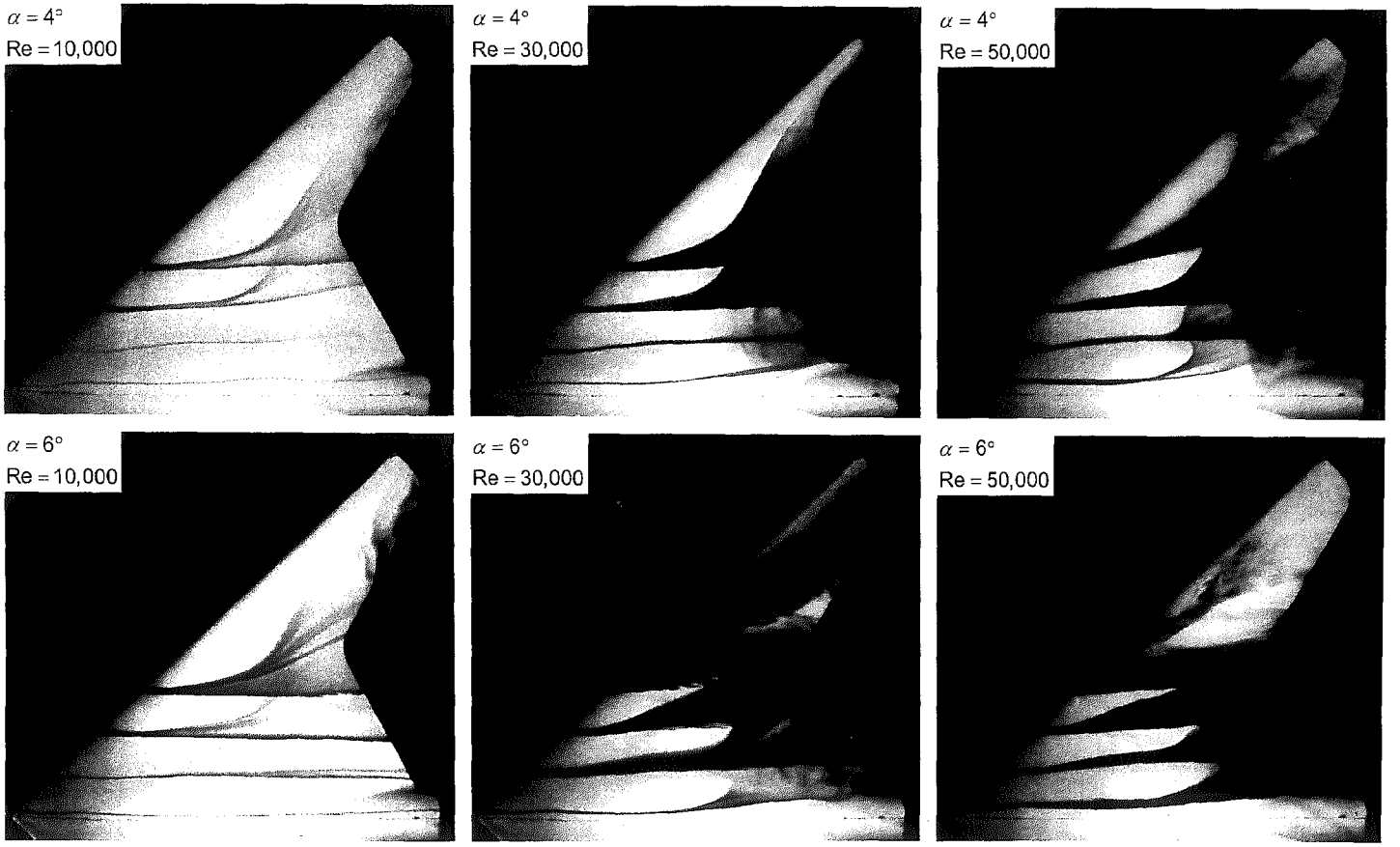

Figure 3.1: Dye visualization of flow structure at angle-of-attack $\alpha = 4°$ and $\alpha = 6°$ for values of Reynolds number Re = 10,000, 30,000, 50,000 based on chord.

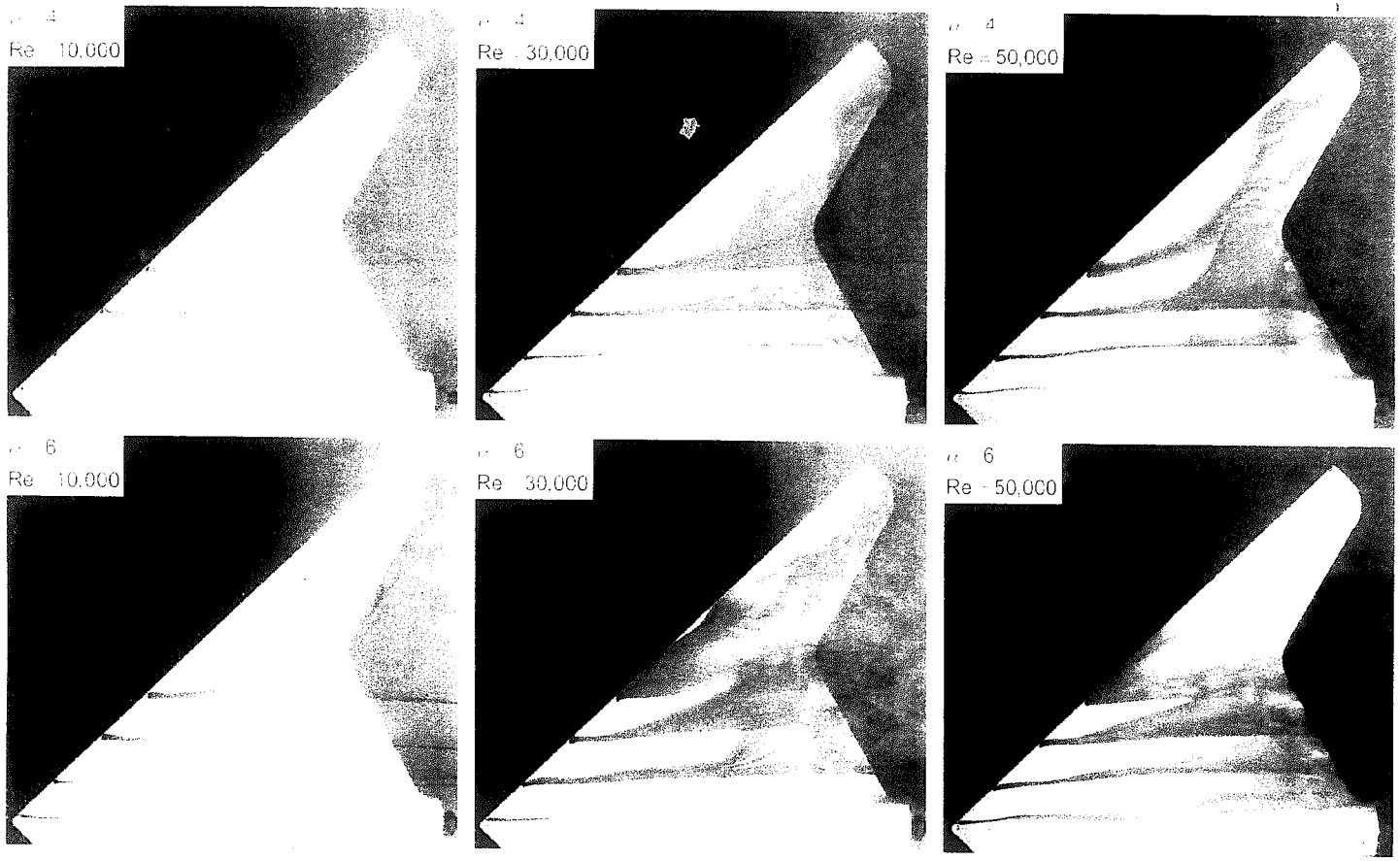

Figure 3.1: Flow visualization of flow structure at angles-of-attack $\alpha = 4$ and $\alpha = 6$ for values of Reynolds number Re = 10,000, 30,000, 50,000 based on chord.

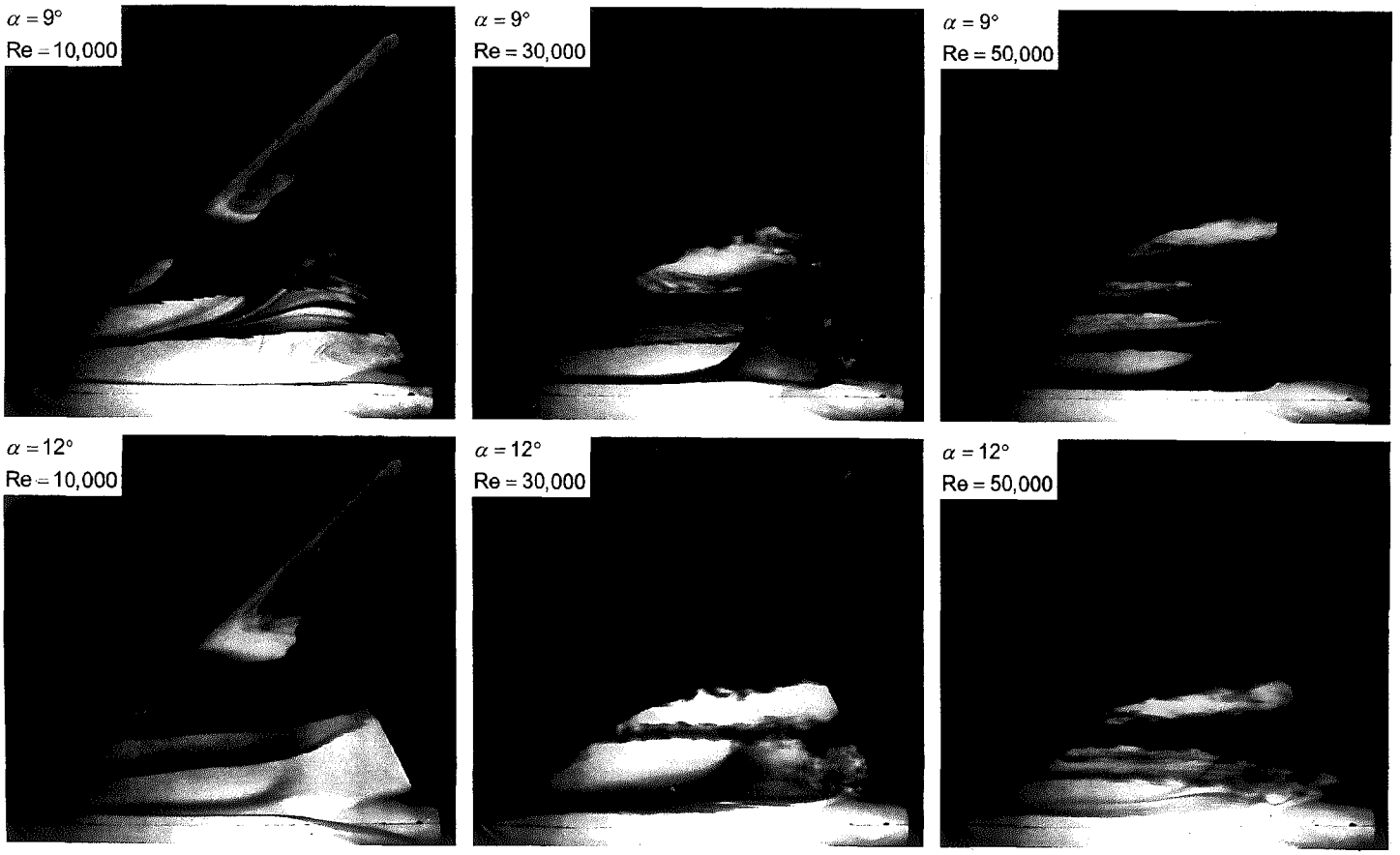

Figure 3.2: Dye visualization of flow structure at angle-of-attack $\alpha = 9°$ and $\alpha = 12°$ for values of Reynolds number Re = 10,000, 30,000, 50,000 based on chord.

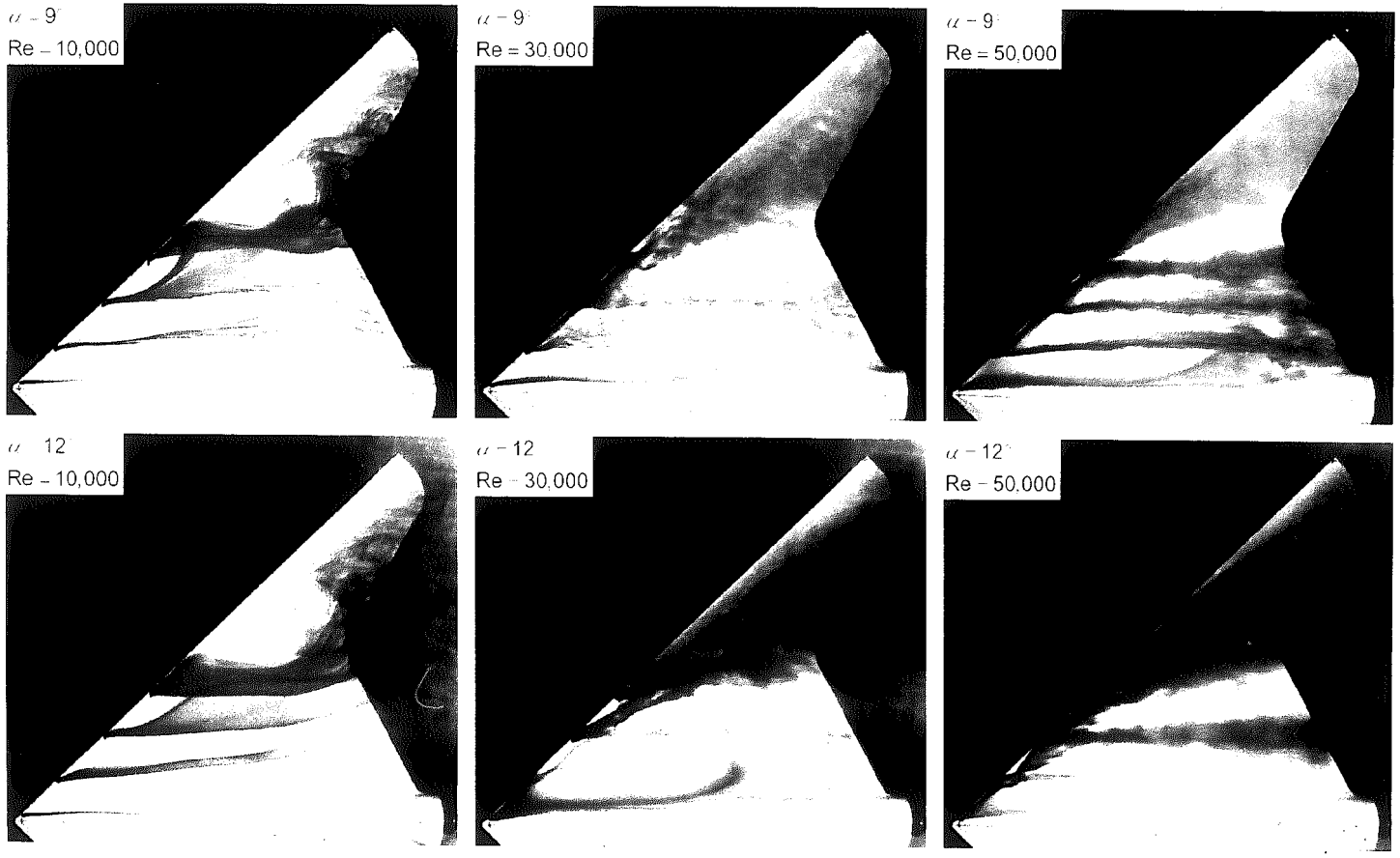

Figure 3.2: Dye visualization of flow structure at angle-of-attack $\alpha = 9°$ and $\alpha = 12°$ for values of Reynolds number Re = 10,000, 30,000, 50,000 based on chord

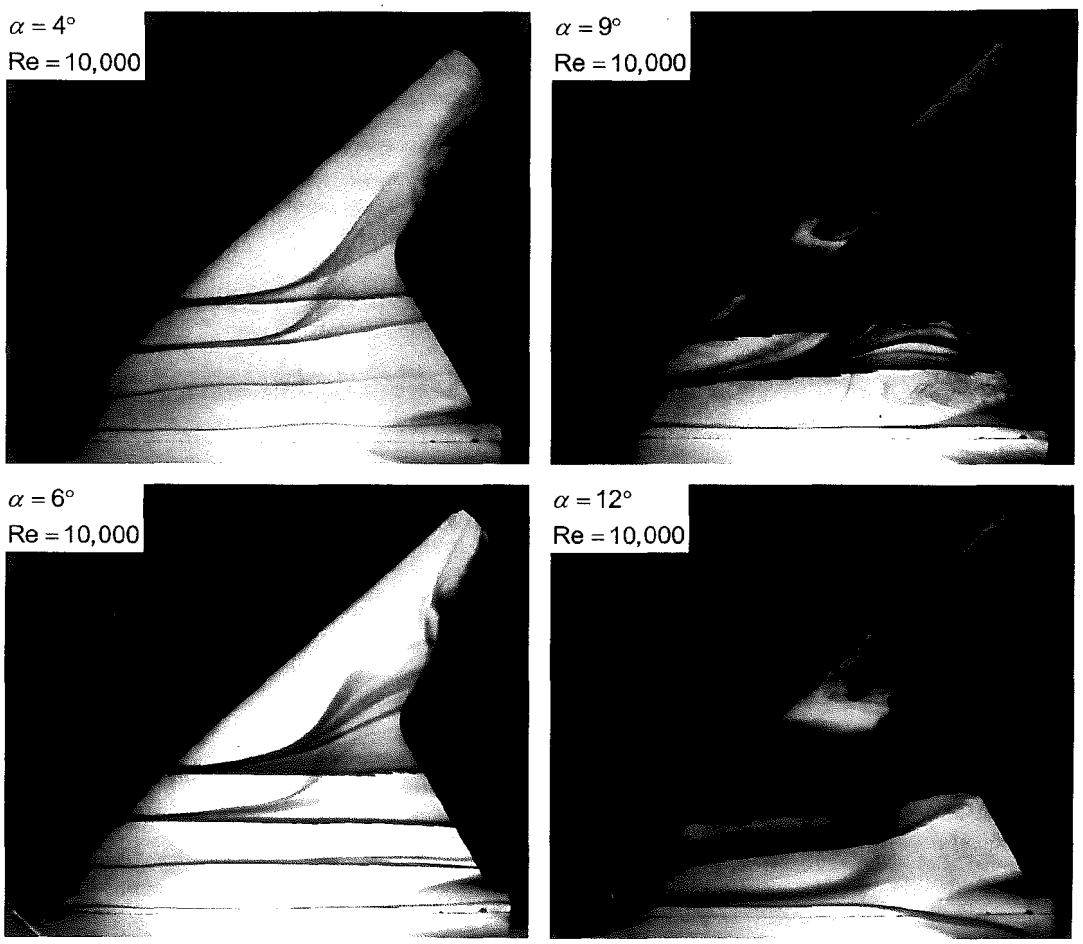

Figure 3.3: Dye visualization of flow structure for angles of attack α = 4°, 6°, 9° and 12° at a value of Reynolds number Re = 10,000 based on chord.

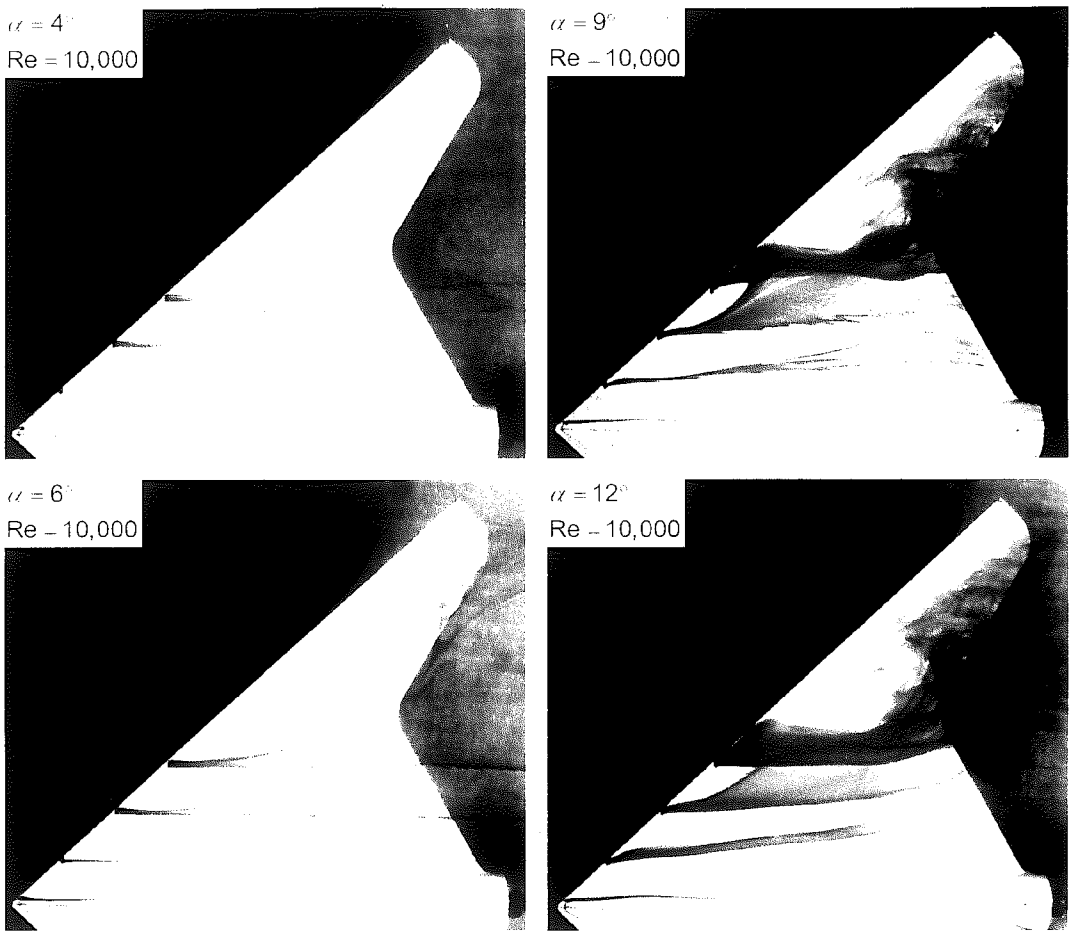

Figure 3.3: Dye visualization of flow structure for angles of attack $\alpha = 4°, 6°, 9°$ and $12°$ at a value of Reynolds number Re = 10,000 based on chord.

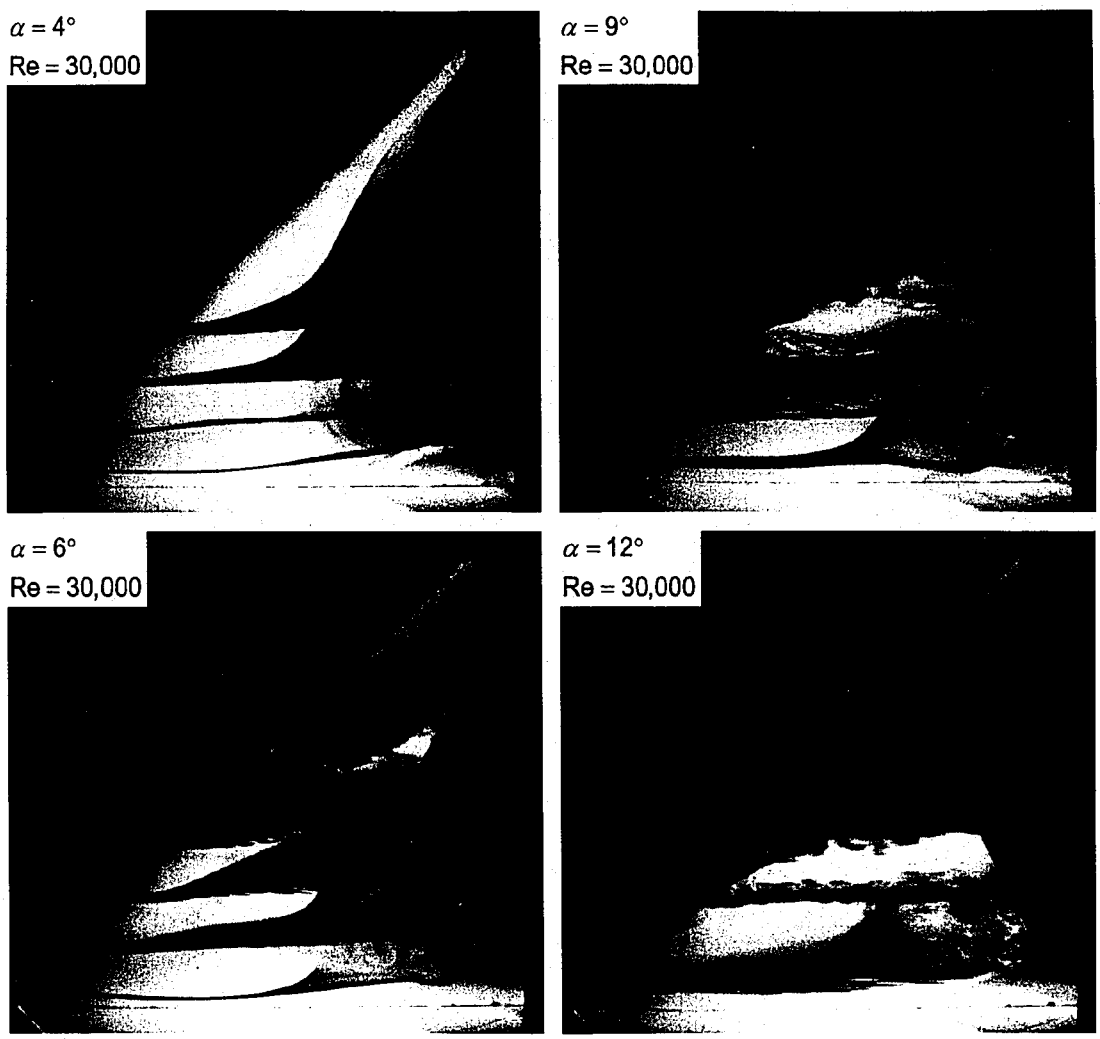

Figure 3.4: Dye visualization of flow structure for angles of attack $\alpha = 4°$, 6°, 9° and 12° at a value of Reynolds number Re = 30,000 based on chord.

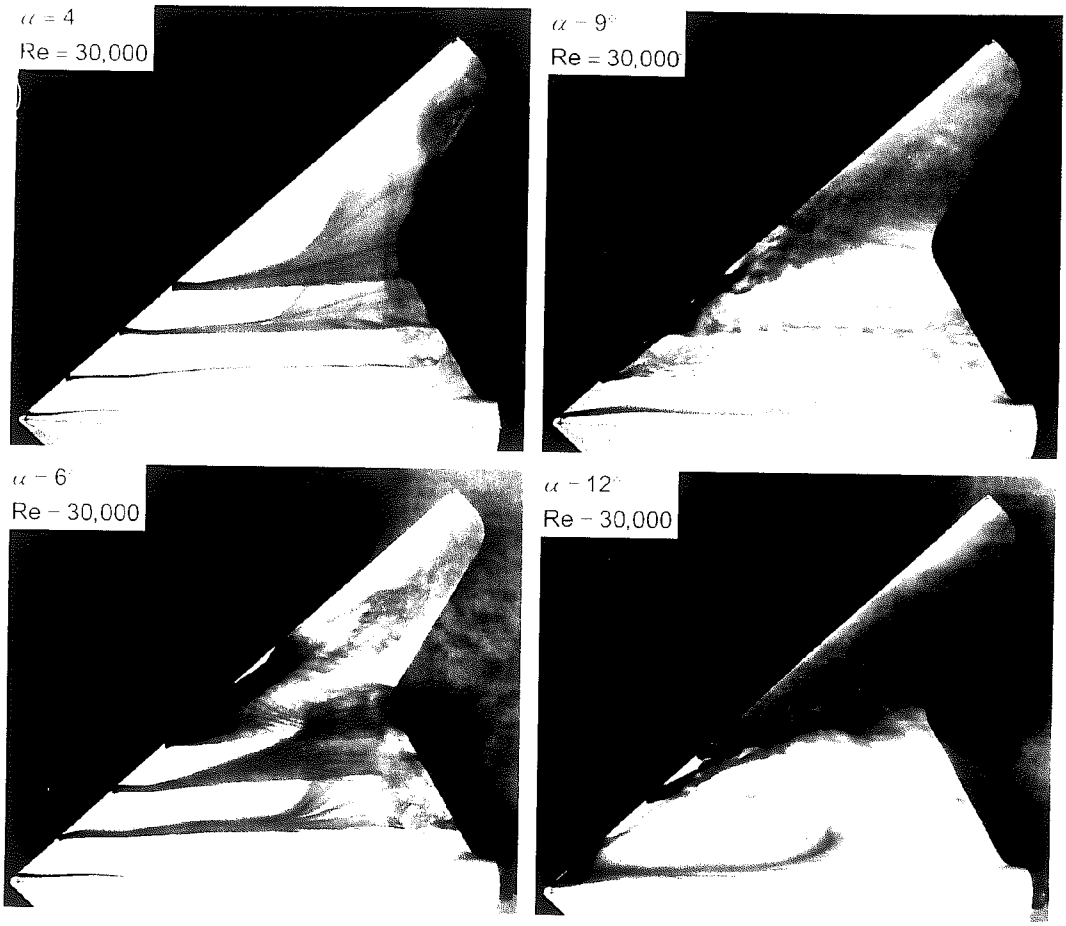

Figure 3.4: Dye visualization of flow structure for angles of attack $\alpha = 4°, 6°, 9°$ and $12°$ at a value of Reynolds number Re = 30,000 based on chord.

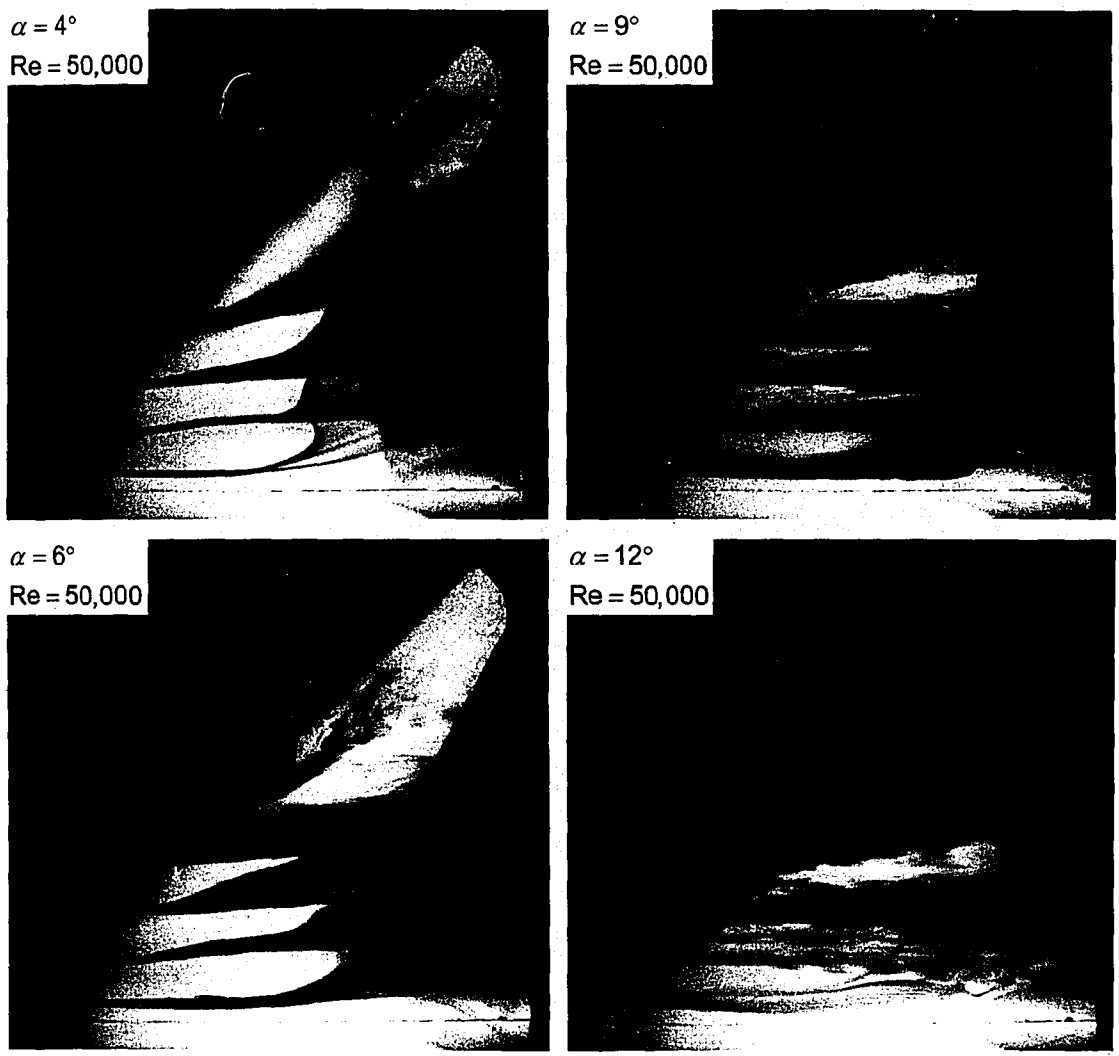

Figure 3.5: Dye visualization of flow structure for angles of attack $\alpha = 4°$, 6°, 9° and 12° at a value of Reynolds number Re = 50,000 based on chord.

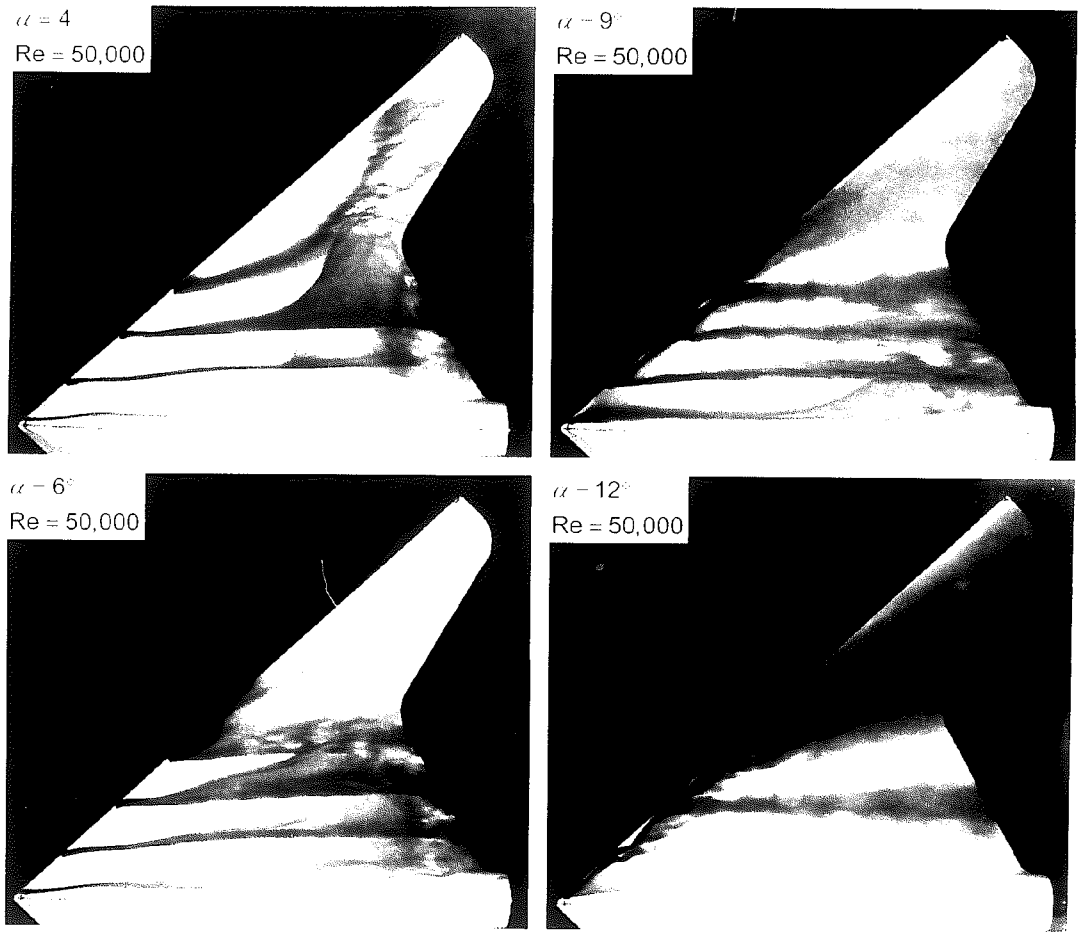

Figure 3.5: Dye visualization of flow structure for angles of attack $\alpha = 4°$, 6°, 9° and 12° at a value of Reynolds number Re = 50,000 based on chord

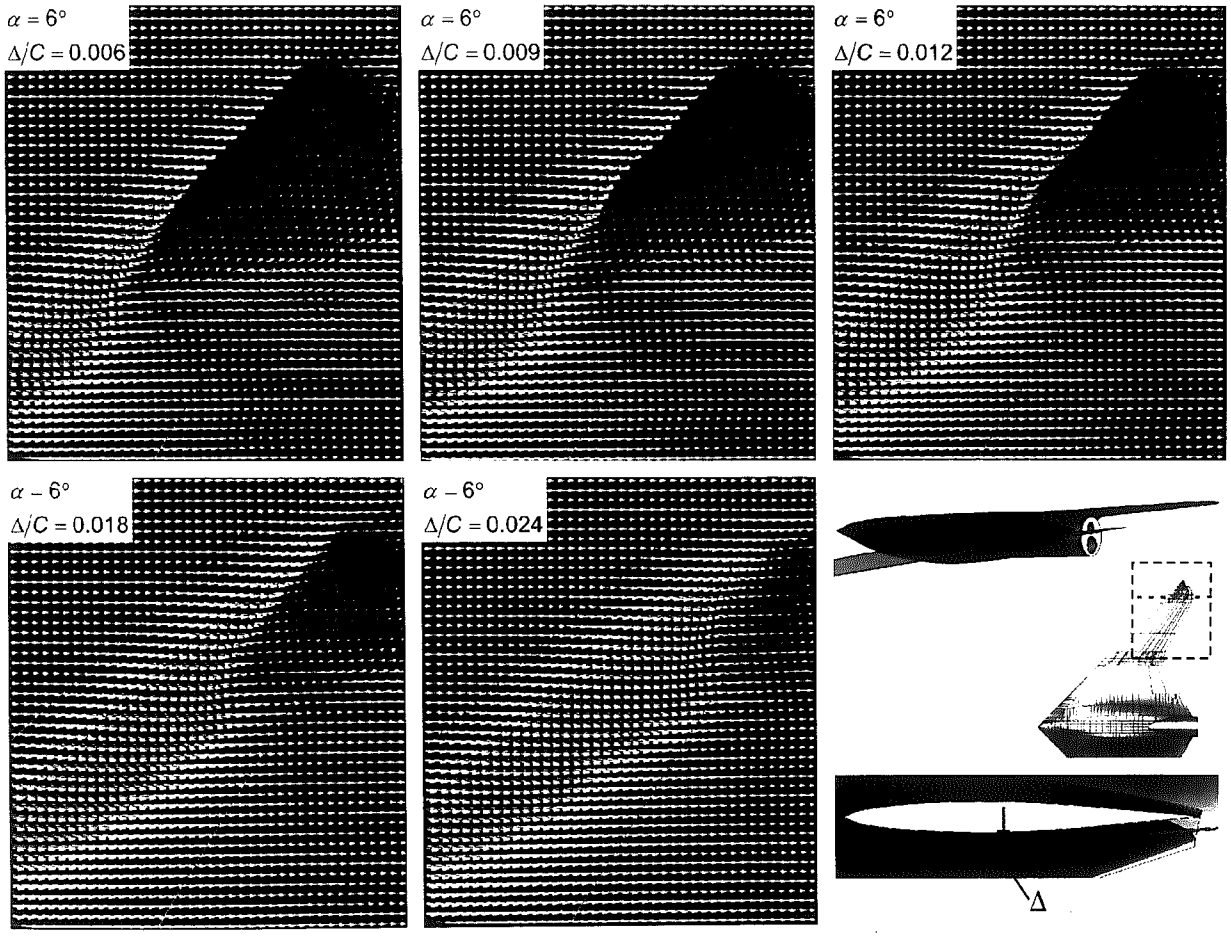

Figure 4.1: Time-averaged velocity vectors $\langle \underline{V} \rangle$ for different values of displacement Δ/C of laser sheet from surface of wing at angle-of-attack $\alpha = 6°$. Reynolds number Re = 50,000 is based on chord.

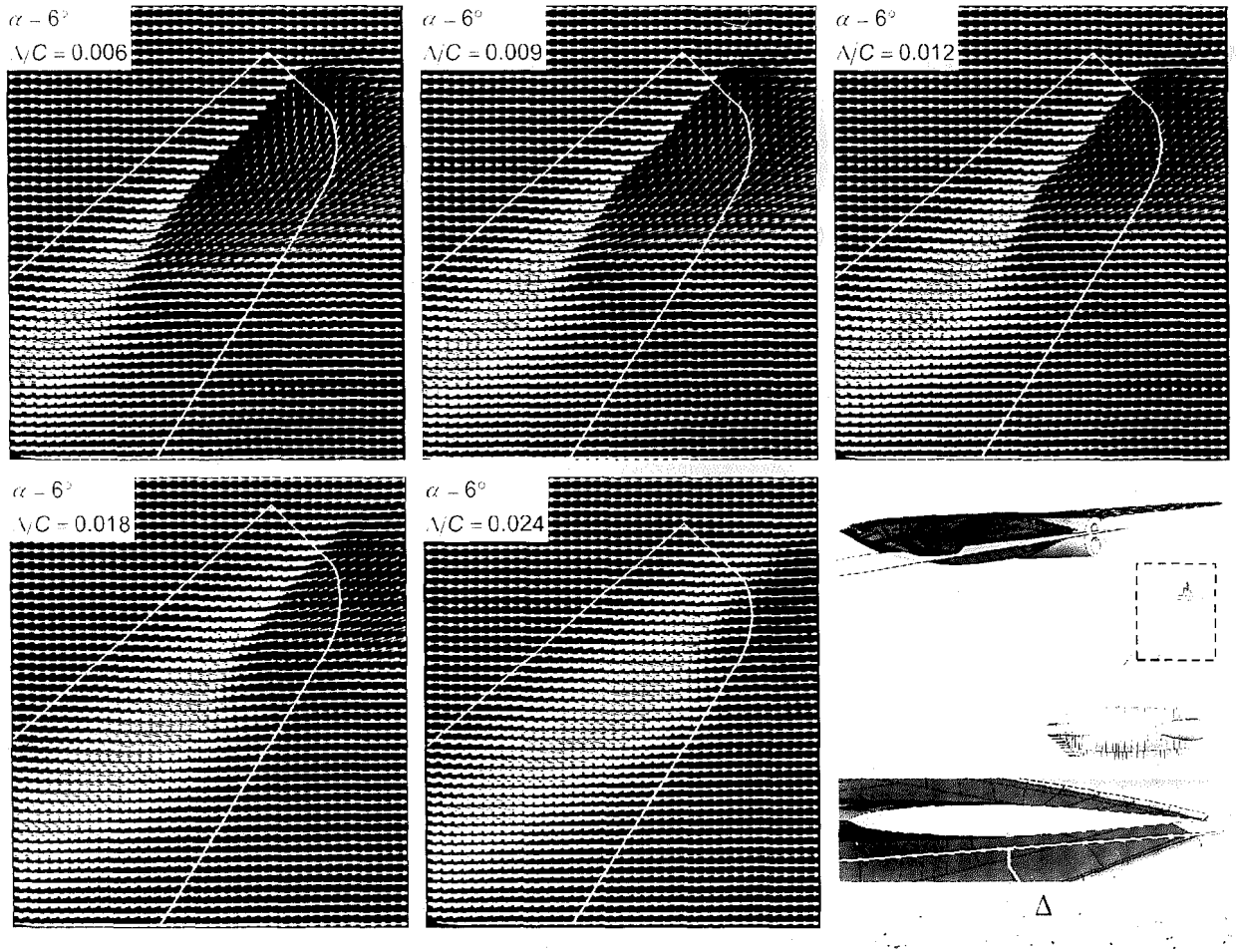

Figure 4.1: Time-averaged velocity vectors $\langle U \rangle$ for different values of displacement Δ/C of laser sheet from surface of wing at angle-of-attack $\alpha = 6°$. Reynolds number Re = 50,000 is based on chord.

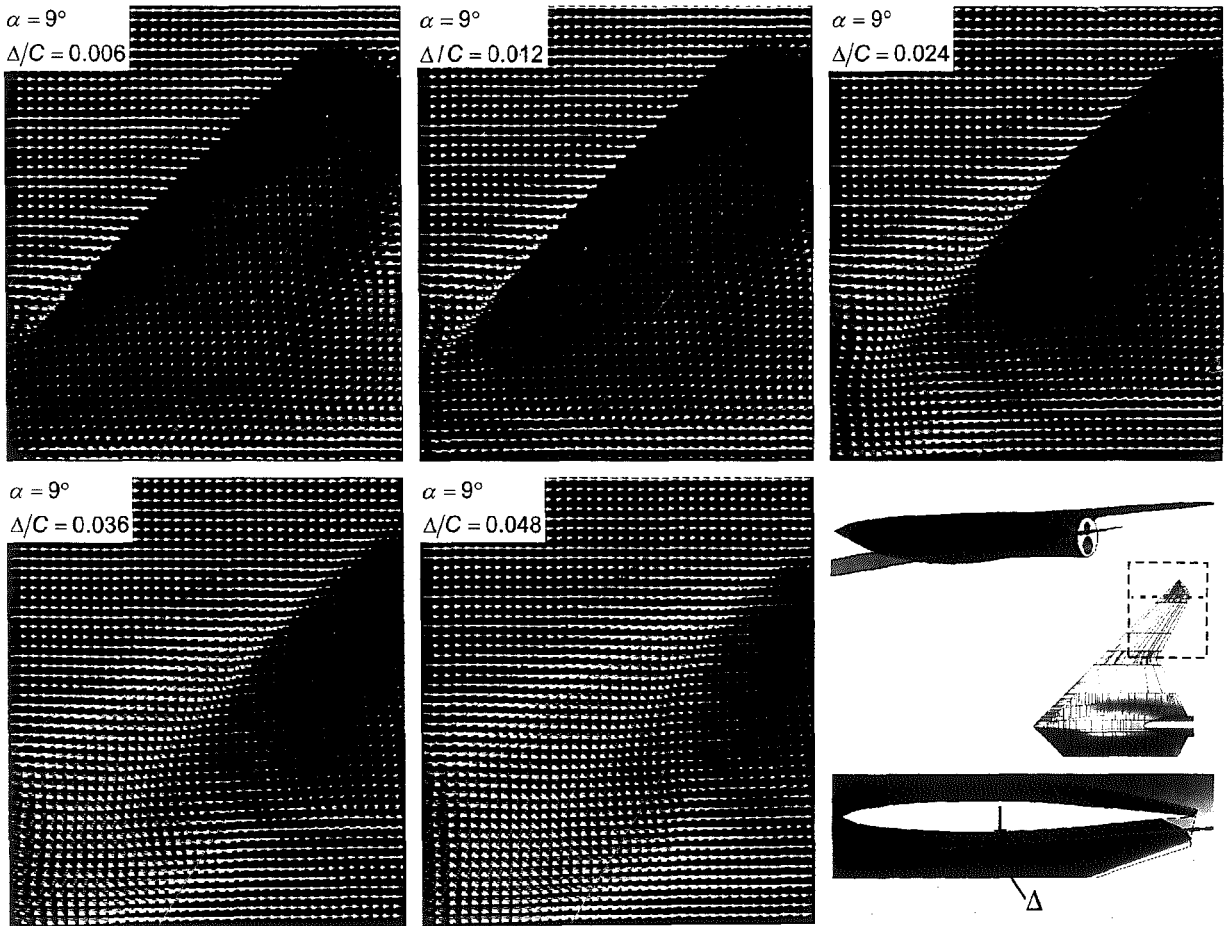

Figure 4.2: Time averaged velocity vectors $\langle \underline{V} \rangle$ for different values of displacement Δ/C of laser sheet from surface of wing at angle-of-attack α = 9°. Reynolds number Re = 50,000 is based on chord.

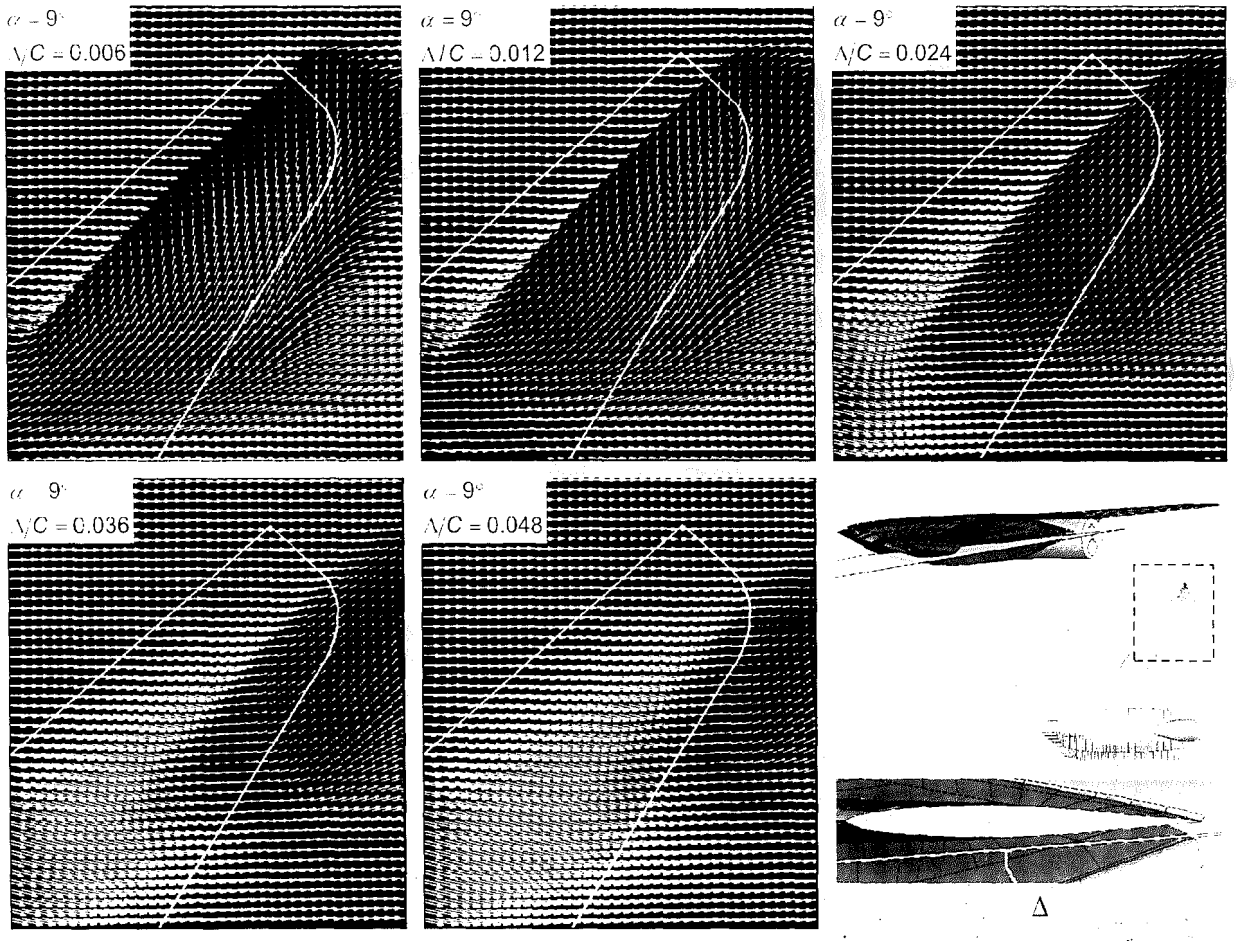

Figure 4.2: Time averaged velocity vectors $\langle U \rangle$ for different values of displacement Δ/C of laser sheet from surface of wing at angle-of-attack $\alpha = 9°$. Reynolds number Re = 50,000 is based on chord.

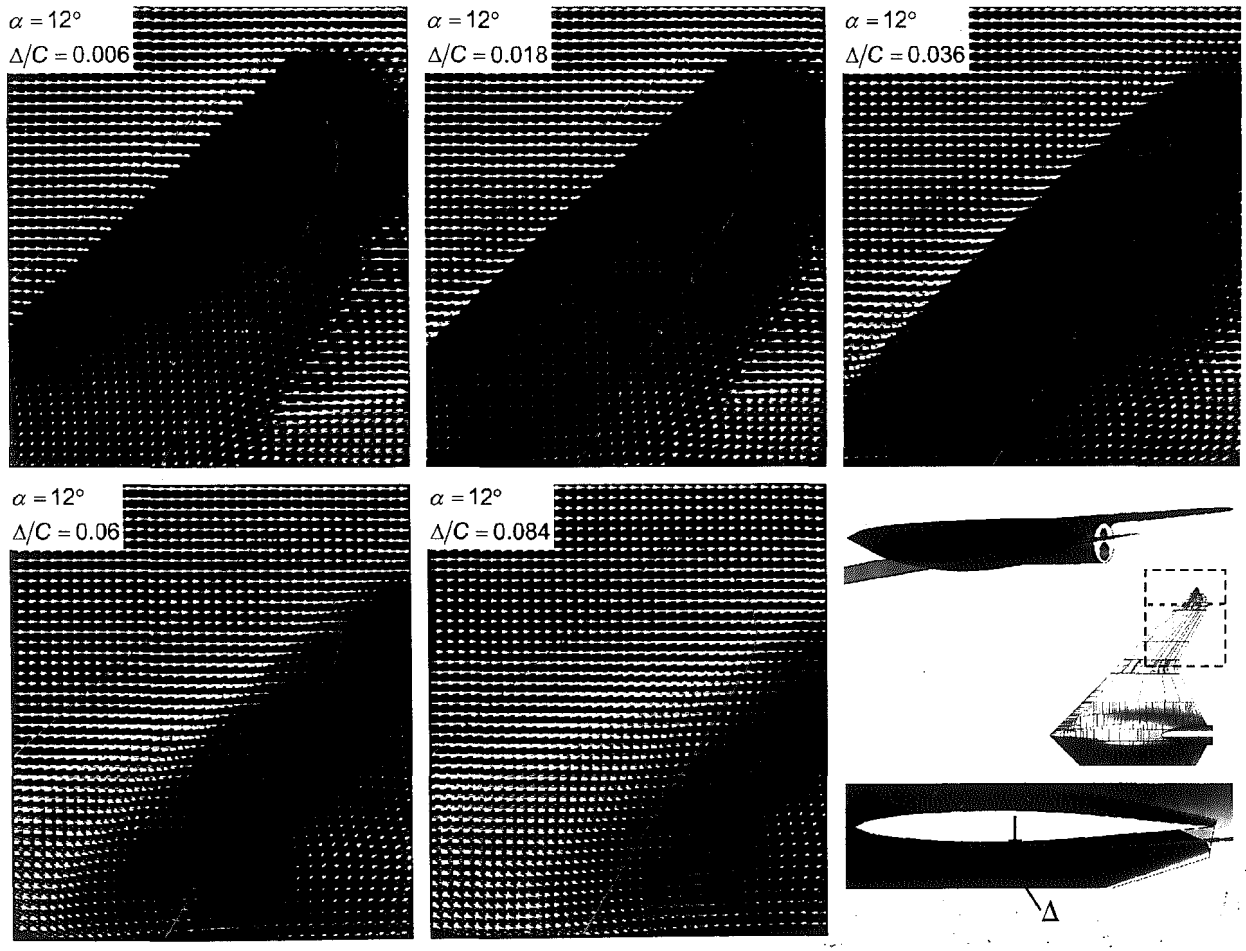

Figure 4.3: Time averaged velocity vectors $\langle V \rangle$ for different values of displacement Δ/C of laser sheet from surface of wing at angle-of-attack α = 12°. Reynolds number Re = 50,000 is based on chord.

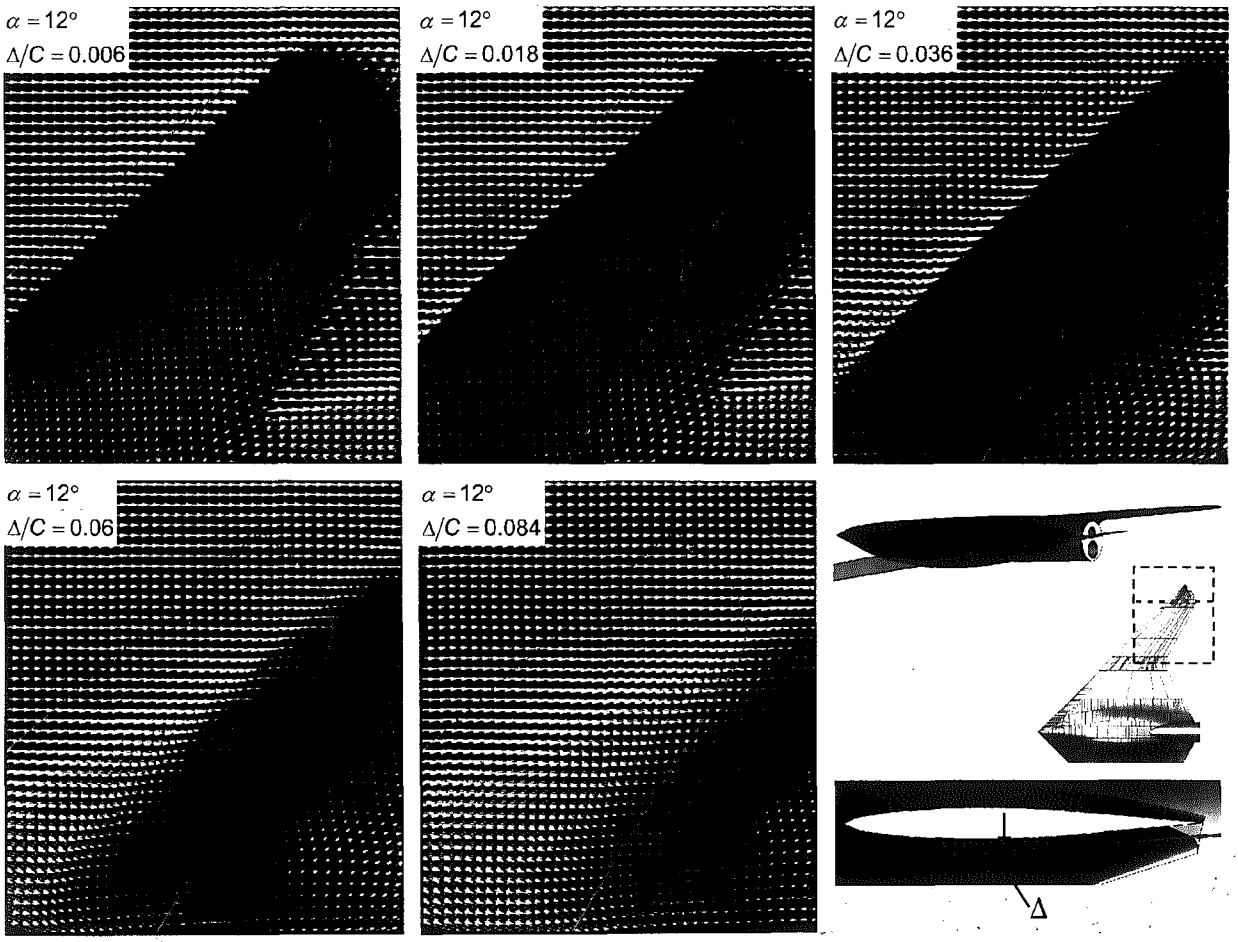

Figure 4.3: Time averaged velocity vectors $\langle \underline{V} \rangle$ for different values of displacement Δ/C of laser sheet from surface of wing at angle-of-attack α = 12°. Reynolds number Re = 50,000 is based on chord.

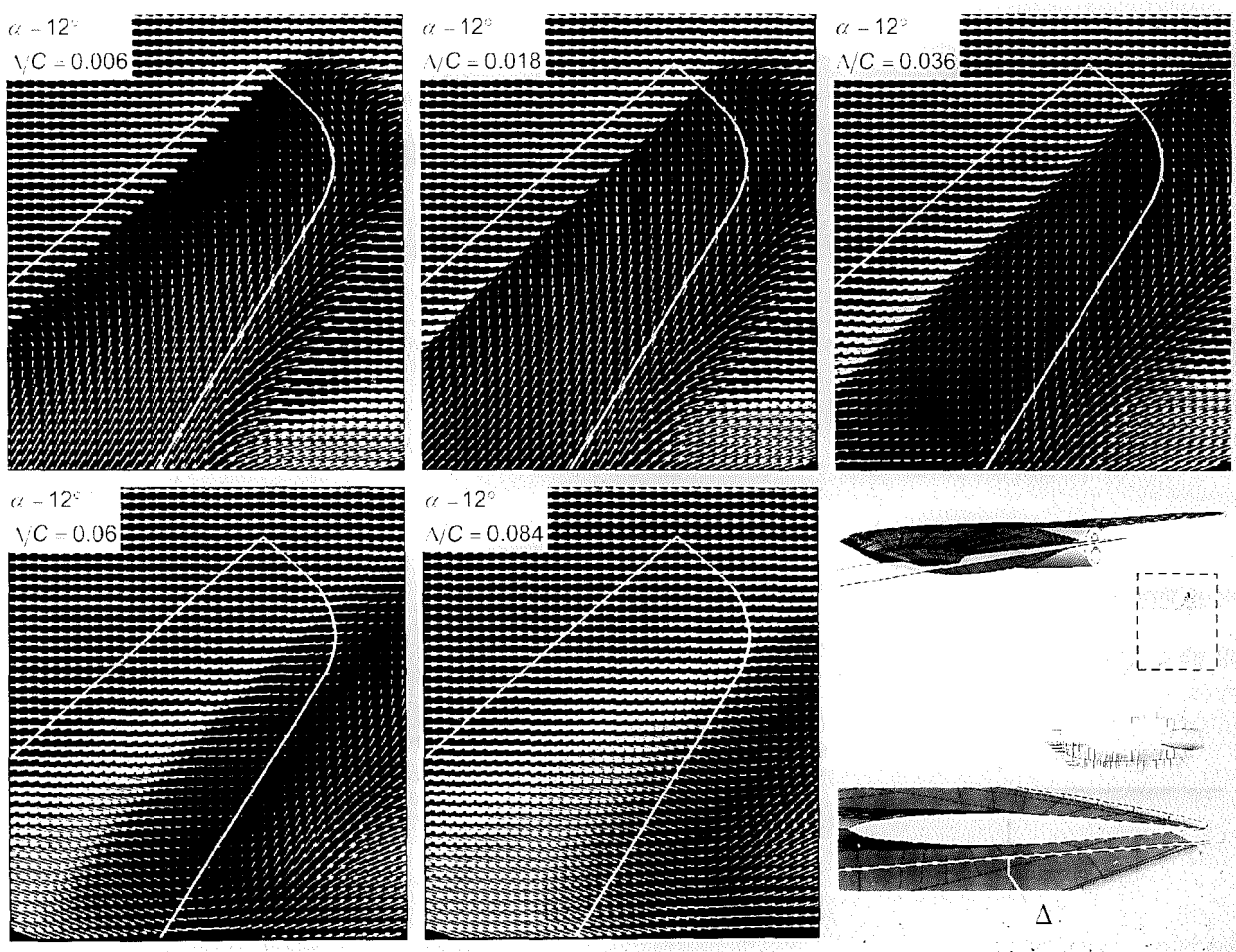

Figure 4.3: Time averaged velocity vectors $\langle U \rangle$ for different values of displacement Δ/C of laser sheet from surface of wing at angle-of-attack $\alpha = 12°$. Reynolds number Re = 50,000 is based on chord.

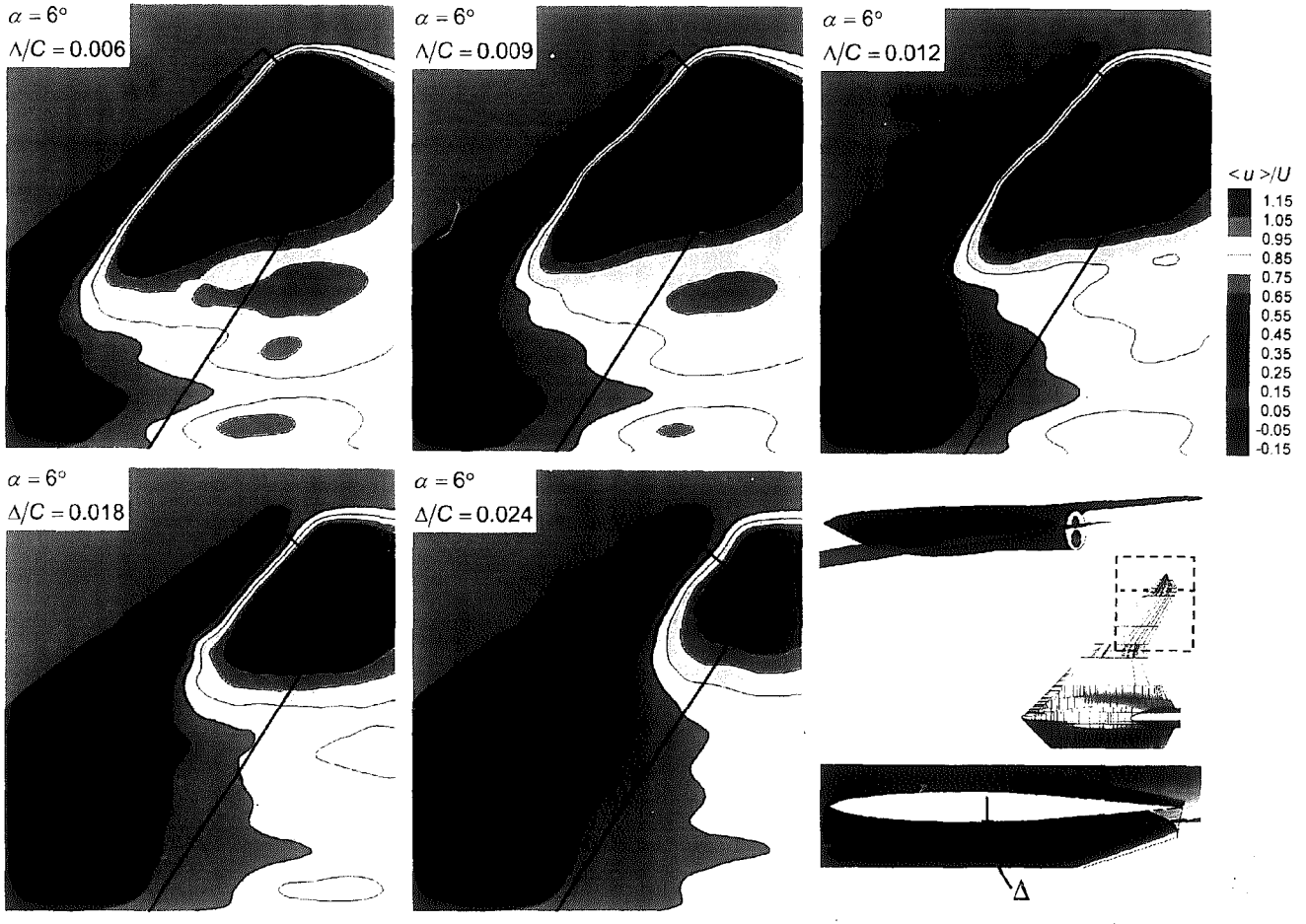

Figure 5.1: Contours of time-averaged streamwise velocity $< u >/U$ for different values of displacement Δ/C of laser sheet from surface of wing at angle-of-attack $\alpha = 6°$. Reynolds number Re = 50,000 is based on chord.

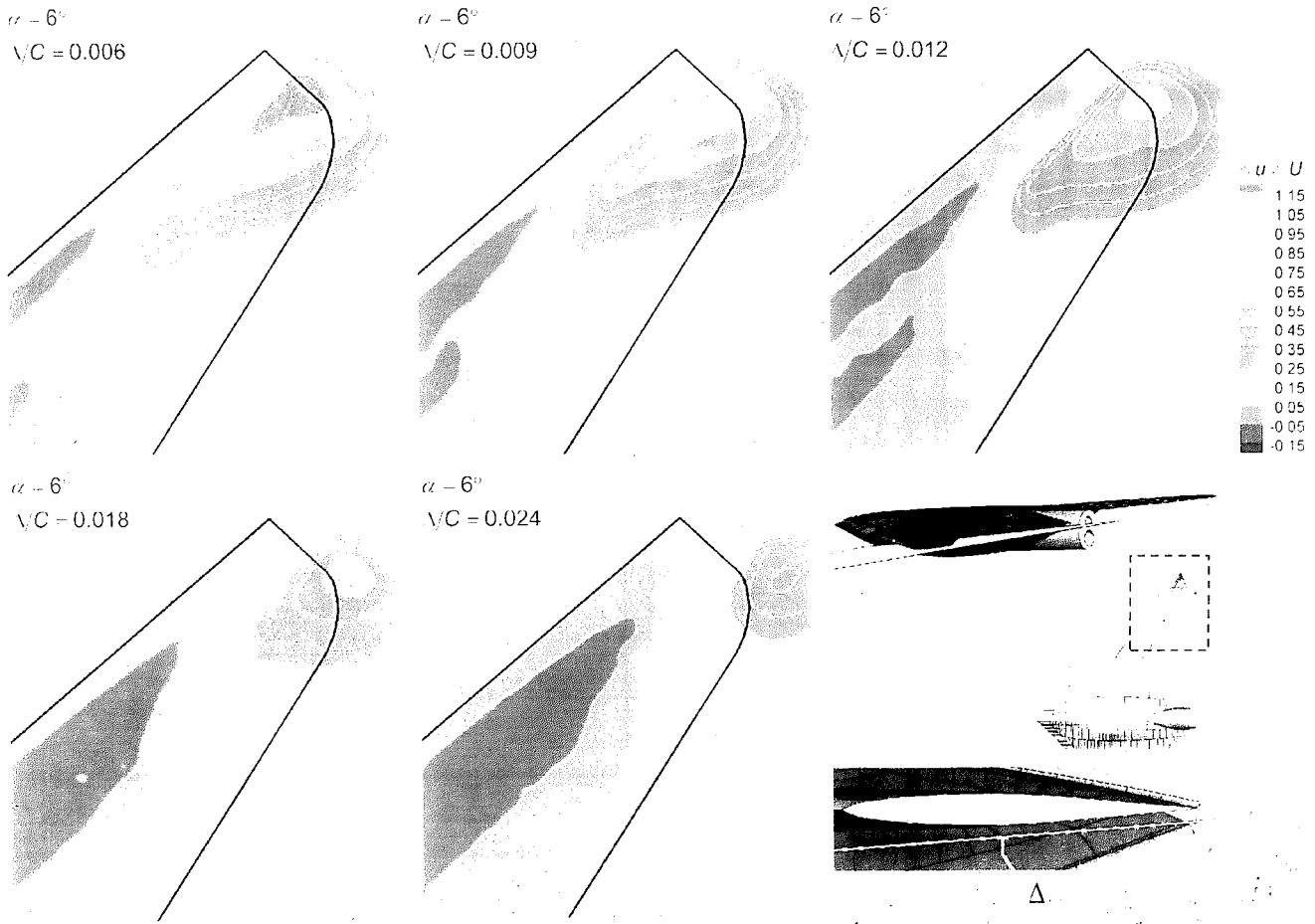

Figure 5.1: Contours of time-averaged streamwise velocity $< u > / U$ for different values of displacement Δ/C of laser sheet from surface of wing at angle-of-attack $\alpha = 6°$. Reynolds number Re = 50,000 is based on chord.

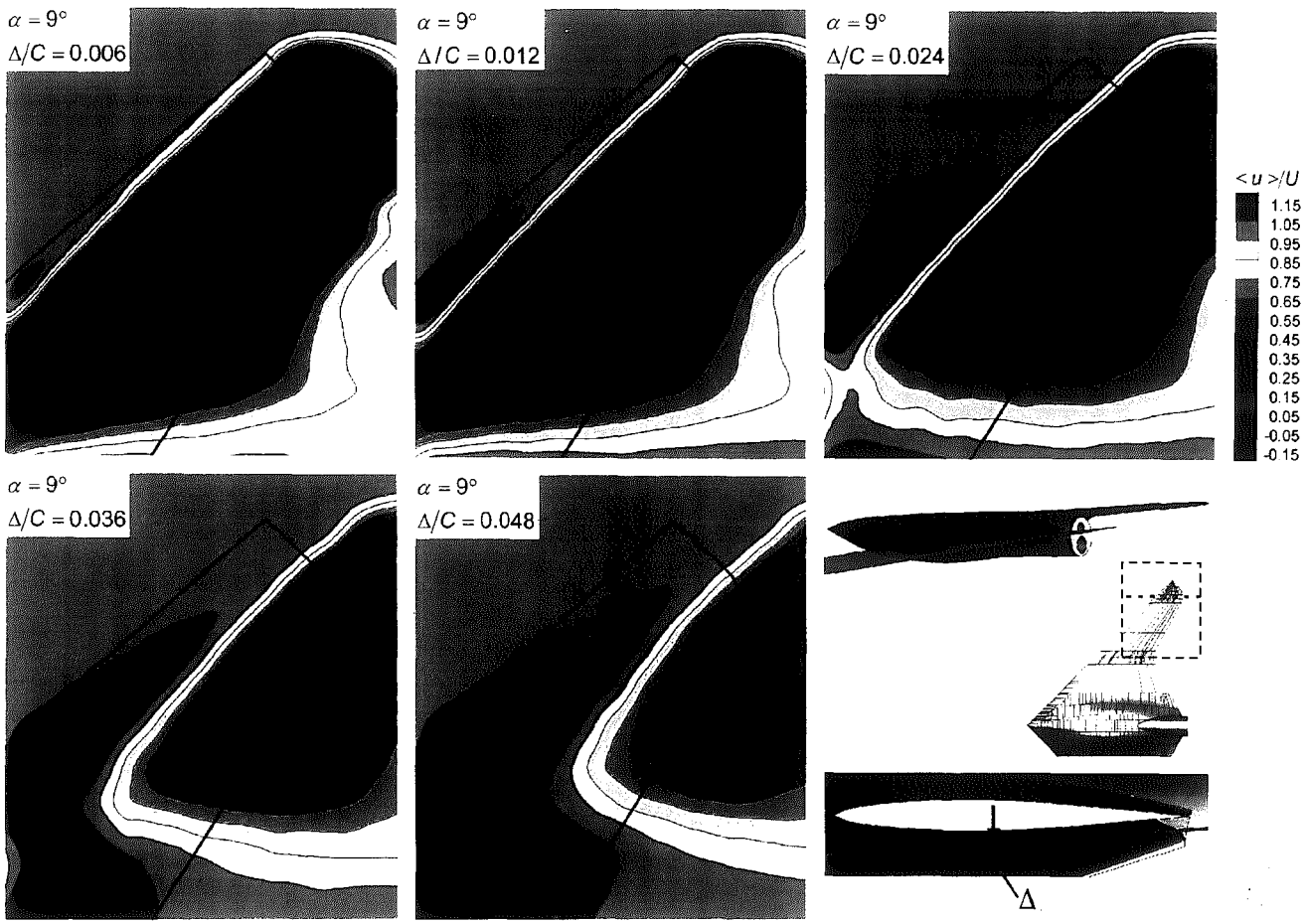

Figure 5.2: Contours of time-averaged streamwise velocity $< u >/U$ for different values of displacement Δ/C of laser sheet from surface of wing at angle-of-attack α = 9°. Reynolds number Re = 50,000 is based on chord.

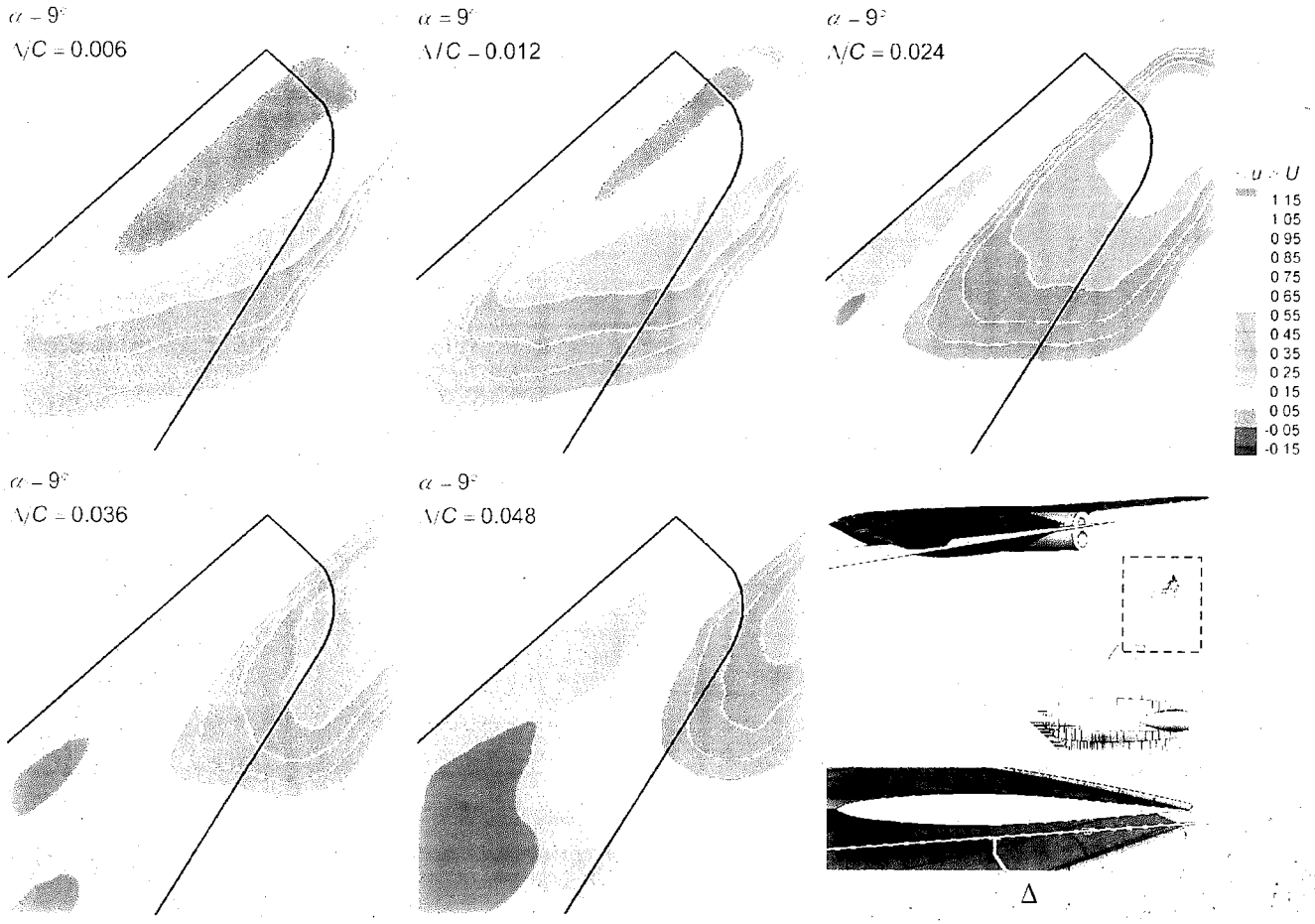

Figure 5.2: Contours of time-averaged streamwise velocity $< u >/U$ for different values of displacement Δ/C of laser sheet from surface of wing at angle-of-attack $\alpha = 9°$. Reynolds number Re = 50,000 is based on chord.

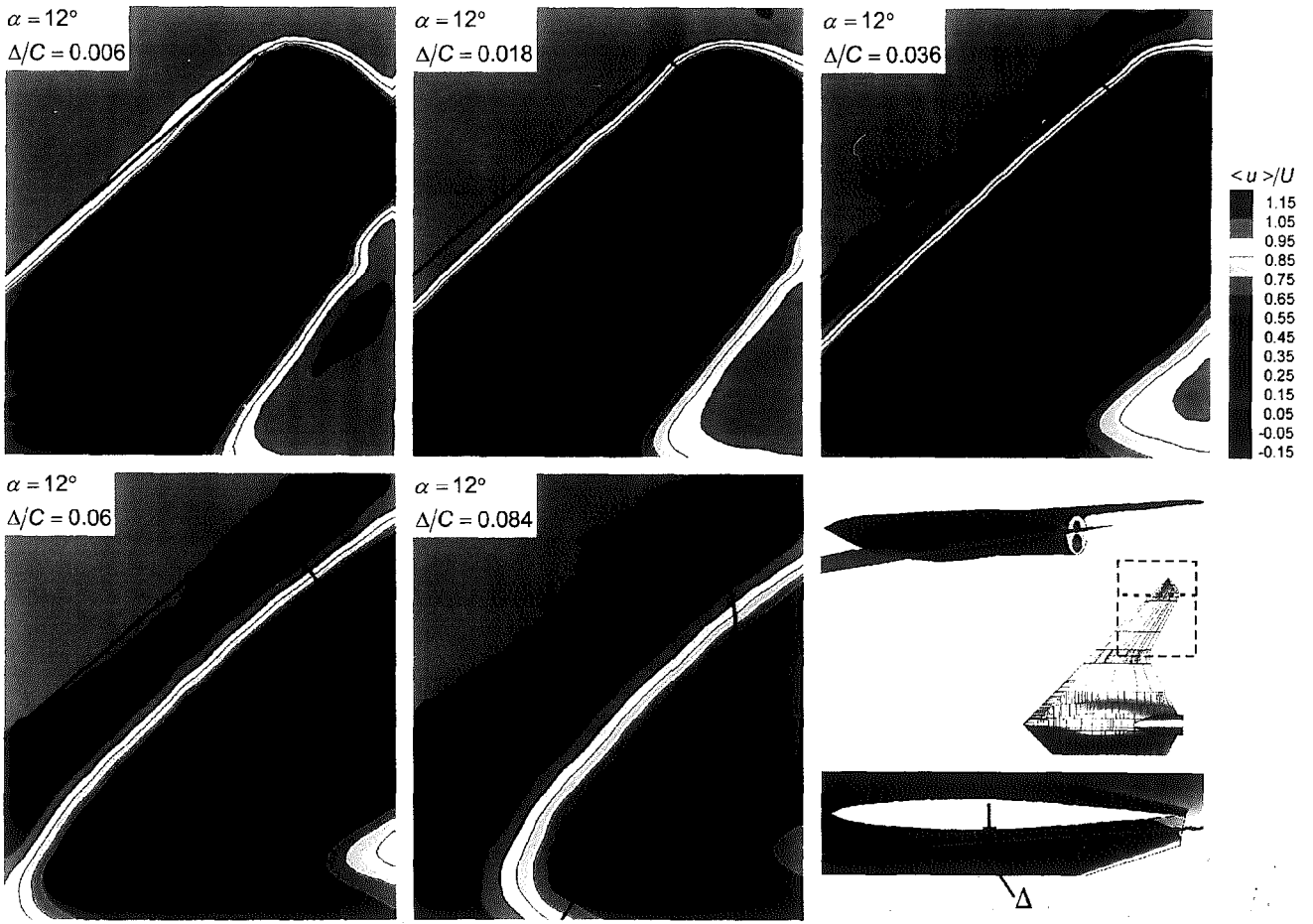

Figure 5.3: Contours of time-averaged streamwise velocity $< u >/U$ for different values of displacement Δ/C of laser sheet from surface of wing at angle-of-attack α = 12°. Reynolds number Re = 50,000 is based on chord.

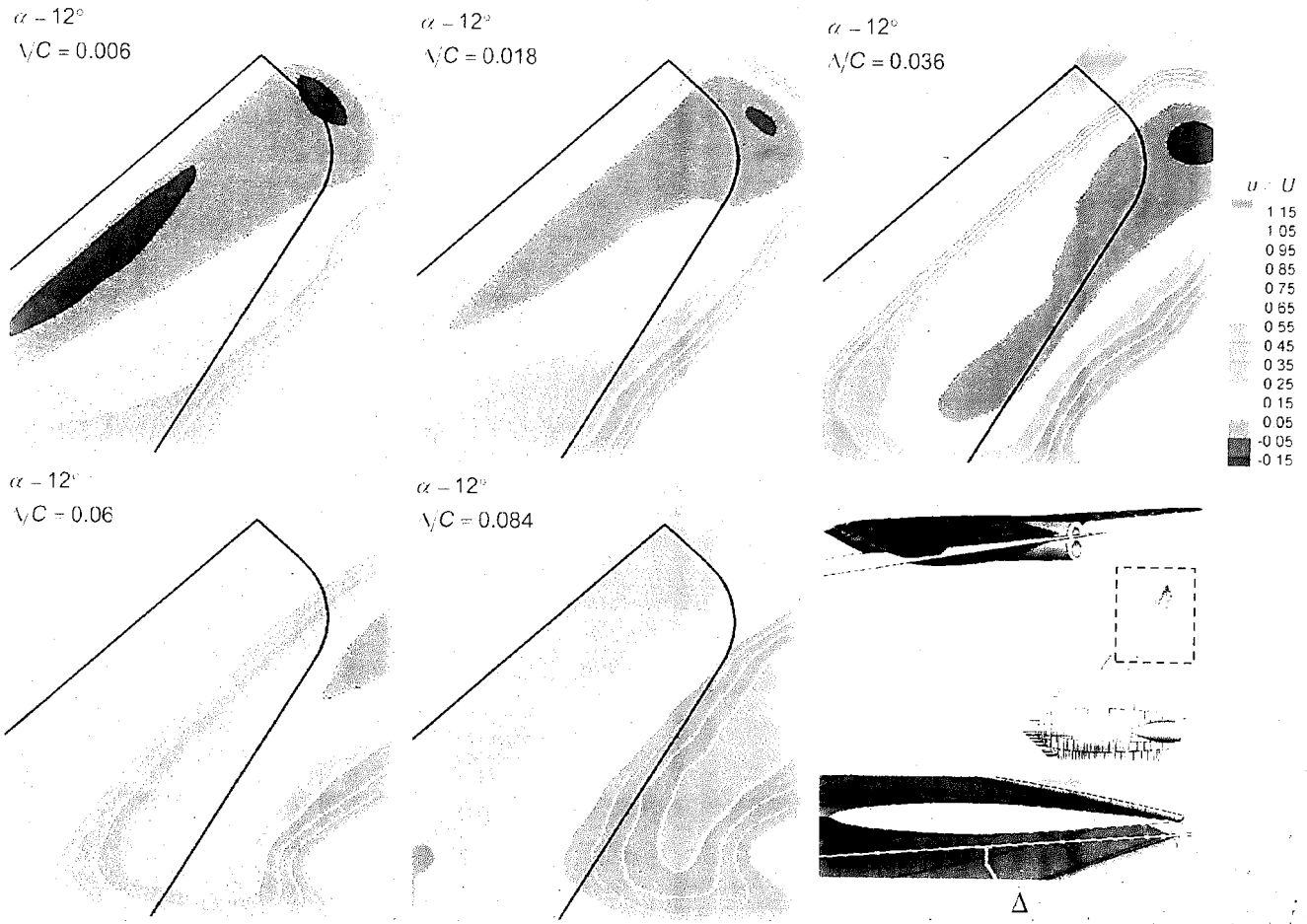

Figure 5.3: Contours of time-averaged streamwise velocity $< u >/U$ for different values of displacement Δ/C of laser sheet from surface of wing at angle-of-attack $\alpha = 12°$. Reynolds number Re = 50,000 is based on chord.

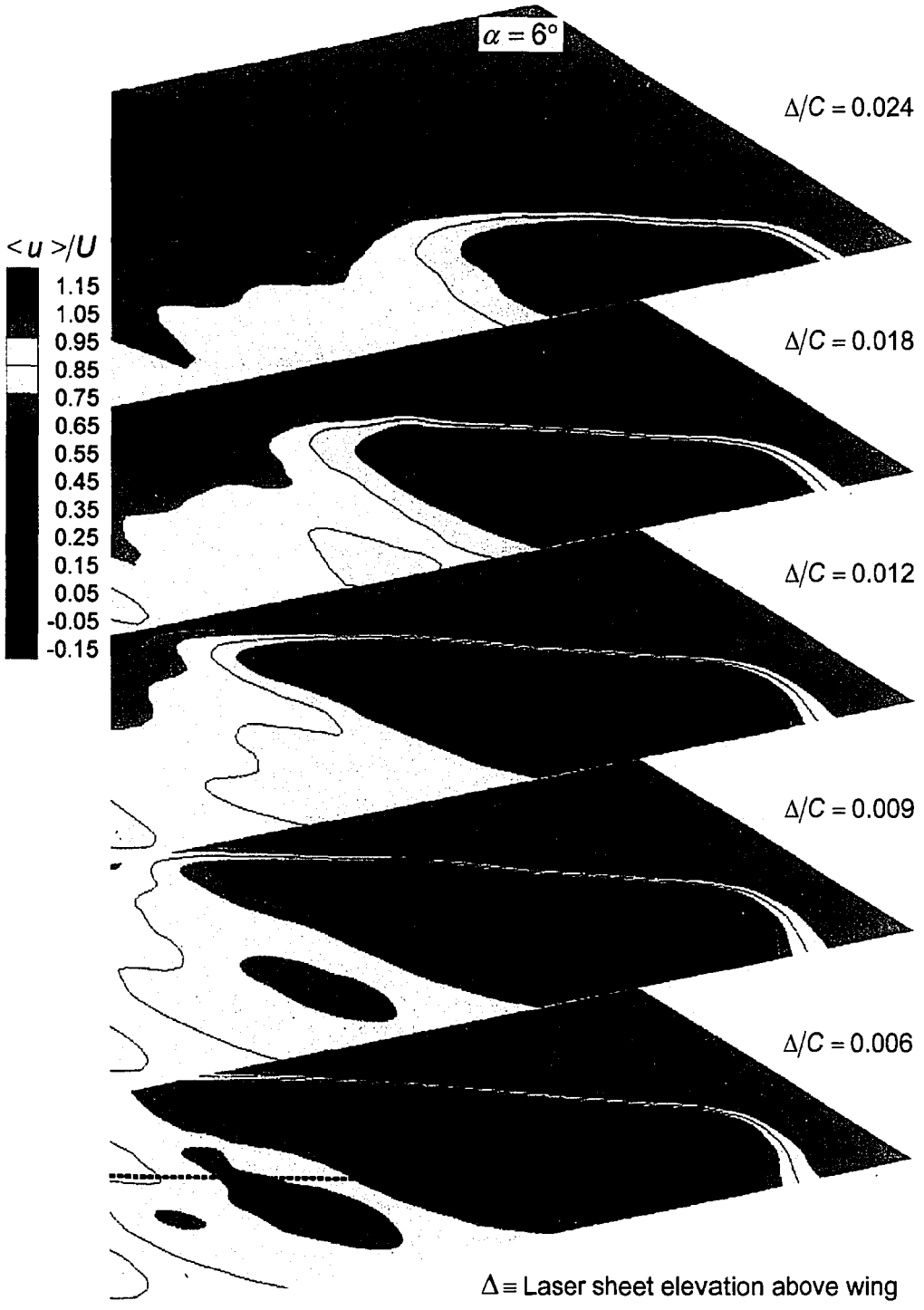

Figure 6.1: Stacked arrangement of contours of time-averaged streamwise velocity $< u >/U$ for different values of displacement Δ/C of laser sheet from surface of wing at angle-of-attack $\alpha = 6°$. Reynolds number Re = 50,000 is based on chord.

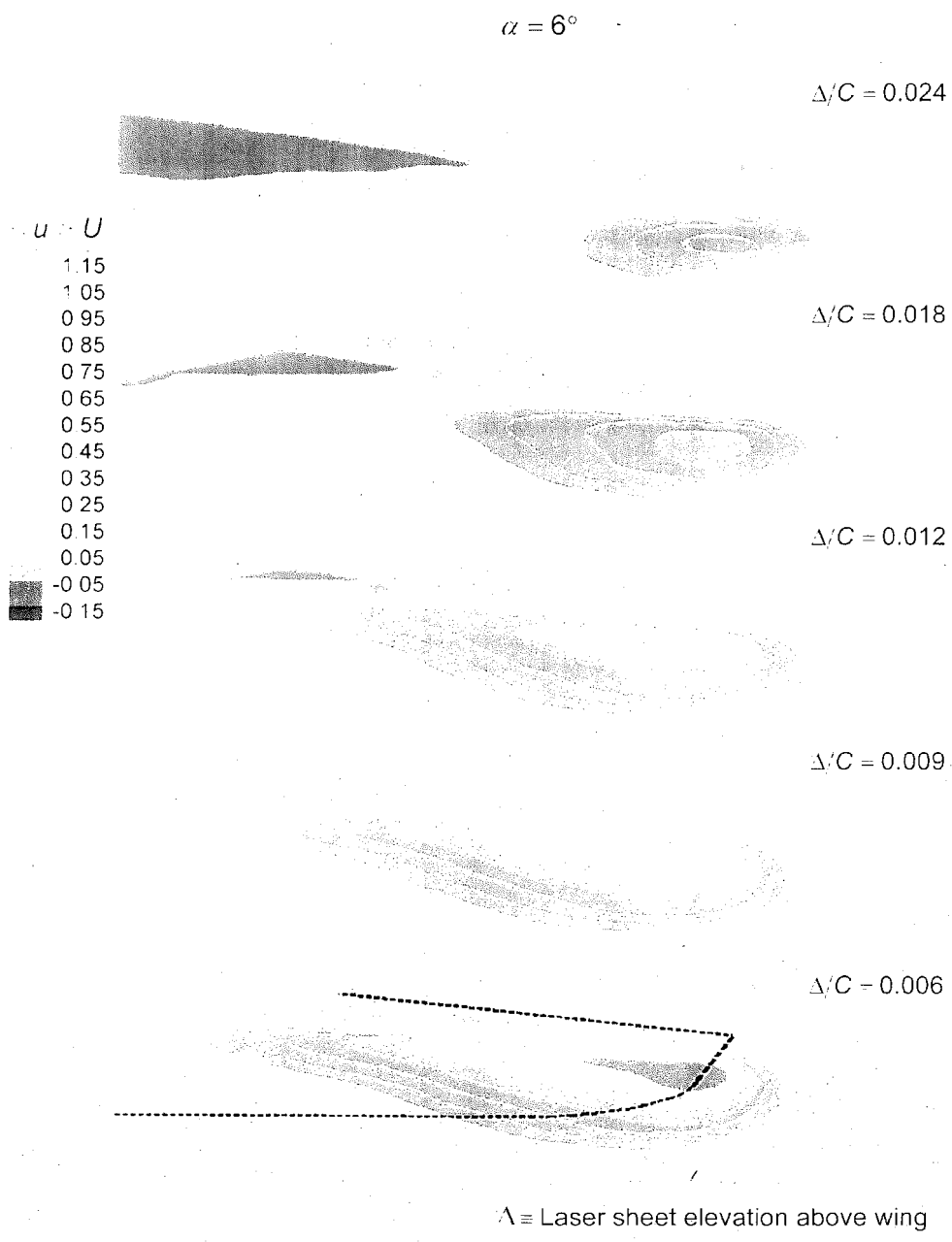

Figure 6.1: Stacked arrangement of contours of time-averaged streamwise velocity $< u >/U$ for different values of displacement Δ/C of laser sheet from surface of wing at angle-of-attack $\alpha = 6°$. Reynolds number Re = 50,000 is based on chord.

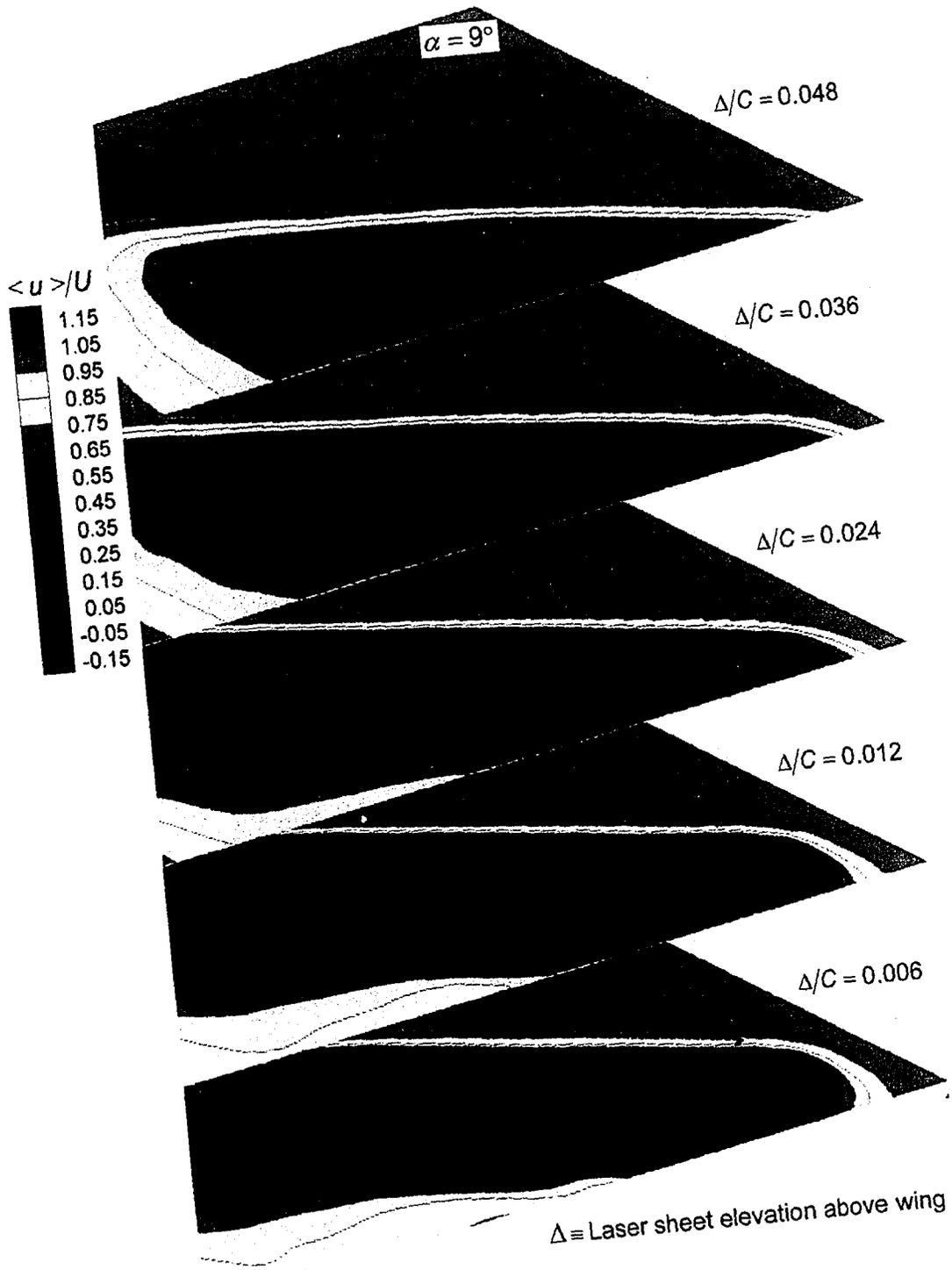

Figure 6.2: Stacked arrangement of contours of time-averaged streamwise velocity $< u >/U$ for different values of displacement Δ/C of laser sheet from surface of wing at angle-of-attack $\alpha = 9°$. Reynolds number Re = 50,000 is based on chord.

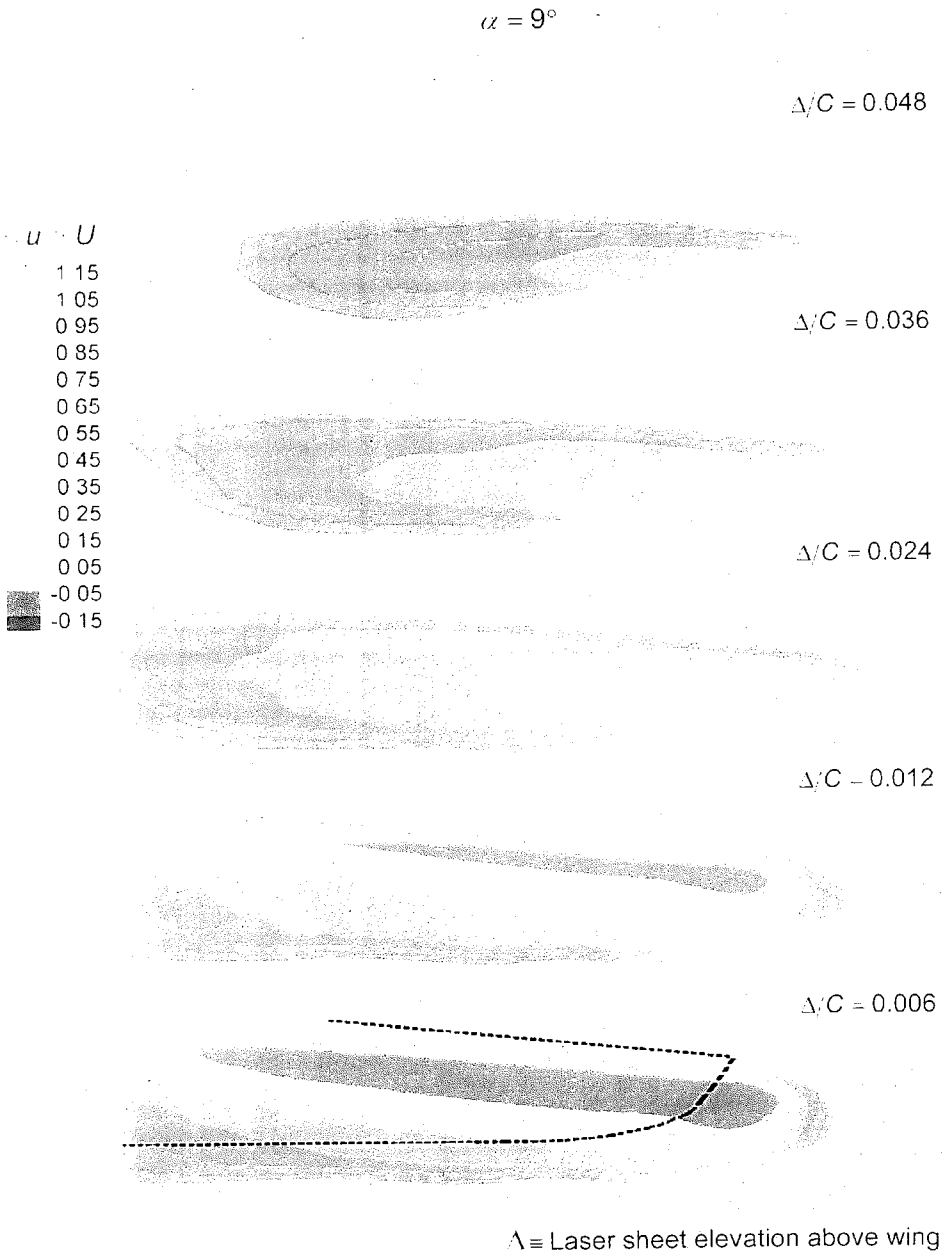

Figure 6.2: Stacked arrangement of contours of time-averaged streamwise velocity $\langle u \rangle / U$ for different values of displacement Δ/C of laser sheet from surface of wing at angle-of-attack $\alpha = 9°$. Reynolds number Re = 50,000 is based on chord.

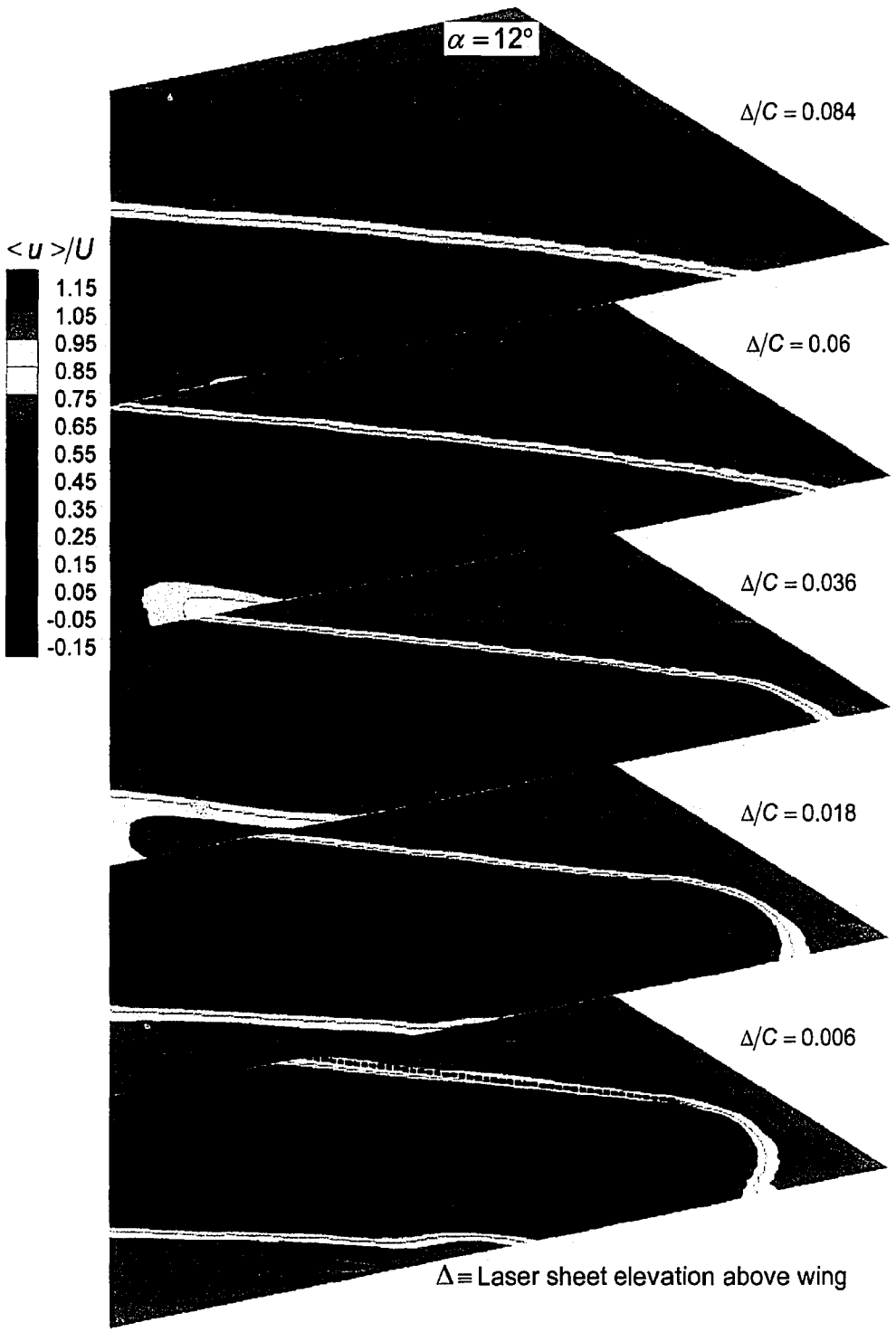

Figure 6.3: Stacked arrangement of contours of time-averaged streamwise velocity $< u >/U$ for different values of displacement Δ/C of laser sheet from surface of wing at angle-of-attack α = 12°. Reynolds number Re = 50,000 is based on chord.

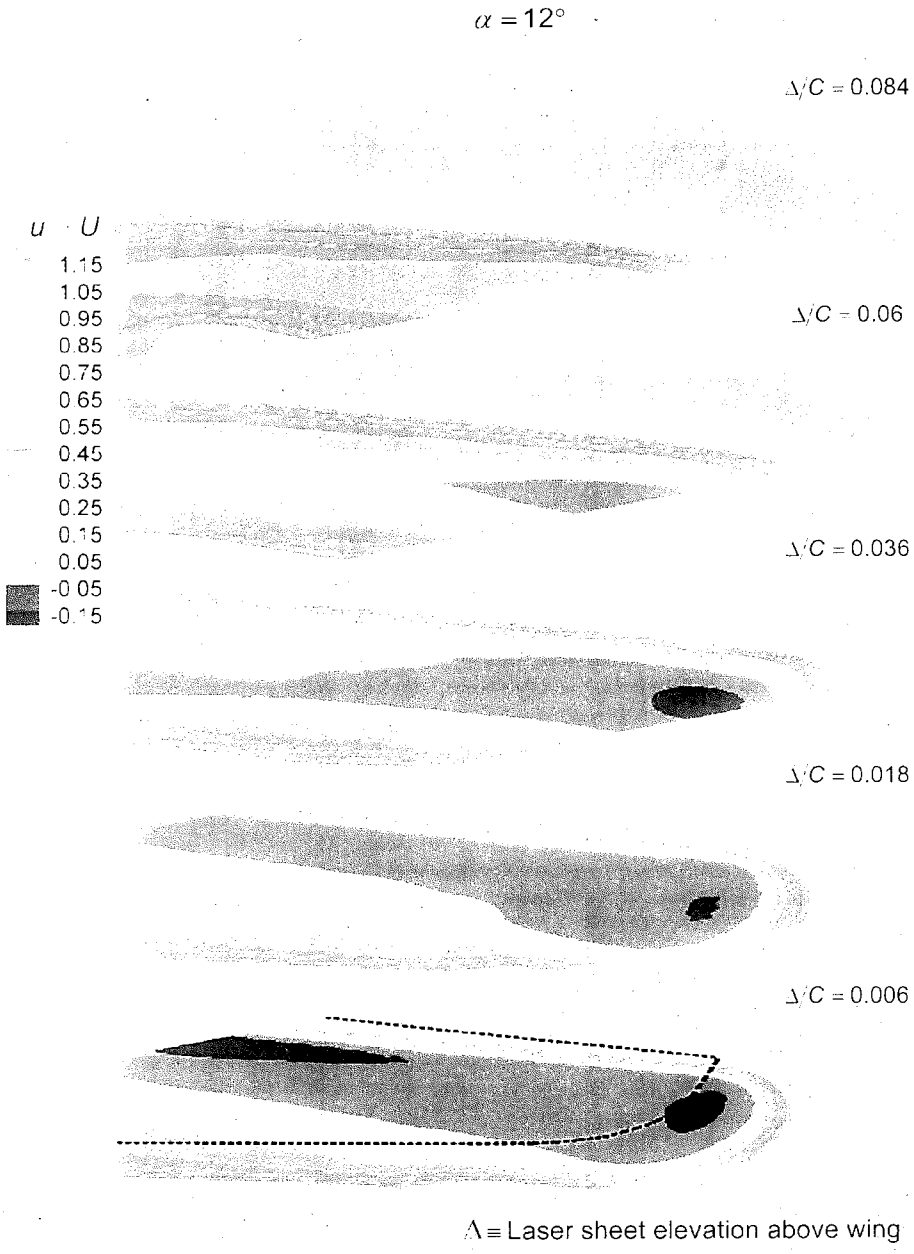

Figure 6.3: Stacked arrangement of contours of time-averaged streamwise velocity $< u >/U_\infty$ for different values of displacement Δ/C of laser sheet from surface of wing at angle-of-attack $\alpha = 12°$. Reynolds number Re = 50,000 is based on chord.

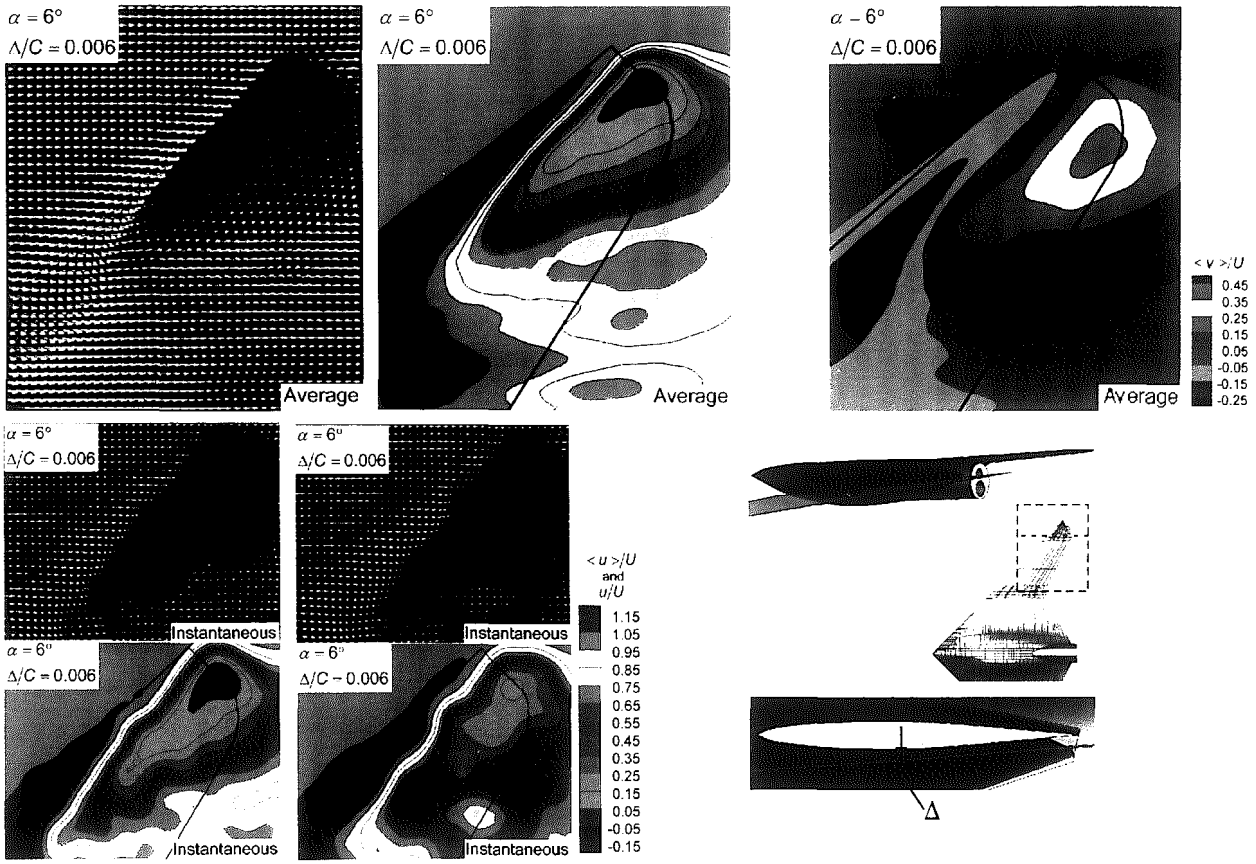

Figure 7.1: Averaged patterns of velocity vectors $< \underline{V} >$, streamwise velocity $< u >/U$ and traverse velocity $< v >/U$ in comparison with patterns of instantaneous velocity vectors $\underline{V}$, and streamwise velocity u/U. Laser sheet displacement from the surface of the wing is $\Delta/C = 0.006$. Angle- of-attack is $\alpha = 6°$.

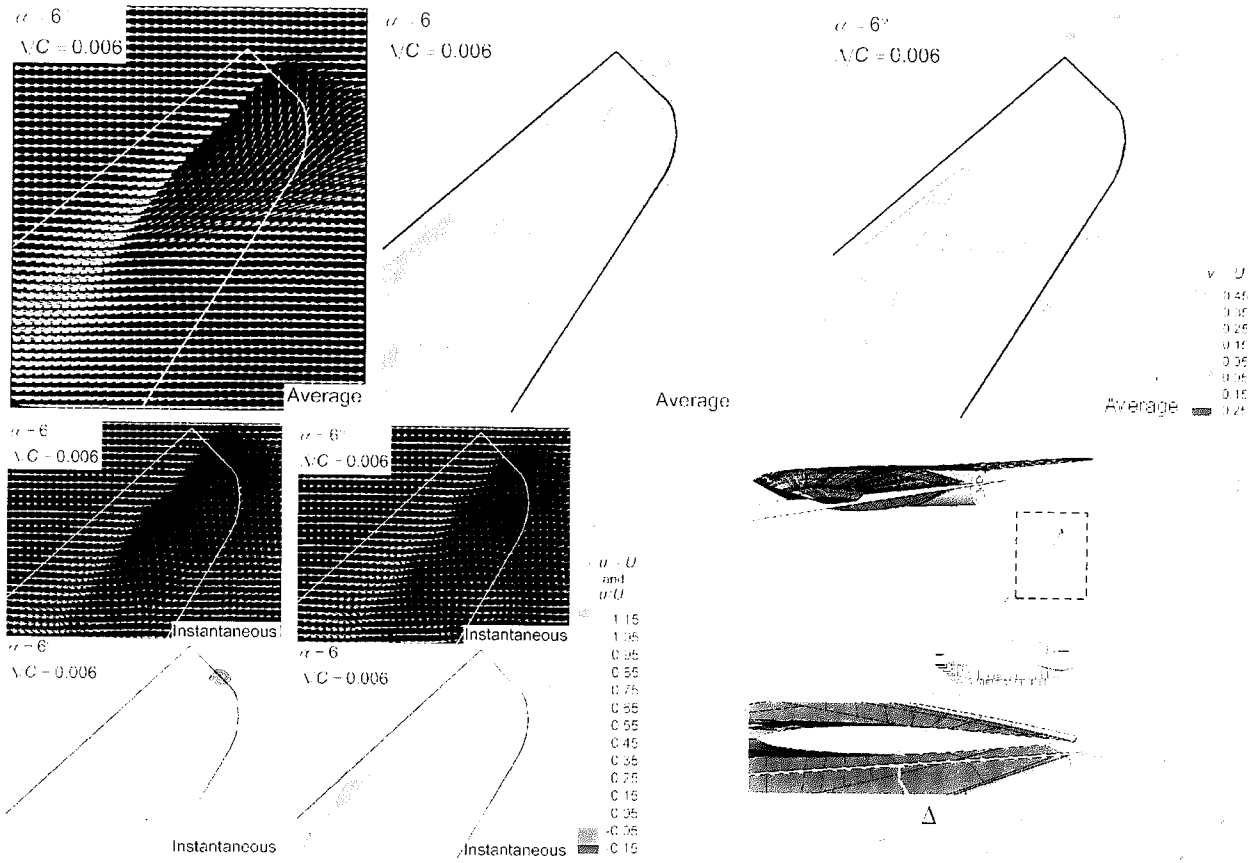

Figure 7.1: Averaged patterns of velocity vectors $\langle \underline{U} \rangle$, streamwise velocity $\langle u \rangle / U$ and traverse velocity $\langle v \rangle / U$ in comparison with patterns of instantaneous velocity vectors $\underline{U}$, and streamwise velocity u/U. Laser sheet displacement from the surface of the wing is $Y/C = 0.006$. Angle-of-attack is $\alpha = 6°$.

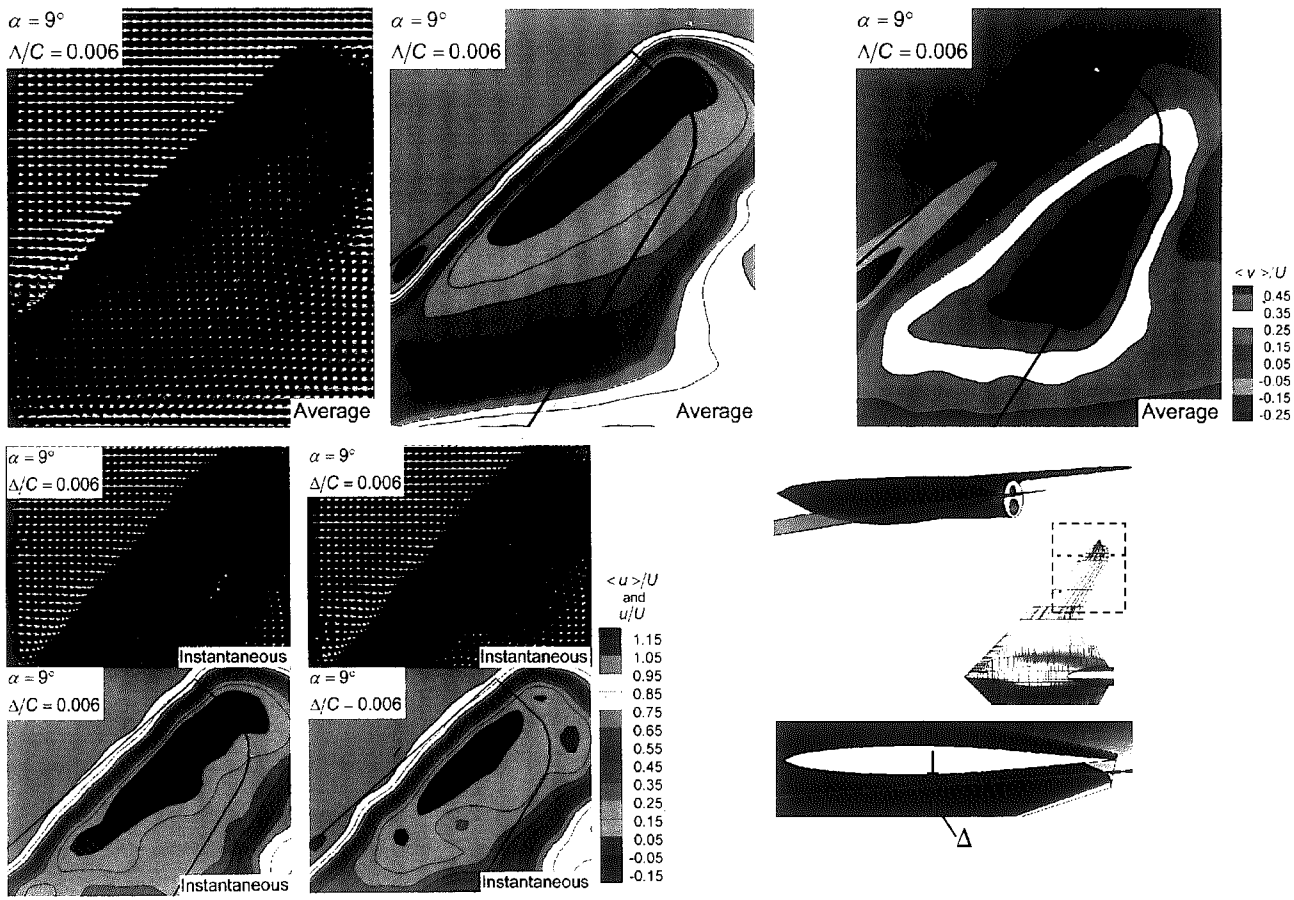

Figure 7.2: Averaged patterns of velocity vectors $<\underline{V}>$, streamwise velocity $<u>/U$ and traverse velocity $<v>/U$ in comparison with patterns of instantaneous velocity vectors $\underline{V}$, and streamwise velocity u/U. Laser sheet displacement from the surface of the wing is $\Delta/C = 0.006$. Angle-of-attack is $\alpha = 9°$.

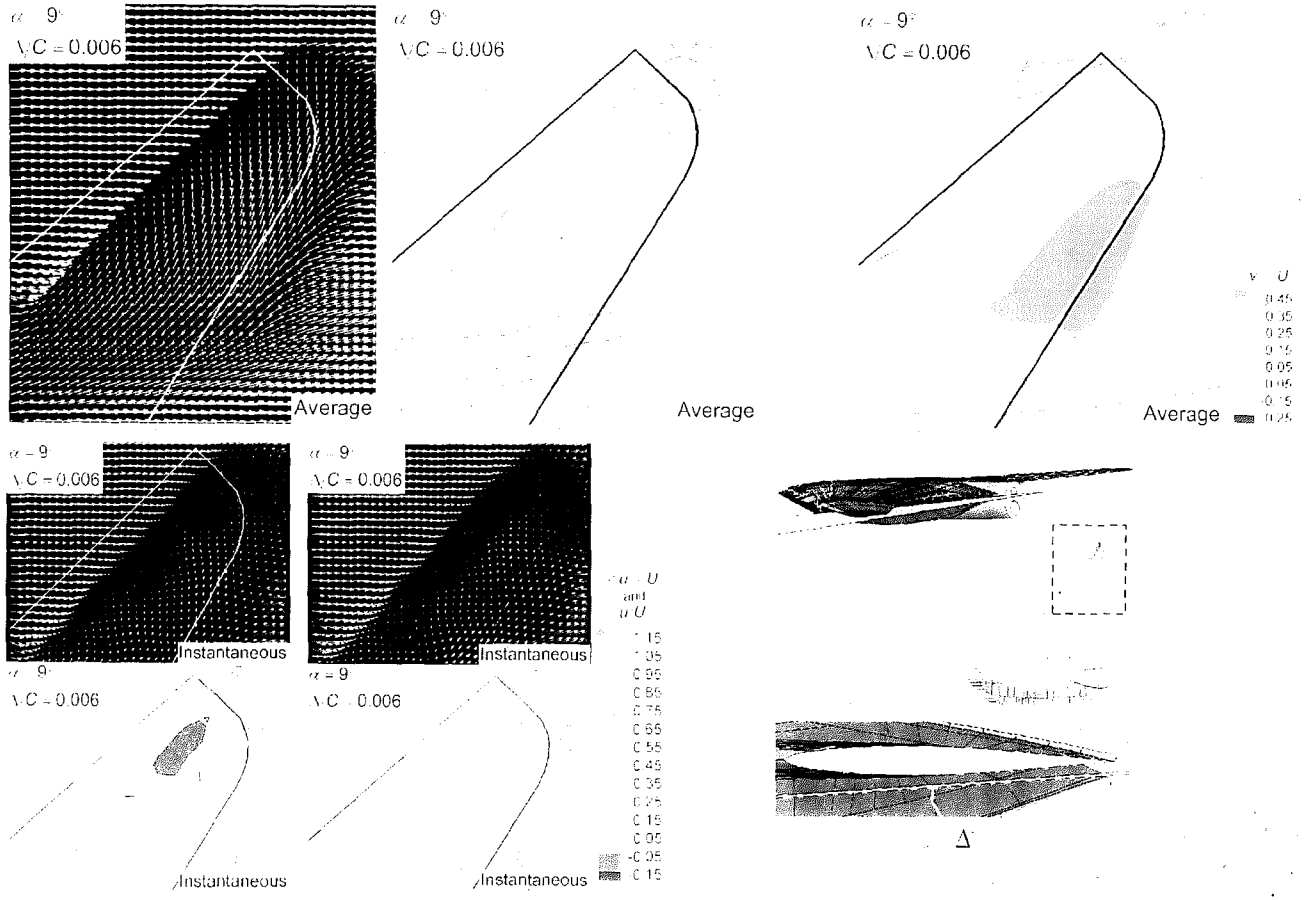

Figure 7.2: Averaged patterns of velocity vectors $\langle \underline{U} \rangle / U_\infty$, streamwise velocity $\langle u \rangle / U_\infty$ and traverse velocity $\langle v \rangle / U_\infty$ in comparison with patterns of instantaneous velocity vectors $\underline{U}$ and streamwise velocity u/U_∞. Laser sheet displacement from the surface of the wing is $Y/C = 0.006$. Angle-of-attack is $\alpha = 9°$.

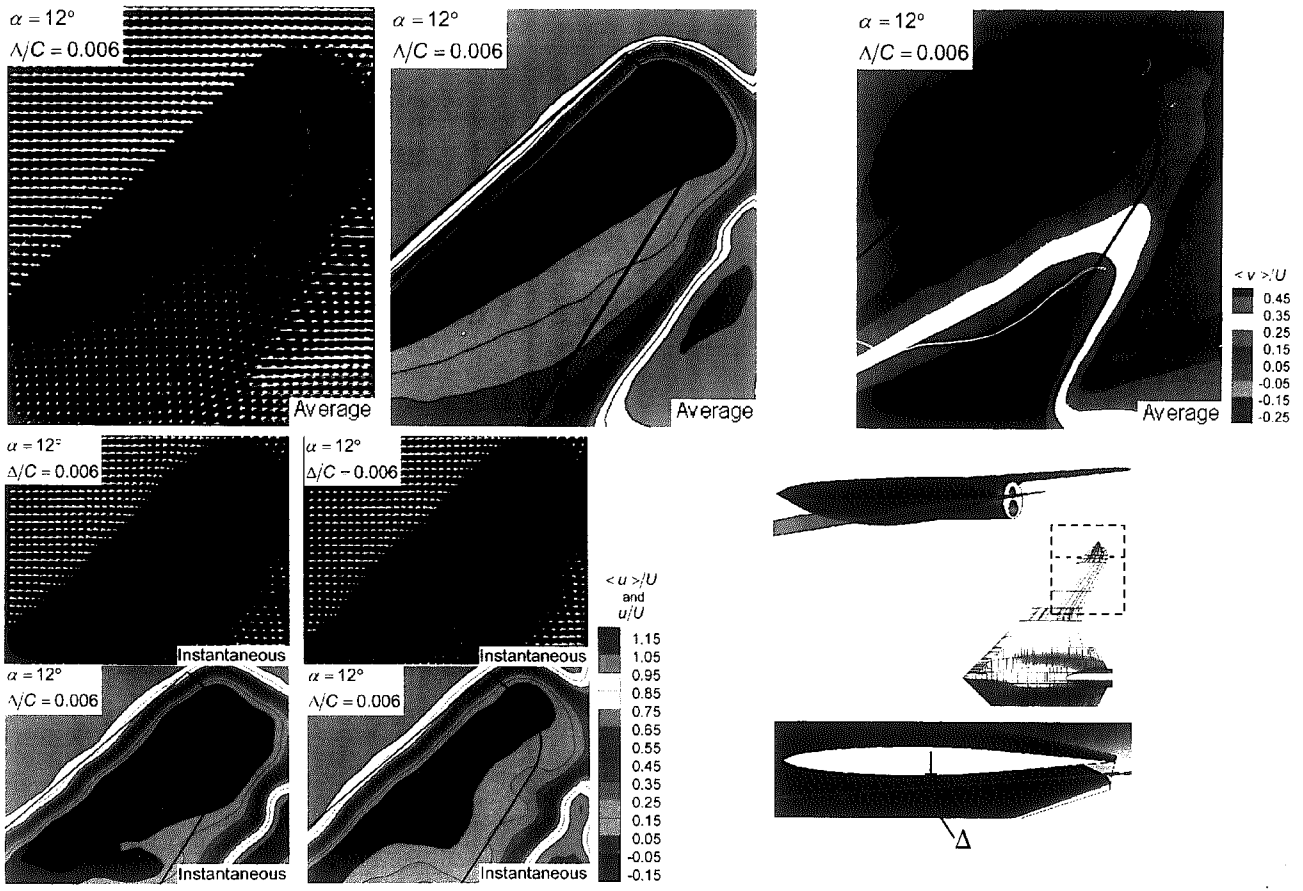

Figure 7.3: Averaged patterns of velocity vectors $<\underline{V}>$, streamwise velocity $<u>/U$ and traverse velocity $<v>/U$ in comparison with patterns of instantaneous velocity vectors $\underline{V}$, and streamwise velocity u/U. Laser sheet displacement from the surface of the wing is $\Delta/C = 0.006$. Angle-of-attack is $\alpha = 12°$.

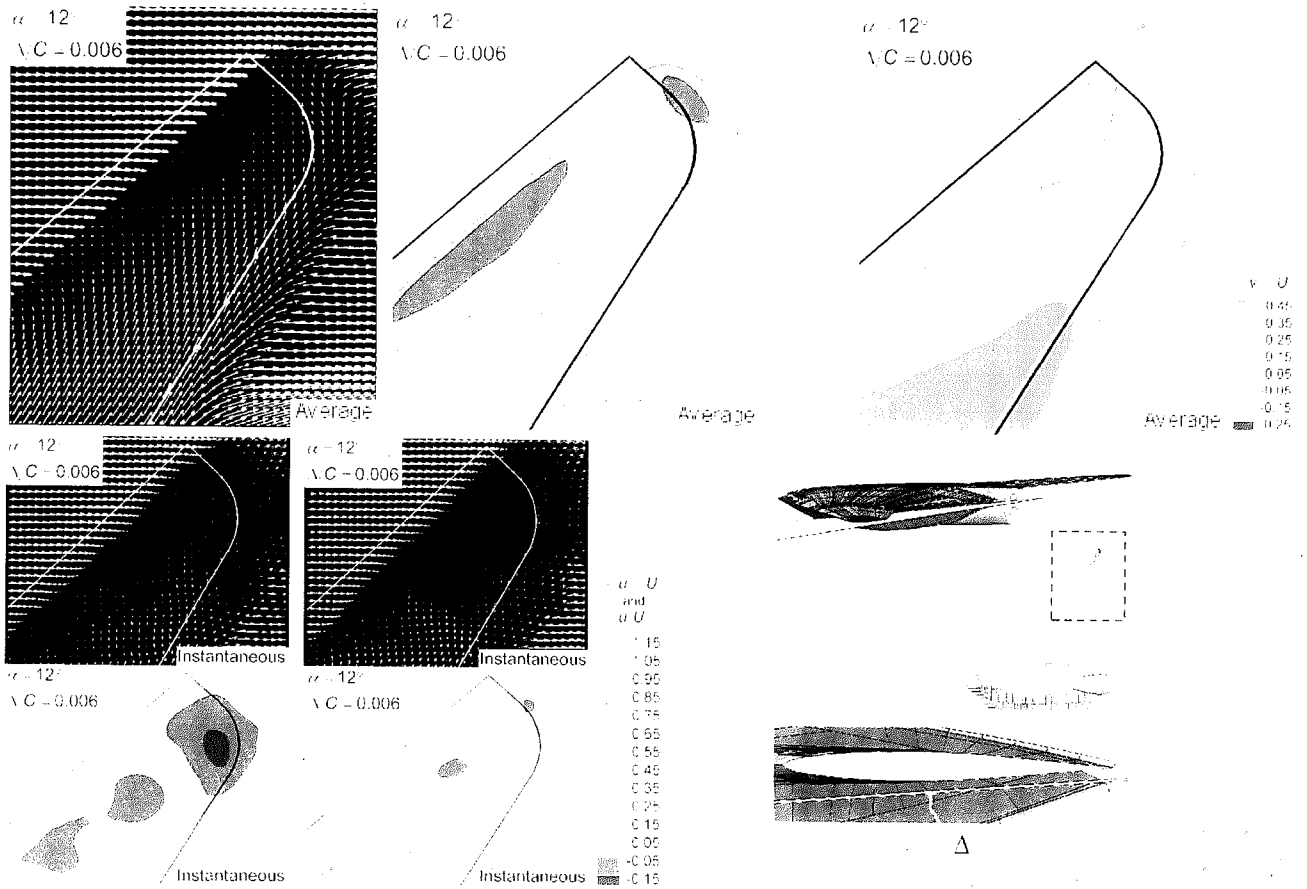

Figure 7.3: Averaged patterns of velocity vectors $\underline{V}/U$, streamwise velocity u/U and traverse velocity v/U in comparison with patterns of instantaneous velocity vectors $\underline{V}/U$ and streamwise velocity u/U. Laser sheet displacement from the surface of the wing is $\Delta/C = 0.006$. Angle-of-attack is $\alpha = 12°$.

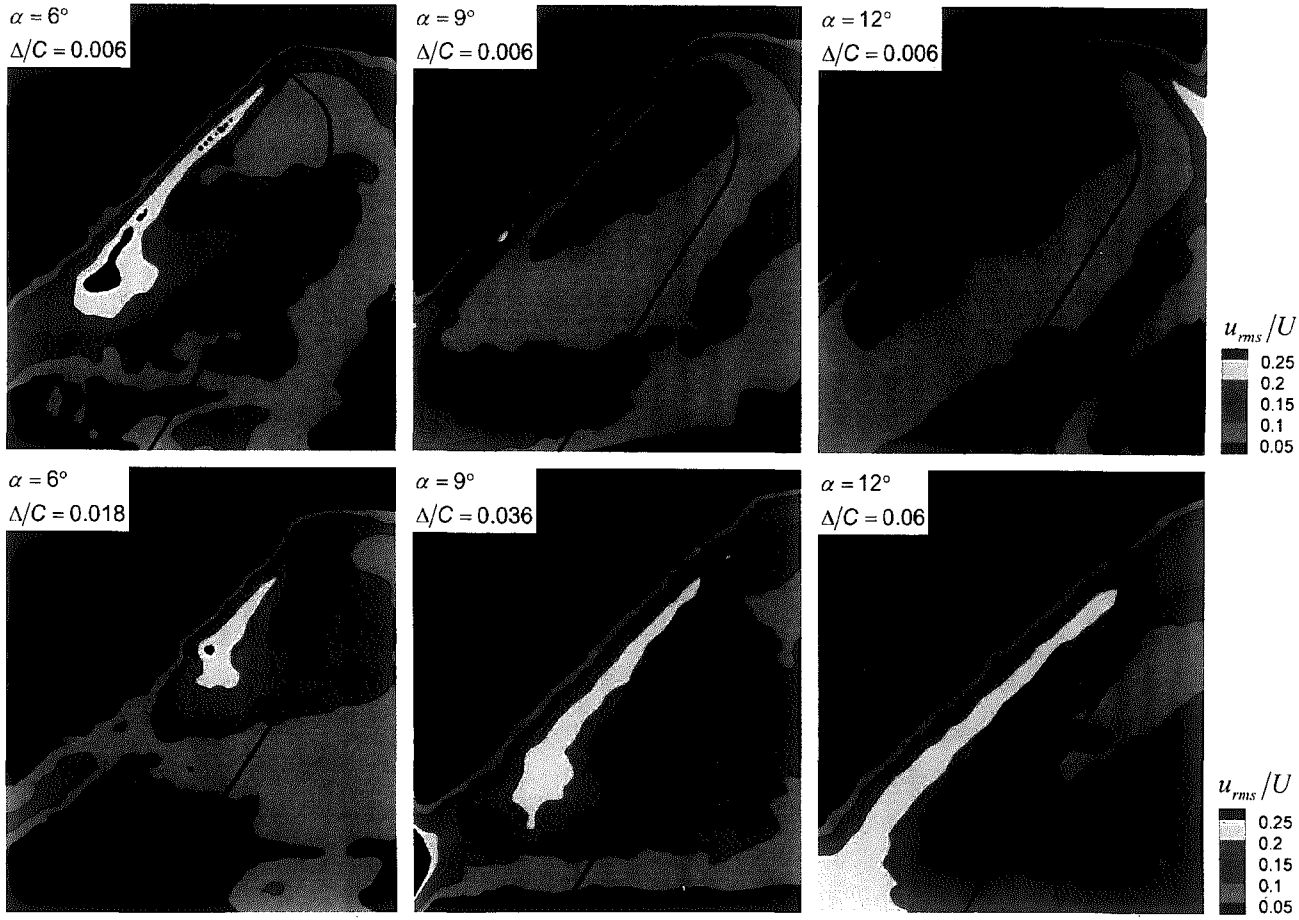

Figure 8.1: Patterns of root-mean-square of fluctuation of streamwise velocity u_{rms}/U as a function angle-of-attack α and displacement Δ/C of laser sheet from surface of wing.

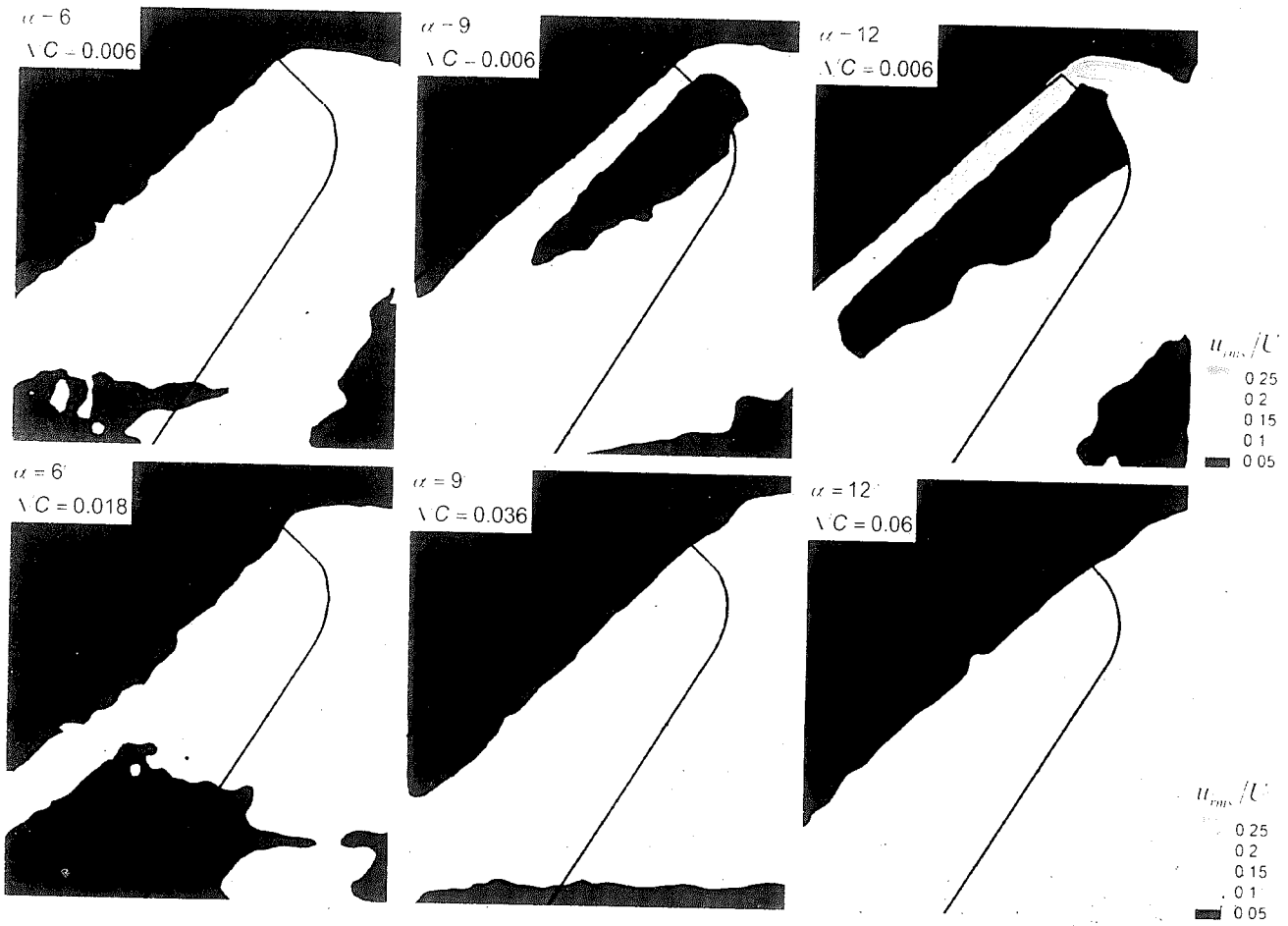

Figure 8.1: Patterns of root-mean-square of fluctuation of streamwise velocity u_{rms}/U as a function angle-of-attack α and displacement Y/C of laser sheet from surface of wing.

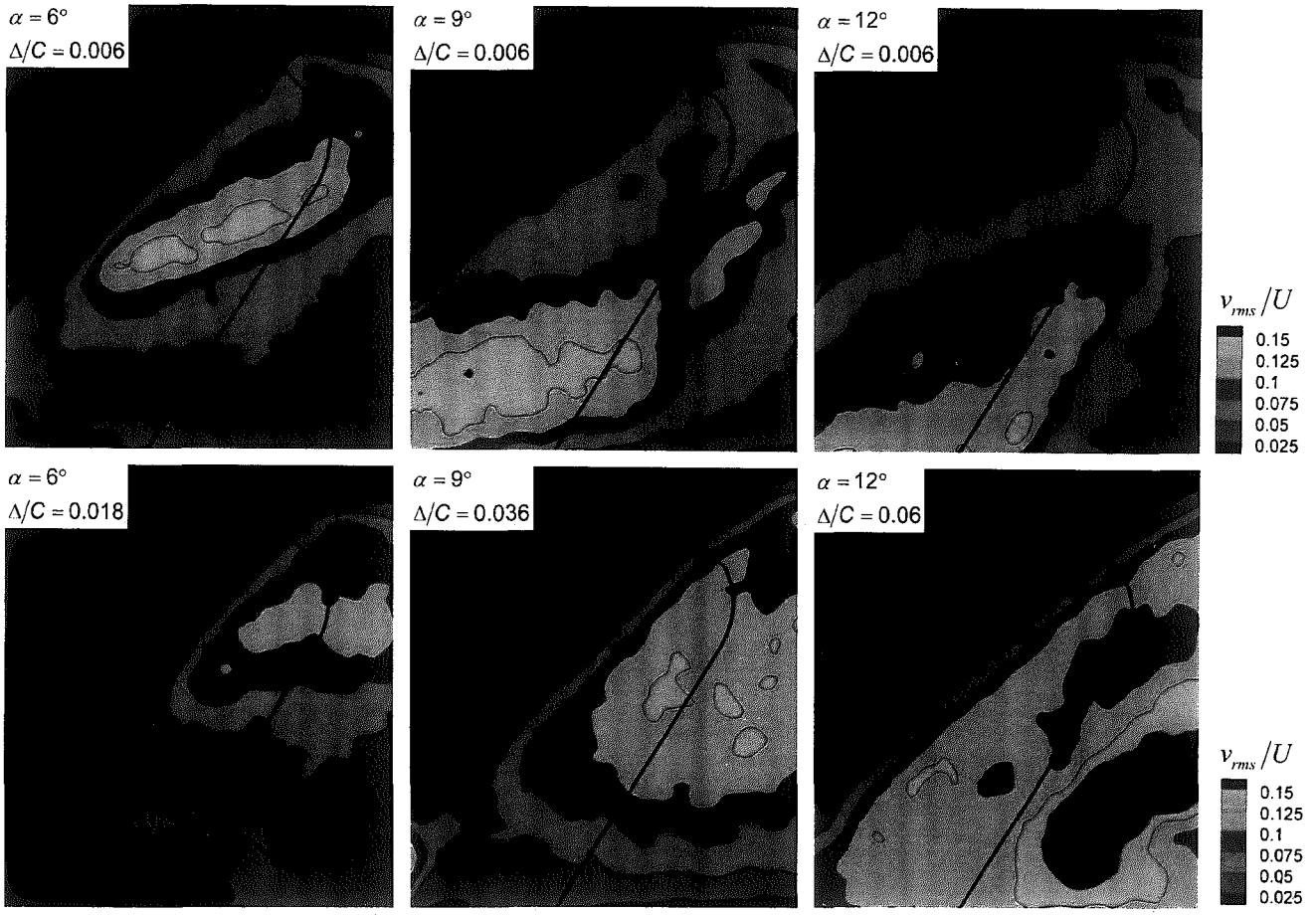

Figure 8.2: Patterns of root-mean-square of fluctuation of transverse velocity v_{rms}/U as a function angle-of-attack α and displacement Δ/C of laser sheet from surface of wing.

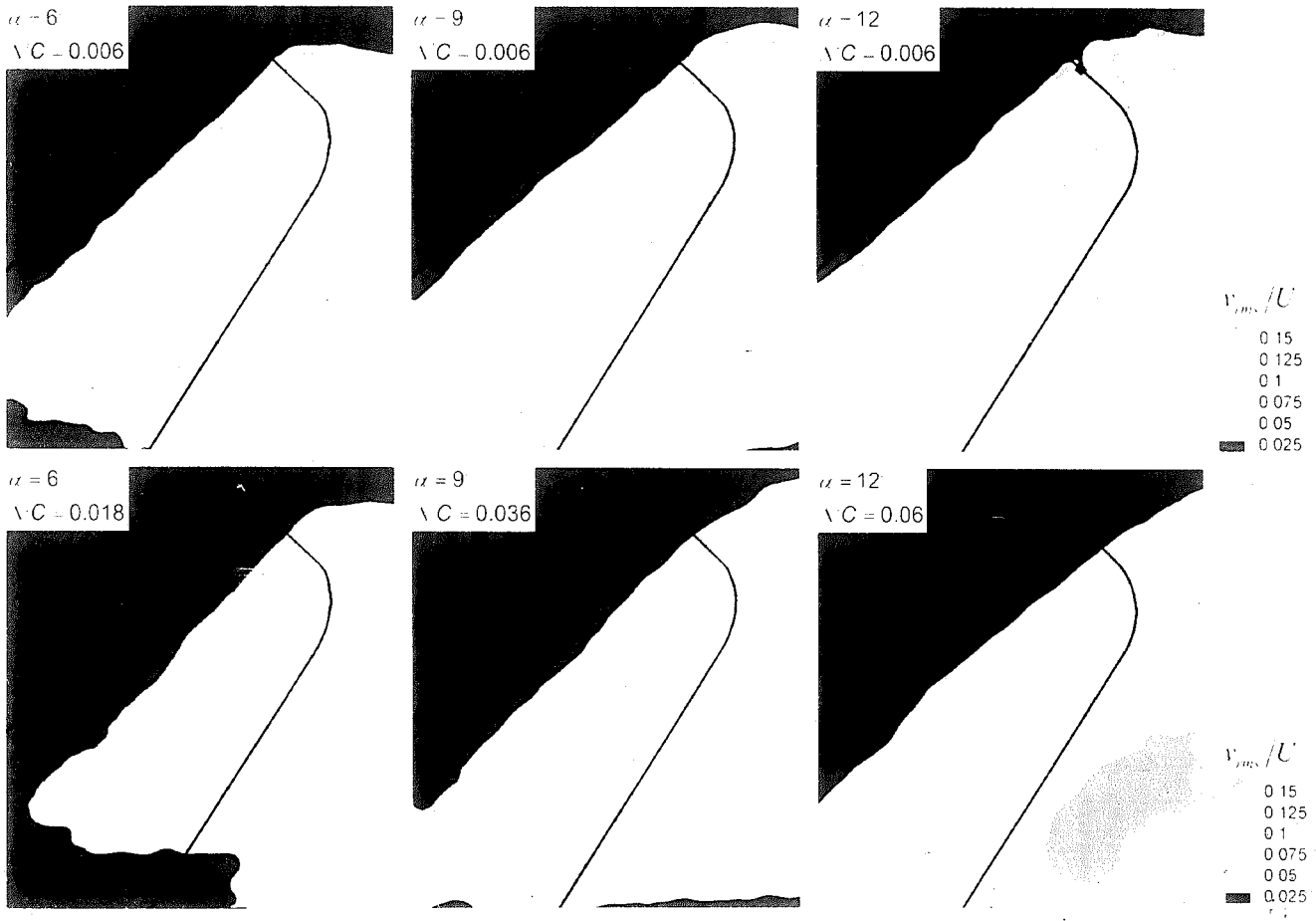

Figure 8.2: Patterns of root-mean-square of fluctuation of transverse velocity v_{rms}/U as a function angle-of-attack α and displacement Y/C of laser sheet from surface of wing.

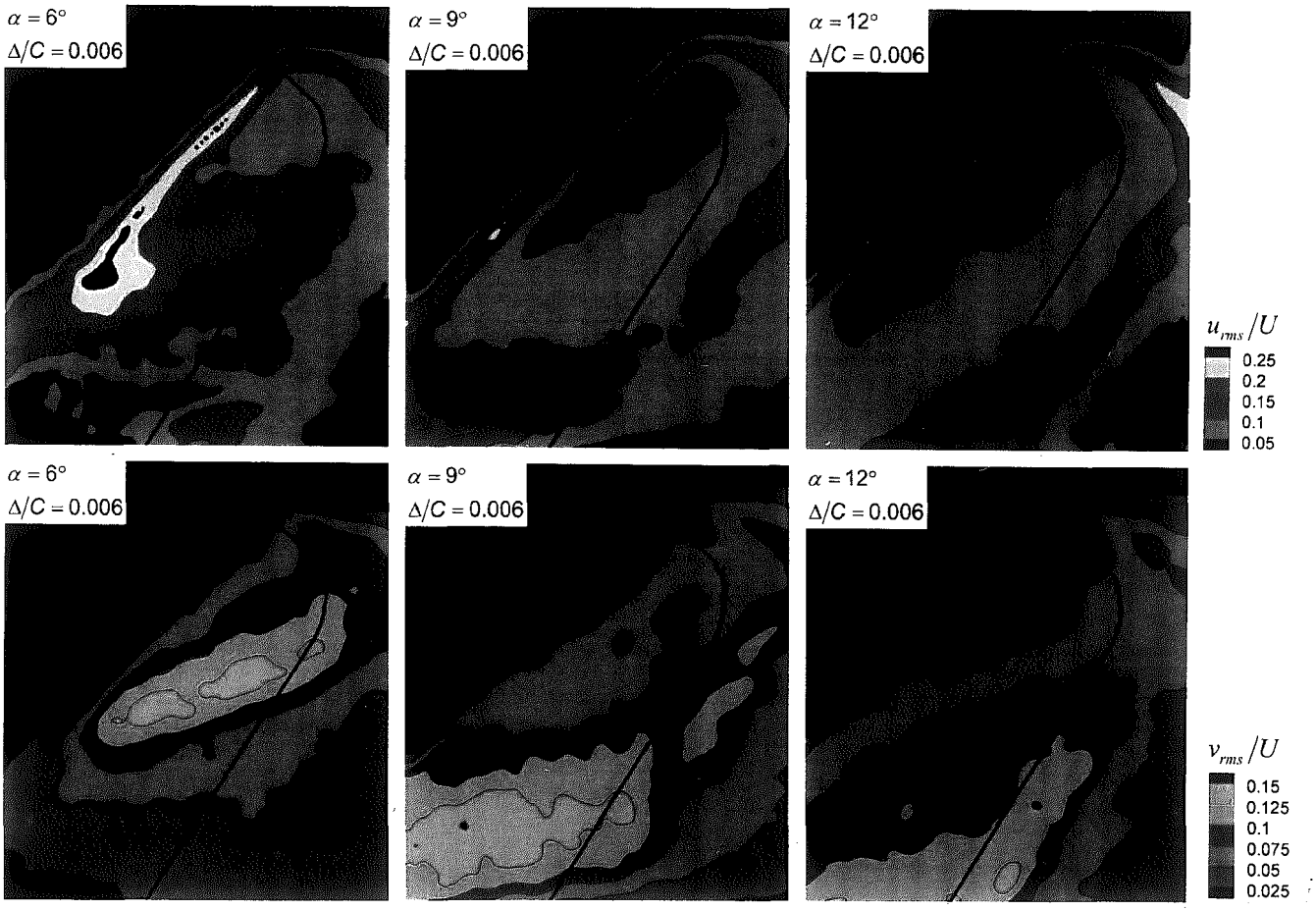

Figure 8.3: Patterns of root-mean-square of fluctuation of streamwise velocity u_{rms}/U and traverse velocity v_{rms}/U for variations of angle-of-attack α at a constant displacement Δ/C of the laser sheet from surface of the wing.

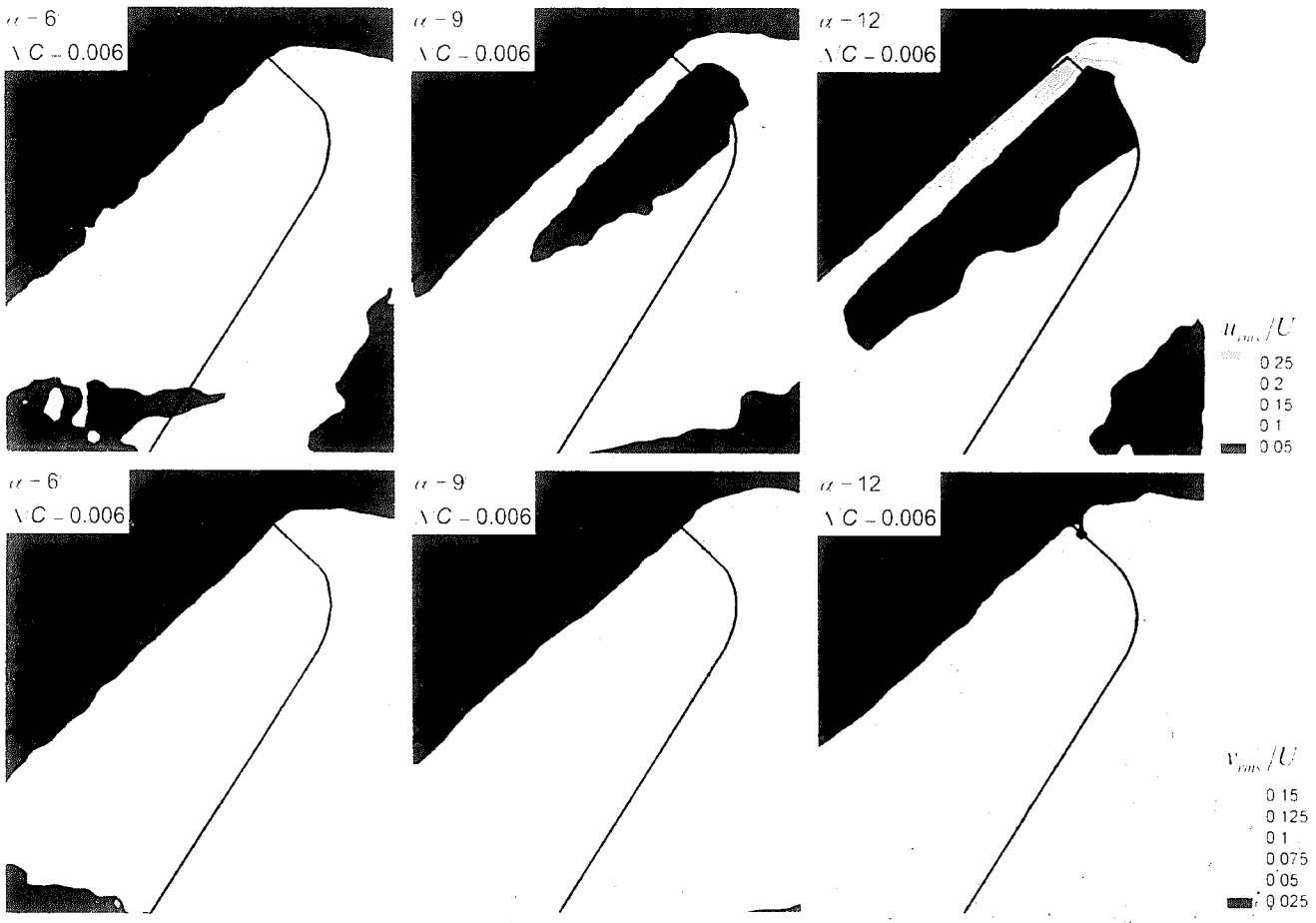

Figure 8.3: Patterns of root-mean-square of fluctuation of streamwise velocity u_{rms}/U and traverse velocity v_{rms}/U for variations of angle-of-attack α at a constant displacement Y/C of the laser sheet from surface of the wing.

LIST OF REFERENCES

Attar, P. J., Gordnier, R. E. and Visbal, M. R. 2006 "Numerical Simulation of the Buffet of a Full Span Delta Wing at High Angle of Attack", Structural Dynamics and Materials Conference, Vol. 8, Collection of Technical Papers – 47th AIAA/ASME/ASCE/AHS/ASC Structures, Structural Dynamics and Materials Conference: 14th AIAA/ASME/AHS Adaptive Structures Conference, 8th AIAA Non-Deterministic APP, pp. 5783-5805.

McParlin, S. C., Bruce, R. J., Hepworth, A.G., and Rae, A.J. "Low Speed Wind Tunnel Tests on the 1303 UCAV Concept", QinetiQ/fST/tR025502/1.0, QinetiQ, Ltd., Farnborough, UK, March 2003.

Elkhoury, M. and Rockwell, D. 2004 "Visualized Vortices on Unmanned Combat Air Vehicle Planform: Effect of Reynolds Number", *AIAA Journal of Aircraft*, Vol. 41, No. 5, September/October, pp. 1244-1247.

Gursul, I., Taylor, G., and Wooding, C. L. "Vortex Flows over Fixed-Wing Micro Air Vehicles", AIAA 2002-0698.

Jeon, D. Ph.D. Thesis, Caltech, 2000.

Miau, J. J., Kuo, K. T., Liu, W. H. Hsieh, S. J., Chou, J. H. and Lin, C. K. "Flow Developments above 50-° Sweep Delta Wings with Different Leading-Edge Profiles", Journal of Aircraft, Vol. 32, No. 4, July-August, 1995.

Nelson, R. C., Corke, T. C., He, C., Othman, H. and Matsuno, T. "Modification of the Flow Structure over a UAV Wing for Roll Control", 45th AIAA Aerospace Sciences Meeting and Exhibit, January 8-11, Reno, NV, AIAA-2007-884.

Ol, M. Water Tunnel Velocimetry Results for the 1303 UCAV Configuration, Collection of Technical Papers- 24th AIAA Applied Aerodynamics Conference, 2006, AIAA 2006-2990, 546-557.

Ol, M. V. and Gharib, M. 2003 "Leading-Edge Vortex Structure of Nonslender Delta Wings at Low Reynolds Number", *AIAA Journal*, Vol. 41, No. 1, January, 2003. pp. 16-26.

Ol, M., McAuliffe, B. R., Hanff, E. S. Scholz, U., Kaehler, Ch., "Comparison of Laminar Separation Bubble Measurements on a Low Reynolds Number Airfoil in Three Facilities", AIAA 2005-5149, 2005.

Poisson-Quinton, P. and Werle, H. "Water-Tunnel Visualization of Vortex Flow". Aeronautics and Astronautics, June 1967, pp. 64-66.

Rullan, J., Gibbs, J., Vlachos, P., Telionis, D. and Zeiger, M. "The Aerodynamics of Low-Sweep Trapezoidal Wings". AIAA-2005-0059.

Taylor, G. S. and Gursul, I. 2004 "Unsteady Vortex Flows and Buffeting of a Low Sweep Delta Angle",42nd AIAA Aerospace Sciences Meeting and Exhibit, January 5-8, 2004, Reno, NV, AIAA-2004-1066.

Taylor, G. S. and Gursul, I. 2004 "Buffeting Flows over a Low-Sweep Delta Wing", *AIAA Journal*, Vol. 42, No. 9, September, 2004, pp. 1737-1745.

Tyler, C., Baust, H., Elliott, G. and Crafton, J. "Multiple Computational Simulations Performed for Comparison with Planar Doppler Velocimetry Measurements", AIAA-2005-0440. Jan. 2005.

Willert, C. E. and Gharib, M. "Digital Particle Image Velocimetry". Experiments in Fluids, Vol. 10, 1991, pp. 181-193.

Yaniktepe, B. and Rockwell, D. 2004 "Flow Structure on a Delta Wing of Low Sweep Angle", *AIAA Journal*, Vol. 42, No. 3, March, pp. 513-523.

Yavuz, M. and Rockwell, D. 2006 "Identification and Control of Three-Dimensional Separation on Low Swept Delta Wing Angle", *AIAA Journal*, Vol. 44, No. 11, November, pp. 2805-2811.

VITA

The author was born to Ibrahim and Kamile Gulnur Kosoglu in Istanbul, Turkey on June 07, 1983. He received his Bachelor of Science degree in Mechanical Engineering from Istanbul Technical University in May 2005. During his graduate study at Lehigh University, he worked under the supervision of Professor Donald Rockwell. He is currently enrolled in the Master of Science in Mechanical Engineering program in the P. C. Rossin College of Engineering at Lehigh University and will continue towards his Ph.D. at Virginia Tech in Blacksburg, VA in Fall 2007.

END OF TITLE